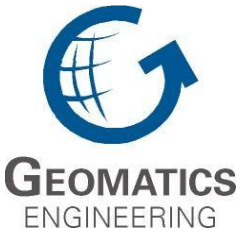

UCGE REPORTS

Number 20310

Department of Geomatics Engineering

Detection of High-Latitude Ionospheric Irregularities from GPS Radio Occultation

(URL: http://www.geomatics.ucalgary.ca/graduatetheses)

by

Man Feng

May 2010

UNIVERSITY OF CALGARY

Detection of High-Latitude Ionospheric Irregularities from GPS Radio Occultation

by

Man Feng

A THESIS

SUBMITTED TO THE FACULTY OF GRADUATE STUDIES

IN PARTIAL FULFILMENT OF THE REQUIREMENTS FOR THE

DEGREE OF MASTER OF SCIENCE

DEPARTMENT OF GEOMATICS ENGINEERING

CALGARY, ALBERTA

May, 2010

ABSTRACT

GPS radio occultation techniques (RO) are effective tools to study ionospheric layered structures. Electron density is estimated from L1 and L2 excess phase delays of the RO signal. Ionospheric structures of electron density irregularities can cause signal fluctuations on GPS L1 and L2 phase paths between the LEO and GPS satellite. The retrieved electron density profiles and their fluctuations can be studied to gain new insight into variations and vertical distributions of ionospheric structures in the high latitude ionosphere for different levels of ionospheric activity, such as storm-enhanced density (SED) and auroral substorms. In this research high latitude scintillation effects and associated electron density profiles are analyzed using COSMIC and CHAMP radio occultation observations. Mechanisms for ionospheric scintillations are investigated from analysis of fluctuations observed in the retrieved electron density profiles during the selected disturbed periods. Electron density maps are also generated to capture the latitudinal extent of the auroral oval under disturbed ionospheric conditions.

ACKNOWLEDGEMENTS

I would like to take this opportunity to thank everyone that helped and supported me to complete the research during the two and half years.

First and foremost, To Dr. Susan Skone, I would like to sincerely thank you for providing me the great opportunity to pursue my graduate study in Department of Geomatics Engineering. Thank you for your helps, patient guidance, and continuous support. You inspire my exploration of both ionosphere science and geomatics engineering. You teach me to think in an academic manner. You also lead me to the gate of research and make me really enjoy the time of working with you.

To Dr. Yang Gao, Dr Kyle O'Keefe, Dr. Geard Lachapelle and Dr. Naser El-Sheimy thank you for your various help and instruction to me through my study.

To other members of Dr. Susan Skone's group, Ossama, Fatemeh, Rajesh and Sadeque thanks for being so analytical and for letting me interrupt you as often as I did to get help from you.

To my family, my dear father and mother, thanks for caring about me and supporting me throughout my entire life. Thanks for all the encouragement and comfort from you when I met difficulties. Thanks for the endless love from my family.

TABLE OF CONTENTS

LIST OF TABLES

LIST OF FIGURES

LIST OF ABBREVATIONS

AE	Auroral Electrojet
AEI	Auroral E-ionization
A.S.	Anti-Spoofing
CDAAC	COSMIC Data Analysis and Archive Center
CHAMP	Challenging Mini-Satellite Payload
COSMIC	Constellation Observing System for Meteorology, Ionosphere and Climate
DoD	Department of Defence
ED	Electron Density
GNSS	Global Navigation Satellite System
GPS	Global Positioning System
GRACE	Gravity Recovery and Climate Experiment
GUVI	Global Ultraviolet Imager
HMF2	Height of F2 peak
NMF2	Density of F2 peak
PSD	Power Spectral Density
RO	Radio Occultation
S.A.	Selective Availability
SNR	Signal to Noise Ratio
TEC	Total Electron Content
WAAS	Wide Area Augmentation System

CHAPTER 1

INTRODUCTION

1.1 BACKGROUND

High latitude scintillation effects related to ionospheric activities are a concern for satellite-based navigation systems. Ionospheric electron density irregularities can cause short-term fading and rapid phase changes of GPS L1 and L2 signals [*Mitchell et al.,* 2005]. The formation of irregularities is usually associated with certain ionospheric activity dependent on latitude and local time. For example, during strong magnetic storm periods the dusk sector mid-latitude region (United States) can have storm enhanced densities and subauroral ionospheric drifts [*Ledvina et al.,* 2004]. At high latitudes in Canada, usually the auroral oval and polar cap regions, the ionosphere is affected by the related magnetospheric processes at night [*Basu et al.*, 2002]. Satellite-based navigation system users may expect significantly degraded positioning accuracies during the coming solar maximum (approximately 2012-2013). Ionosphere research, in the context of Global Navigation Satellite Systems (GNSS), is necessary to anticipate such effects.

Ionospheric scintillations can degrade GNSS receiver tracking performance. A number of methods exist to model, predict and understand such signal scintillations. The Wide Area Augmentation System (WAAS) and other ground-based networks with ionosphere monitoring applications have been deployed (and expanded) during the past decade. In Canada the Canadian Active Control System GPS reference network

can be used to study effects such as high latitude ionospheric auroral E-ionization (AEI) (e.g. as measured by *Coker et al.* [1995]). Recently, GPS radio occultation techniques (GPS/MET, CHAMP, COSMIC, GRACE missions etc.) have been employed to provide observations of the ionosphere from geospace; this is deemed to be a useful tool to monitor the ionospheric structures at different vertical layers [*Tsybulya, 2005; Wu, 2006*]. Like incoherent scatter radar and ionosonde observations, radio occultation retrievals are capable of providing ionospheric electron density information for various altitudes.

High-latitude irregularity structures in the ionosphere can cause strong fluctuations on GPS L1 and L2 phase paths which can be measured by GPS receivers onboard a low-Earth orbiter (LEO); from such observations electron density profiles may be retrieved. The radio occultation (RO) technique is effective for providing vertical information for three-dimensional ionosphere modeling. The LEO can provide global, all-weather, high vertical resolution measurements of atmospheric and ionospheric parameters [*Melbourne et al., 1994; Kursinski et al., 1997; Wickert et al., 2001; Hajj et al., 2002*] which are not available using other more conventional instruments and platforms. In this thesis ionospheric scintillation effects and electron density distributions at high latitudes are analyzed using CHAMP and COSMIC mission radio occultation observations. Scintillation evaluation is conducted through analysis of RO raw phase observations and retrieved electron densities from excess phase delay.

RO missions contribute to several aspects of ionospheric study including: (1) Specification and forecasting of electron density; (2) Ionospheric scintillation and irregularities; (3) Analysis of the driver source physics and response of the ionosphere. The continuous and global measurement of ionospheric electron density is essential to characterize diurnal, seasonal and annual cycles. For specific analyses it is also

helpful to capture detailed information of several space weather phenomena such as the following: production and evolution of auroral effects, generation of spread-F, AEI and intermediate layers, in addition to time variation of NmF2 (density of F2 peak) and HmF2 (altitude of F2 peak) to study dynamo electric field and thermospheric wind.

On the operational side, electron density profiles measured by RO can be used to estimate the ionospheric range error for line-of-sight GPS observations, as required by GPS users to achieve precise positioning accuracy, and other space weather applications. For ionospheric modeling, a variety of research has been conducted to model the background ionosphere as well as the scintillation effects on single and dual frequency positioning and on WAAS receivers [*Hegarty et al.,* 2001; *Conker et al.* 2003; *Skone et al.,* 2005]. Disturbed ionospheric conditions at high latitudes are more critical for modeling because of the further degraded positioning accuracies during “storm” periods. Scintillation simulation software has been developed to create realistic ionospheric scintillation conditions with appropriate phase and amplitude variations on GPS signals. However, such scintillation models usually ignore the real physical conditions in the ionosphere since the ionosphere is not a uniform, horizontally stratified medium as assumed but contains various sizes of irregularity structures at different altitudes [*Hargreaves,* 1992]. For example the higher-order terms of ionospheric effect will cause differential bending effects (and therefore signal paths) dependent on frequency. Signal paths of the GPS L1 and L2 signals (due to their different frequencies) are usually separated by a small amount - tens of meters - due to the presence of free electrons while propagating through the ionosphere [*Brunner and Gu,* 1991]. This separation can result in decorrelated effects on L1 and L2 when small irregularities with scale sizes less than 100 meters exist; this causes different levels of scintillation effects on L1 and L2 signals. Such considerations are

not generally included in simulations based on statistical scintillation models. A physics-based model is preferable with signals propagated through a simulated distribution of small-scale ionospheric irregularities.

The simplest physics-based ionosphere simulation uses a thin, shallow, phase screen to represent ionospheric irregularities. This model assumes that all irregularities are lying in an infinitely thin layer, which will cause small phase perturbations along the wavefront as a wave passes through the screen [*Hargreaves* 1992]. *Dyrud et.al* [2005] proposed such a one phase screen scintillation model. It allows multiple signal frequencies to propagate through one phase screen, which is at least more accurate than the statistical models.

A more accurate model for ionosphere simulation should include the various ionospheric physical aspects such as structures with multiple scale sizes representing irregularities in the E and F layers (and therefore over a range of altitudes) when building the scintillation model. A three-dimensional model which includes multiple phase screens at various altitudes is more appropriate. In reality the ionosphere consists of layered structures, with the electron density varying with altitude and irregularities developing with vertical scale sizes of several kilometers. These irregularities cause GPS signal phase scintillation and amplitude scintillation as measured at the GPS receivers on the ground. A realistic model should consider all these factors and simulate scintillation effects on multiple frequencies realistically - to be used ultimately in testing certain receiver tracking loop configurations and developing robust receiver technologies.

The Multiple Phase Screen (MPS) Model is an effective approach to determine the propagation properties of radio waves through the ionosphere [*Levy et al.,* 2000]. A

MPS model can compute diffraction effects from the simulated Fresnel structures and produce appropriate amplitude and phase scintillation effects on different frequencies. In order to simulate more physical based scintillation models, information about ionosphere layered structures at different altitudes is required. Radio occultation methods can be used as a tool to generate required vertical information at various altitudes with global coverage. Electron density measurements can be combined in a tomographic manner to produce three-dimensional distributions of ionospheric irregularities [*Tsybulya and Jakowski*, 2005; *Kunitsyn and Tereshchenko*, 1992]. Electron density irregularities along GPS-LEO rays are localized if the data quantity of RO observations is sufficient for tomographic localization. GPS radio occultation methods for the ionosphere will accurately measure the three-dimensional electron density and yield maps of both densities and irregularities. For the advanced COSMIC mission today more than 4000 global daily occultation events are processed to produce high-resolution vertical profiles; this information can be assimilated into a more accurate model than traditional models.

1.1.1 REVIEW OF RADIO OCCULTATION TECHNIQUES FOR IONOSPHERE OBSERVATIONS

The main idea of radio occultation was developed in 1964 [*Fjeldbo and Eshleman*, 1965]. From 1975, RO was applied to study the Earth's atmosphere by using communication satellites. GPS satellites were then considered as signal sources for proof-of-concept RO missions; GPS receivers were equipped on the low earth orbiting (LEO) satellite MicroLab-1 GPS/Meteorology (GPS/MET) mission launched on April 3, 1995 [*Kursinski et al*., 1997]. More and more RO satellites for different missions were gradually launched, including ORSTED, Stellenbosch University

Satellite (SUNSAT), Challenging Mini-Satellite Payload (CHAMP), Satellite de Aplicaciones Cientificas-C (SAC-C), Formosa Satellite-3 and Constellation Observing System for Meteorology, Ionosphere and Climate (FORMOSAT-3/COSMIC), and the recent Gravity Recovery and Climate Experiment (GRACE). For scientific purposes the RO technique is mainly applied to obtain ionospheric electron densities and neutral atmosphere components such as density, pressure, temperature, and moisture.

The methodology has been developed to use RO observations, such as excess phase delay, to retrieve ionospheric or atmospheric parameters For example the implementation of an Abel transform in electron density retrievals (and improvements of such methods) has been conducted by *Sokolovskiy* [2000], *Pavelyev et al*. [2002], *Hocke et al*. [1999] and *Steiner et al*. [1999]. Research has also been conducted to evaluate and reduce the error introduced by assumptions in the electron density retrieval method: *Garcia-Fernandez et al*. [2003] and *Syndergaard* [2002].

Focused analyses, based on CHAMP's SNR and excess phases, have been conducted to study ionospheric physical processes. For example, the global sporadic E layer has been studied using 50 Hz CHAMP data by *Wu* [2006] and *Wu et al.* [2005]. The characteristic of sporadic E layer distribution has been summarized globally. Similar analysis was done by *Hocke et al.* [2001], using data from GPS/MET, and *Wickert et al.* [2004] using S4 indices calculated from CHAMP observations. Power spectral density (PSD) analysis for RO observations was conducted by *Tsybulya and Jakowski* [2005] using 1 Hz CHAMP data. The PSD analysis is used to define scale sizes of instability structures in the ionosphere with power generated from the Fourier transform. Spatial distribution of irregularities in the polar cap and auroral oval, with structures of different scale sizes defined by PSD analysis, has been studied. The

correlation between ground-based GPS scintillation measurements and RO observations has been established by *Skone et al.* [2008; 2009].

Further work has focused on comparison between radio occultation methods and other atmospheric monitoring tools for validation purposes. *Lei et al.* [2007] compared the electron densities retrieved from COSMIC observations with ISR, Ionosondes, IRI model, and the TIMEGCM model. The COSMIC electron density was proved to be consistent with other measurements and with model simulations. Overall, radio occultation methods have been proven as a powerful tool to provide valuable information about ionospheric electron density properties.

1.2 OBJECTIVES

The significance of this research is the use of RO observations to determine characteristics of ionospheric electron density distributions at high latitudes, with a focus on investigating ionosphere structures and instabilities under high levels of ionospheric activity. The major objectives are described as follows.

1) Identify specific RO events representative of disturbed auroral conditions and establish spatial characteristics of associated ionospheric instabilities and structures.

2) Validate RO observations using other ground observations and compare results of RO retrievals with the existing theory for high latitude irregularity measurements.

3) Develop maps of electron density irregularities for the high latitude region.

4) Verify the necessity of scintillation models using multiple phase screens and provide information for specification of ionospheric tomography methods during disturbed ionospheric conditions.

1.3 OUTLINE

The first chapter is the brief introduction of this thesis. Chapter 2 will present relevant background knowledge about Global Navigation Satellite Systems (GNSS). Chapter 3 introduces properties of the high latitude ionosphere and the ionospheric effects on GNSS signals. Chapter 4 describes radio occultation techniques.

In Chapter 5 radio occultation observations are validated using other ionospheric observation tools, with a focus on ionospherically disturbed periods. In Chapter 6 representative RO events during disturbed periods are identified and ionospheric irregularities are analyzed using filtering and PSD analysis. Chapter 7 includes use of RO measurements for ionospheric electron density mapping. Observation availability for mapping using COSMIC mission data is also investigated. Auroral and magnetospheric morphology for electron density profiles is illustrated during ionospherically disturbed periods.

1.4 CONTRIBUTION OF THIS RESEARCH

Chapters 5, 6 and 7 contain analyses and results of the thesis. Until now radio occultation measurements from COSMIC or other RO missions have been used extensively to study equatorial ionospheric irregularities, or sporadic E layer for the

mid- and low- latitude ionosphere, such as presented by *Hocke et al.* [2001], *Hajj et al.* [2000], *Hocke et al.* [2001], *Wu* [2006], *Wu et al.* [2005; 2002]. However only minimal work has been done to monitor high-latitude irregularities by using radio occultation measurements since the high-latitude ionospheric irregularities are not formed (or observed) as often as equatorial irregularities. Due to the deficiency of RO observation availability it is easier to map the low- and mid-latitude ionosphere using an average of several days of observations. However, for the high latitude region the auroral irregularities do not occur regularly but are associated with storm events; during such storm events it is hard to obtain enough simultaneous radio occultation observations.

Prior to the wider observation coverage generated by COSMICII (which is expected in future to provide continuous ionosphere observations globally), in this work the high latitude auroral irregularities associated with ionospheric scintillation are analyzed from studies of single profiles; ionospheric irregularities are mapped to latitude and local time for short ionospherically “disturbed” periods. Single electron density profiles are selected for disturbed periods and augumented with ground scintillation data and geomagnetic field observations for the disturbed times and locations. Structures of ionospheric irregularities are studied by applying PSD analyses to the electron density profiles. Ionospheric irregularity maps are created by averaging the selected disturbed electron density profiles within a given latitude and local time sector (since the auroral phenomena are fixed with respect to the sun.) The latitudinal extent of aurora is captured by mapping the “disturbed” electron density profiles from radio occultation observations in this manner. These analyses are the first such studies of high-latitude ionospheric irregularities (associated with scintillation) conducted using RO observations. The TEC enhancement due to AEI is also calculated. An extra range delay due to AEI is quantified for GNSS applications.

Overall the contribution of this work is comprised of validation of radio occultation observations during disturbed periods with incoherent scatter radar observations, selection and analyses of auroral electron density profiles from radio occultation observations and the spatial mapping of high latitude ionospheric irregularities.

The main dataset used in this thesis is selected from the excess phase products from COSMIC CDAAC. The electron density retrieval method from excess phase observation is described in Chapter 4. However, this retrieval process is not unique to the work presented in this thesis. Only the analyses of electron density profiles and other data products from radio occultation missions - with respect to high-latitude ionospheric irregularity analysis - is a unique contribution of this thesis.

CHAPTER 2

INTRODUCTION TO GPS THEORY

2.1 OVERVIEW OF GLOBAL POSITIONING SYSTEM

The Global Positioning System (GPS) is a radio-based, all weather, satellite navigation system developed by the U.S. Department of Defence (DoD) and Department of Transportation (DOT). GPS's basic architecture was initiated in 1973 and the first satellite was launched in 1978, and the system reached full operating capability in 1995. The purpose of GPS is to provide precise estimates of position, velocity, and time to global users. GPS positioning is based on one-way ranging measurements with GPS satellites transmitting precise radiowave signals, allowing the receivers to determine their position. Ranges are measured to four or more satellites by one GPS receiver through code correlation methods using the received signal and the user-generated signal [*Parkinson and Spilker*, 1996].

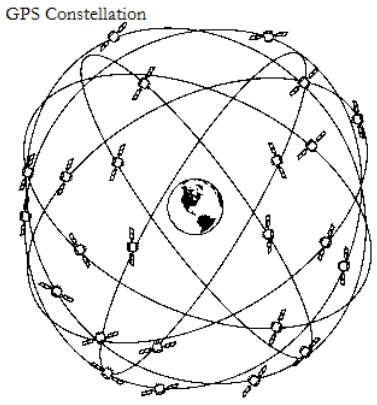

Figure 2.1 GPS satellite constellation [after *Dixon*, 1997]

Four or more observation equations can be used to solve for the receiver's position in three dimensions and its clock error. The GPS consists of three segments: space segment, ground control segment, and user segment.

2.1.1 SPACE SEGMENT

The space segment consists of up to 32 GPS satellites. The operational satellites orbit the earth in six orbital planes with an inclination of fifty-five degrees at approximately 20200 km above the Earth's surface [*Kaplan and Hegarty,* 2005]. The advantage of such high altitude is that GPS will not suffer the atmospheric drag effect, which is beneficial for precise satellite orbit determination. Each of these six orbital planes is spaced sixty degrees apart. A GPS satellite has an orbital period of 11 hours and 58 min, which means it will orbit the earth twice each day. Figure 2.1 is the constellation of GPS satellites. Each GPS satellite will continuously broadcasts signals, which are received by GPS receivers. GPS systems ensure that there will be at least four satellites above the horizon locally since the GPS receiver needs four satellites to solve its positions in three-dimensional coordinates plus the receiver clock error. All the satellites use onboard atomic clocks to produce the synchronized signals and broadcast over the same frequency (eg: L1 as 1575.42 MHz). GPS satellites transmit information at a rate of 50 bits; data includes satellite time and synchronization signal s, precise orbital data; time correction information, approximate orbital data, correction signals to calculate signal transit time; ionosphere error correction and operating status of the satellite [*Kaplan and Hegarty,* 2005].

2.1.2 CONTROL SEGMENT

The GPS control segment includes a master control station (MCS) located at Schriever AFB in Colorado Springs, five monitor stations (MS) distributed globally, which are responsible for collecting range data and monitoring the navigation signal. The MCS is the center of ground support and calculates all positions and clock errors for individual satellites based on the information from monitor stations. It also sends the required correction information back to the satellites. The monitor stations check the position, speed and condition of the orbiting satellites. Satellites' orbit and clock errors are predicted with the information collected by the monitor stations [*Kaplan and Hegarty,* 2005].

2.1.3 USER SEGMENT

GPS receivers consist of an antenna, a highly-stable oscillator and receiver-processors. Receivers compute the local position solution by measuring the ranges of at least four GPS satellites combined with knowledge of satellites' positions from the broadcast ephemeris [*Parkinson and Spilker,* 1996]. The radio signals transmitted by GPS satellites take about 67 milliseconds to reach a receiver on the ground. The receiver measures the transmission time of the signal from the satellite antenna to the receiver antenna. Correlation technique is used, where the transmission time is determined by the shifted interval that maximum correlation is obtained between satellites' PRN code and identical code generated by the receiver. The shifted time multiplied by the speed of light in a vacuum is the range from a given satellite to the receiver. However, the transmission medium is more complicated than a simple vacuum. The error introduced by the earth's atmosphere should be considered, which will be discussed

later. Due to the effect of Doppler shift the transmitted signals can be shifted by up to ±5000 Hz at the reception point. Hence the determination of the signal travel time and data recovery requires both the correlation with possible codes at all possible phase shifts and the identification of the correct phase carrier frequency [*Kaplan and Hegarty,* 2005].

.

Nowadays the receivers usually have 12 to 20 channels which is the number of GPS satellite signals that can be monitored simultaneously. If more than four satellites are tracked the position of the receiver will be solved with redundant observations by the least squares method which is an approach to solving an overdetermined system.

2.2 GPS SIGNAL DESCRIPTION

Currently every GPS satellite broadcasts on two frequencies: L1 (1.57542 GHz) and L2 (1.22760 GHz). The L1 and L2 signals received can be written as:

$$S_{L1}(t)=\sqrt{2C_{C/A}}\,D(t)X(t)\sin(2\pi f_1 t+\theta_1)+\sqrt{2C_{P1}}\,D(t)P(t)\cos(2\pi f_1 t+\theta_1) \quad (2.1)$$

$$S_{L2}(t)=\sqrt{2C_{P2}}\,D(t)P(t)\cos(2\pi f_2 t+\theta_2) \quad (2.2)$$

Before the U.S DoD's implementation of the GPS modernization plan all GPS satellites transmit three signals:

On the L1 frequency one civilian signal (C/A code) and one military signal (P(Y) code) are transmitted. On the L2 frequency a second P(Y) for military applications is transmitted. The coarse acquisition code (C/A code) and precise code (P code) are two

modulations. Here $C_{C/A}$ and C_{P1} are the square root of the received power of the in-phase and quadrature components of L1 signal, respectively. C_{P2} is the square root of received power of the L2 signal. D(t) is the amplitude of L1 and L2 modulation which contains the navigation data. X(t) is the pseudorandom sequence with ±1 at 1.023 MHz corresponding to C/A code. P(t) is also a pseudorandom sequence of ±1, which modulates the quadrature component of L1 and L2 at 10.23 MHz corresponding to P code.

GPS modernization introduces a third frequency in addition to L1 and L2 frequencies. By the end of 2009, eight new satellites of Block IIR-M have been launched into orbit. The additional signals include a new civilian signal on 1227.60 MHz (L2C) and further military signals at 1575.42 MHz and 1227.60 MHz (M signals). After that 24 satellites of GPS Block IIF are to be launched into orbit with a new civilian signal of 1176.45 MHz (L5). Moreover after 2013 the new generation is planned to have the designation GPSIII with increased M signal strength and improvement of C/A signal structure for the civilian L1 frequency. All signal modernization will be discussed in Section 2.4. However the processing of COSMIC and other RO missions is based on signals from older GPS satellites. Therefore only traditional L1 and L2 signals are the focus for the data analyses in this study.

A GPS receiver will detect the signal and distinguish the amplitude, pseudorange and phase measurements for C/A, P1 of L1 and P2 of L2. Usually C/A code is more reliable than P1 since the power of it is 3 dB stronger, which is also not encrypted. C/A code is used to acquire P code since it can be acquired more easily. However, P code is more precise since it is a higher frequency modulation. P code is encrypted and not available to unauthorized users. Hence C/A code is primarily used by the

civilian users. For radio occultation technique C/A phase and P2 phase are basic measurements. The common GPS measurements are

$$L^{ij}{}_k = -\frac{c}{f_k}\phi^{ij}{}_k = \rho^{ij} + \gamma^{ij}{}_k + C^i + C^j + \upsilon_k + \lambda N \tag{2.3}$$

$$\gamma^{ij}{}_k = \eta^{ij}{}_k + d\frac{TEC^{ij}{}_k}{f^2{}_k} \tag{2.4}$$

where $\phi^{ij}{}_k$ is the measured phase cycles from transmitter *i* to receiver *j*, c is the speed of radio wave, *k* is 1 or 2 for the L1 and L2 signals respectively, ρ^{ij} is the range measurement based on the travel time between transmitter and receiver, $\gamma^{ij}{}_k$ is the delay of neutral atmosphere and ionosphere, and *C* is the clock error. The indices *i* and *j* correspond to transmitter and receiver respectively. The term υ_k contains the thermal noise and multipath error. N is the carrier phase integer ambiguity in number of cycles. In equation (2.4) $\eta^{ij}{}_k$ is the delay due to neutral atmosphere. The second term on the right hand side of equation (2.4) is the ionospheric error; $TEC^{ij}{}_k$ is the integrated electron density along GPS-LEO (or GPS to ground receiver) line-of-sight. Higher order effects of the ionosphere which are inversely proportional to f^n (n larger than 2) and very small at GPS frequencies have not been included in equation (2.4). The ionospheric error is small in the neutral atmosphere (below 40 km); however it becomes a dominant error for high altitudes especially during solar maximum during daytime. The ionospheric error also depends on frequency. As a result of the dispersive ionosphere the L1 and L2 signals experience slightly different range errors and may propagate through slightly different parts of the atmosphere due to the differential bending effects.

2.3 GPS ERROR SOURCES

GPS error sources can be classified into three categories: satellite-based, propagation effects, and receiver-based. Satellite-based errors include the satellite clock error and satellite orbit error. The errors introduced by propagation consist of ionosphere and troposphere delays, multipath and other interference. Receiver-based errors mainly consist of antenna errors, the receiver clock error, inter-channel biases, noise, and timing/tracking errors.

Satellite orbit and clock error corrections are generated by the control segment and are predicted based on the past tracking information. The discrepancy between the prediction and the real value is the error. The accuracy of broadcast orbits is about 160 cm and 7ns for satellites clocks (in June 2009) [*IGSCB*, 2009]. Usually the post-processed data will have a higher accuracy. Currently the final product of IGS is 5 cm for orbit correction and 0.1 ns for satellite clock correction [*IGSCB*, 2009].

Troposphere error can be reduced by modeling. The neutral atmosphere has an impact on GPS signal propagation from Earth's surface up to approximately 50-70 km altitude. Due to the dominant effects at lower tropospheric altitudes this propagation error is often referred to simply as "troposphere error." Simple models of troposphere propagation delay can have accuracies of 20 cm, which is adequate for low accuracy positioning. Delay of troposphere can be divided into dry and wet components, and the latter part is hard to model. Dry component accounts for 90% of the total delay and water vapor accounts for 10%. The dry atmospheric zenith delay is around 2.3 m and varies with atmospheric pressure and temperature. However, it is predictable [*Spilker*, 1996]. The model accuracy of dry component can be better than 1%. The wet component can change 10-20% in a few hours and is much less predictable [*Spilker*,

1996]. The model accuracy is approximately 10-20%. Troposphere modeling error is therefore mainly due to the wet component. The unmodeled residual is about 3 cm in the zenith [*Mendes,* 1999]. Error correction methods include the application of a traditional model, or estimation of the zenith delay by GPS post-processing and external measurements such as those from a water vapor radiometer.

Multipath error is introduced when a signal arrives at the antenna via two or more different paths. It is a large source of error when the antenna is set up in an environment with large reflecting surfaces. Multipath can cause errors as high as 15 cm for L1 carrier phase and around 15-20 m for pseudorange observations [*Hannah,* 2001]. Multipath effects can be reduced by choosing a proper location and antenna. For example the application of an RF-absorbing ground plan or choke-ring at the antenna will reduce such effects. Kalman filtering as well as other receiver processing techniques can also mitigate the multipath errors.

Receiver noise is due to limitation of the receiver's electronics, which is hard to mitigate. A better quality receiver should have a minimum noise level. Noise can be found both in carrier phase measurements and code pseudorange measurements, and the former is much lower than the latter. The level for C/A code is around 0.3 m while for carrier phase it is only 2mm [*Parkinson and Spilker,* 1996].

Receiver clock error for a common GPS receiver exists due to a low-cost internal oscillator. The measured distance is quite sensitive to the errors of time lag measurement since these observations are multiplied by a large value of speed of light. GPS treats the receiver clock error as the fourth unknown to be solved. When enough GPS satellites are tracked (four or more) the receiver clock will be synchronized to GPS time. The receiver clock error can also be cancelled by applying differential

methods.

The ionospheric error will be described in Chapter 4.

2.4 GPS MODERNIZATION

In 1998 the United States started a GPS modernization plan. In 2000, U.S. Congress authorized the efforts. The mission is referred to as GPSIII. The first step of modernization was realized by removing the Selective Availability (SA) on May 2, 2000. And the stand-alone positioning accuracy was improved to about 20 m. The other modernization aspects include adding ground stations, adding a second civil signal (L2C) and a third civil frequency (L5), adding new military signals (M-code), and adding a fourth civil signal (L1C). Currently six satellites are the modernized Block IIR-M satellites. The next-generation modernization project with L1C is scheduled to launch in 2013.

L2C is a new civil signal broadcast on the L2 frequency and transmitted by Block IIR-M (and later designed) satellites. The first modernized GPS Block IIR satellite with L2C was launched on September 26, 2005. L2C signal can improve the positioning accuracy as a redundant signal. It is also applied to remove the ionospheric delay error since there are two civil signals on each satellite. Unlike the CA code L2C has two distinct PRN code sequences to provide ranging information: CM (civilian moderate) and CL (civilian long). Compared with the C/A signal L2C has 2.7 dB greater data recovery and 0.7 dB greater carrier-tracking. L5 is another civilian-use signal broadcast at 1176.45 MHz. It was implemented with the first GPSIIF satellite launched in 2010. L5 will have higher transmission power than L1 or

L2C. It also has a wider bandwidth with a 10 times faster code than L1 and L2. The major aim of L5 is to improve signal structures for enhanced performance. The L5 is an aeronautical navigation band, which means the frequency is chosen so that the aviation community can manage interference to L5 more effectively than to L2.

L1C is a civilian-use signal. It is broadcast on the same original L1 signal. The L1C signal will be available with GPS Block III launch. L1C implementation will provide C/A code to ensure backward compatibility and 1.5 dB increase in minimum C/A code power.

In future with the introduction and application of the additional L5 signal the influence of the ionosphere on the signal can be better compensated or even eliminated [*McDonald*, 2002]. This is because the ionosphere delay is dependent on the signal frequencies. Higher order ionospheric error can be estimated in addition to the first order range error (please refer to Section 3.3.1). In that case an improved ionospheric error calibration capability is expected for future radio occultation missions. However the dataset for current RO missions (used in this study) is based on the original GPS L1 and L2 signal configurations.

CHAPTER 3

IONOSPHERIC EFFECTS ON GPS

3.1 IONOSPHERE INTRODUCTION

The ionosphere is defined as part of the upper atmosphere extending between approximately 60 and 1500 km altitude above the Earth's surface. This region is populated by free electrons with sufficient density that can affect radio wave propagation. Free electrons and positively-charged ions are created from the ionization of molecules by solar radiation (and cosmic particles to a minor degree) [*Ratcliffe*, 1964]. In the ionization process molecules and atoms in the atmosphere receive enough radiation energy such that one or more electrons will be dissociated from the neutral molecules or atoms. Since the atmosphere at ionospheric heights is very sparse it takes time for electrons and the positive ions to recombine. The free electrons exist in approximately the form of plasma. The ionization process is highly dependent on solar radiation. Electron densities in the ionosphere vary with time (universal time, season and solar cycle), locations (altitude, latitude and longitude), and magnetic activity [*Schunk and Nagy*, 2000]. Figure 3.1 shows typical daytime and nighttime electron density profiles for solar minimum and maximum conditions.

Figure 3.1 is an example of electron density profiles at mid-latitude. Electron density can change in magnitude between day and night, solar maximum and minimum. The ionosphere structure can be very complicated. Usually ionospheric characteristics are distinguished between equatorial, mid-latitude, and high-latitude regions. The high

latitude ionosphere can also be divided into auroral oval and polar cap regions, with boundaries between regions defined by magnetic field properties [*Kunitsyn* and *Tereshchenko,* 1992]. Physical processes in the high latitude ionosphere are usually associated with effects of the solar wind, local electric fields and particle precipitation, which are linked to magnetospheric regions.

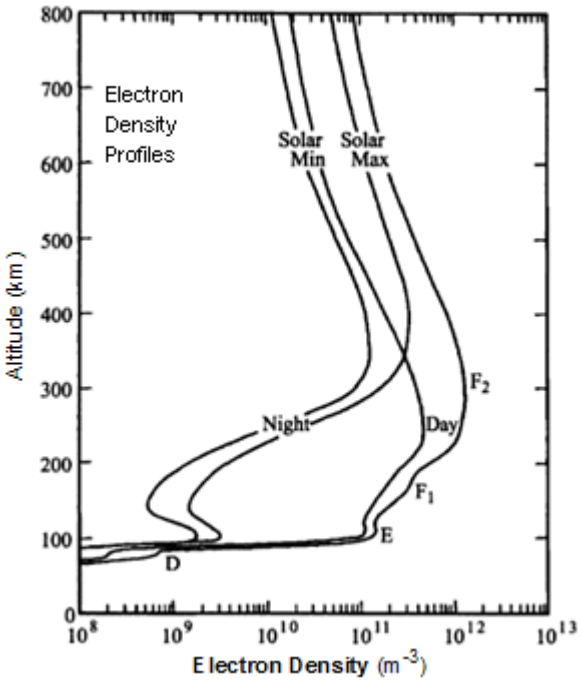

Figure 3.1 Ionospheric electron density profiles for solar minimum and maximum (daytime and nighttime) at mid-latitude [after *Schunk* and *Nagy*, 2000]

3.1.1 REGIONS OF THE IONOSPHERE

In Figure 3.1 different regions of the ionosphere can be identified based on altitude and by characteristics of electron density. Usually the ionosphere is divided into D, E and F regions. The F region can also be divided into F1 and F2 sub-regions. These

layers are not clearly distinct and can also disappear under some conditions. They are most distinct in daytime ionosphere at mid-latitude [*Schunk* and *Nagy*, 2000].

D region is the lower part of the ionosphere from altitudes of 70 to 90 km. This layer disappears during night-time [*Hargreaves*, 1992]. The D region is complicated since it includes several sources of ionization, such as Lyman-α radiation, EUV radiation, X-ray radiation, galactic cosmic and energetic particles [*Hargreaves*, 1992]. During daytime the D region can reflect radio waves with reductions to the radio wave signal strength. The D region is a major contributor to radio absorption. This absorption in winter is increased by a factor of two or three versus summer; this is called the winter anomaly of ionospheric radio absorption.

E region is just above the D region and extends to approximately 160 km. The ionization at this altitude remains at night. This region is mainly formed by soft X-rays and far ultraviolet solar radiation [*Kelley*, 1989]. Normally this layer can only reflect radio waves with frequencies lower than 10 MHz and contribute little absorption for higher frequencies. However a significant phenomenon in the lower E region, called sporadic E (Es), can reflect 50 MHz and higher frequencies. It is characterized by transient, localized patches of related high electron density in E region, which will significantly affect radio wave propagation. Sporadic-E can last from minutes to hours causing phase and amplitude scintillation of GPS signals. Sporadic E has strong local time and seasonal variation, and is believed to have strong relations to other atmospheric or ionospheric processes [*Wu et al.*, 2005].

Another feature at high latitudes is the auroral E ionization (AEI) which can be very significant due to the precipitation of energetic electrons and protons during auroral substorm events. The vertical scale size of ionospheric irregularities can be very small

(from 0.5 to 5 km in width) [*Hargreaves*, 1992] in the region 90 to 110 km altitude. Figure 3.2 shows a typical electron density profile with AEI obtained from COSMIC observations during local nighttime auroral activity September 1, 2007. A sharp electron density peak appears around 110 km. E region can be used to reflect the signal from ground transmitters for long distance transmission. At night the E region ionization levels drop because the lack of solar radiation.

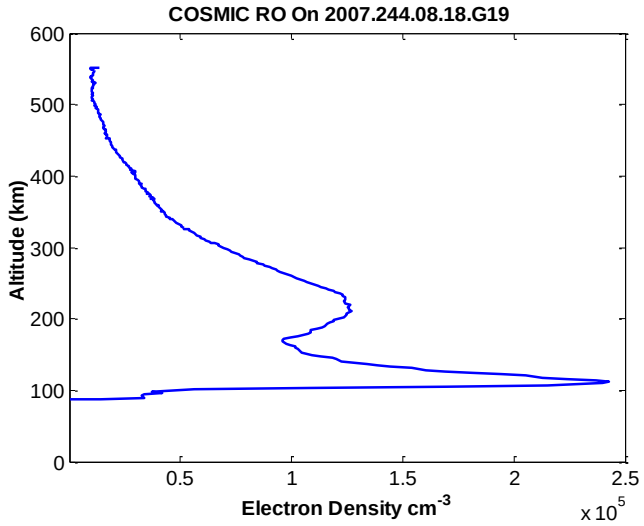

Figure 3.2 AEI observation by COSMIC FM1 08:18 UT September 1 2007

F region is the upper ionosphere at altitudes in the range 150 km to 500 km [*Kelley*, 1989]. It is mainly formed by solar radiation with 20 to 90 nm wavelengths. The F layer can be divided into F1 and sub F2 layers. The F2 layer is of great research interest for radio propagation since it has the largest electron densities [*Hargreaves*, 1992]. The F2 region is also very variable and difficult to predict. With the large F region ionospheric electron density, single layer ionospheric models usually select 400 or 350 km as the ionosphere altitude for total electron content (TEC) observation mapping. Spread F is another type of ionospheric irregularity, named for the diffused F layer echo on ionograms from digisonde observations. Equatorial spread F is a very common phenomenon after sunset [*Chen et al.*, 2006].

3.2 HIGH LATITUDE IONOSPHERE

3.2.1 MAGNETIC FIELD

The Earth's magnetic field is close to a magnetic dipole. The earth's magnetosphere (which deviates from a symmetric dipole configuration) is produced by the electrical charges' (plasma) motion in near-Earth regions [*Giraud and Petit*, 1978]. The magnetosphere acts to couple energy from the solar wind to the earth's atmosphere [*Lyou*, 2000]. Figure 3.3 shows behavior of the earth's magnetic field under the effect of solar wind [*UCLA*, 2009]. The solar wind carries the interplanetary magnetic field (IMF) from the Sun outwards and has a strong influence on the earth's atmosphere. With the protection of the earth's magnetosphere solar wind plasma cannot penetrate the earth's atmosphere directly. In Figure 3.3 the solar wind is deflected by the bow shock of the earth on the dayside.

The dipolar terrestrial magnetic field is compressed by the high speed solar wind on the dayside and stretched on the opposite nightside. The high energy particles are accelerated by transferring the energy of solar wind into heating [*Lyou*, 2000]. The Earth's magnetic field is subject to irregular short-term fluctuation plus the ordinary quasi-diurnal change due to large-scale electric current systems. The global Kp index is used to measure the magnitude of magnetic perturbations at high latitudes [*Giraud and Petit*, 1978]. The Kp index can characterize planetary magnetic (and ionospheric) activities. Details of the Kp information can be found in *Giraud and Petit* [1978].

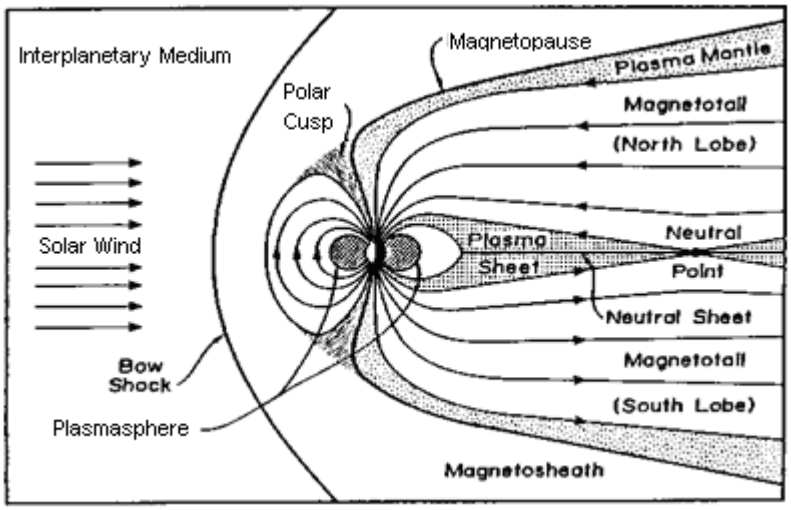

Figure 3.3 Earth's magnetic field distorted under effects of solar wind [after *UCLA*, 2009]

3.2.2 HIGH LATITUDE IONOSPHERIC IRREGULARITIES

Figure 3.4 shows the distribution of several types of ionospheric irregularities in the high-latitude ionosphere. The plasmasphere is a region where the ions and electrons are trapped by the earth's magnetic field. Usually it extends up to 60 deg N geomagnetic latitude in the night hemisphere. The poleward boundary is called the plasmapause [*Aarons*, 1982]. A trough (localized low electron density region) exists at geomagnetic latitude between 60 deg N to 65 deg N nightside. The plasmapause and trough are located equatorward of the auroral oval and polar cap.

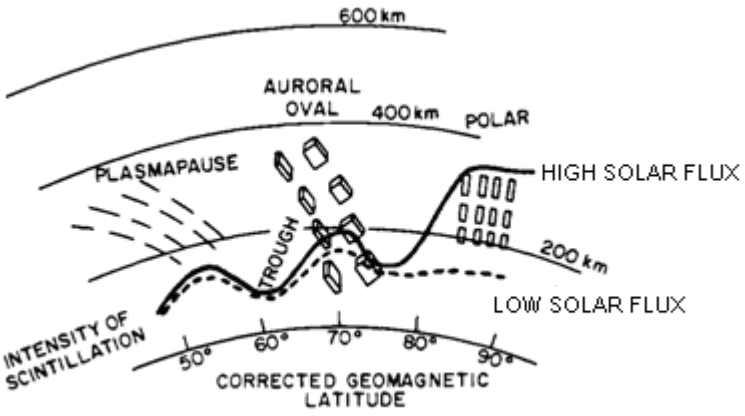

Figure 3.4 High latitude irregularities at auroral midnight [after *Aarons,* 1982]

3.2.2.1 AURORAL OVAL

The auroral oval is a region of closed magnetic field lines, which is characterized by high conductivity, auroral electroject currents and precipitating electrons. Under active conditions, energy from the solar wind is released into the auroral ionosphere and precipitating electrons collide with neutral atmospheric constituents at approximately 110 km altitude, resulting in visible aurora and variable total electron content (TEC). The magnetosphere shields the Earth's magnetic field from the solar wind and highly energetic particles do not enter the ionosphere directly. The particles will precipitate into the auroral oval along the magnetic field lines. The precipitation occurs via field-aligned currents (Figure 3.5) and into the ionospheric electroject region which is colocated with the auroral oval. Large-scale generation of field-aligned currents is introduced by the precipitation plasma flows [*Bates et al.*, 1973]. Electrons with energies of 1 to 10 keV enter the atmosphere along the closed magnetic field lines (mapping into the near-Earth magnetotail.)

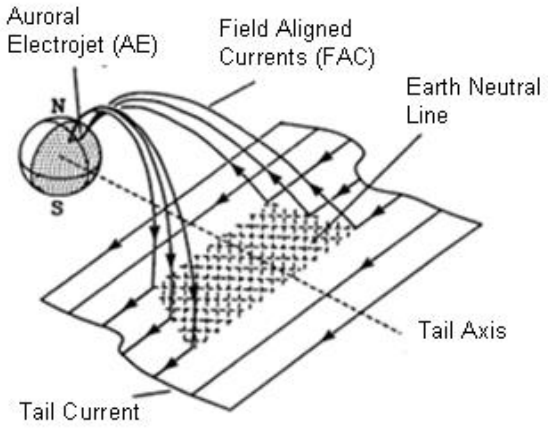

Figure 3.5 Auroral substorm current wedge; the current closes westward through the ionosphere at around 110 km [after *Skone, et al.*, 2009]

Visible and ultraviolet radiation is emitted through collision of energetic electrons and neutral atmospheric constituents, which is part of the phenomenon known as an auroral substorm. Substorms are characterized by a wedge of electric current by electrons coming from the near-Earth magnetotail (Figure 3.5) [*Skone et al.*, 2009]. The localized ionospheric closure current can be observed by ground-based magnetometers with perturbations in the H (north-south) component.

The enhancement of electron density at altitudes near 110 km, in the range 65-75° N geomagnetic latitude after local midnight, is associated with auroral substorm activity. Auroral precipitation creates irregularities in the E region - Auroral E-ionization [*Skone*, 1998]. Small-scale instabilities corresponding to localized current structures in the auroral ionosphere exist during geomagnetically disturbed periods [*Hunsucker et al.*, 1995]. Ionospheric electron density structures and irregularities exist with horizontal scale sizes in the range 20 to 400 km [*Baron*, 1974]. Decorrelation of TEC and GPS ionospheric range delays can occur over short distances (tens of kilometers). AEI can have magnitudes comparable to the F region maximum with electron densities in the range 2 - 20 $\times 10^{11}$el/m^3 [*Baron*, 1974].

3.2.2.2 POLAR CAP

The polar cap is at geomagnetic latitudes poleward of the auroral oval; this region contains magnetic field lines open directly to the solar wind [*Hunsucker and Hargreaves,* 2003]. The plasma can enter the ionosphere and becomes the source of patches forming F region irregularities in the polar cap region [*Rodger and Graham,* 1996]. Polar cap irregularities do not exhibit as strong local time dependence as those in the auroral oval [*Aarons,* 1982].

3.2.3 IONOSPHERIC PHENOMENA

Ionospheric phenomena and solar activities are highly related. The Sun emits electromagnetic radiation over a wide spectral range which becomes the major energy source of ionization of the ionosphere [*Hargreaves,* 1992]. Ionospheric phenomena are caused by interaction of the solar wind and magnetosphere. Phenomena include ionospheric storms, magnetic storms, auroral substorms, and traveling ionospheric disturbances. Some relevant processes are described here.

Auroral Substorm is usually associated with auroral disturbances. It includes three phases: growth phase, expansive and recovery phase. In the initial growth phase, auroral oval boundaries expand equatorward. Ionospheric conductivity increases and causes enhanced auroral electrojets and field-aligned currents. The growth phase is characterized by a period of southward interplanetary magnetic field (IMF) and lasts for several hours. Aurora occurs during the expansive phase when energetic particles are accelerated from near-earth nightside regions down into the atmosphere. In this phase intense aurora can be observed as the energetic particles precipitate (collide

with neutral atmospheric constituents and emit light). Large variations of electron density will occur in both spatial and temporal domains during the expansive phase and auroral E-ionization (AEI) can be observed in the E layer. Multiple expansions can occur over several hours. During the recovery phase the ionosphere will return to quiet conditions [*Davies*, 1990; *Skone*, 1998; *Skone*, 2007]. It should be noted that in this thesis "storm" usually refers to magnetospheric/auroral substorm for simplicity. The Kp and DST space weather indices can be used to measure the intensity of a local midnight substorm.

Magnetic storm is a global event characterized by disturbances of the Earth's magnetic field. It includes three phases: initial phase, main phase and recovery phase. These phases are identified in observations from low latitude magnetometers - reflecting changes in the large-scale near-earth ring current [*Skone*, 2007].

Ionosphere storm is characterized by features of F region irregularities in electron density [*Skone*, 1998]. Relations have been observed between ionospheric storms and auroral substorms. But the two phenomena are not necessarily related. The ionosphere storm can last for several days with severe effects on radiofrequency signals [*Davies*, 1990]. This event usually happens at mid-latitudes with associated variations (negative and positive phases) in total electron content.

Another phenomenon arising from magnetic storms, with strong mid- and high-latitude ionosphere electron density irregularities, is called storm enhanced density (SED). This effect usually occurs during severe magnetic storm periods with the feature of large TEC gradients at mid-latitudes. It is characterized by a plume of total electron content extending mid- to high-latitude [*Skone et al.*, 2005]. An example of storm enhanced density on March 31, 2001 is shown in Figure 3.6. The plume with

large TEC values extends through high latitudes of Canada. For SED events, the large TEC gradients can cause severe degradation of DGPS positioning accuracies. The narrow enhanced TEC plume (for example the region between 40° N and 60° N latitude) is also difficult to capture by sparse reference networks - such as for the Wide Area Augmentation System (WAAS) [*Skone*, 2007].

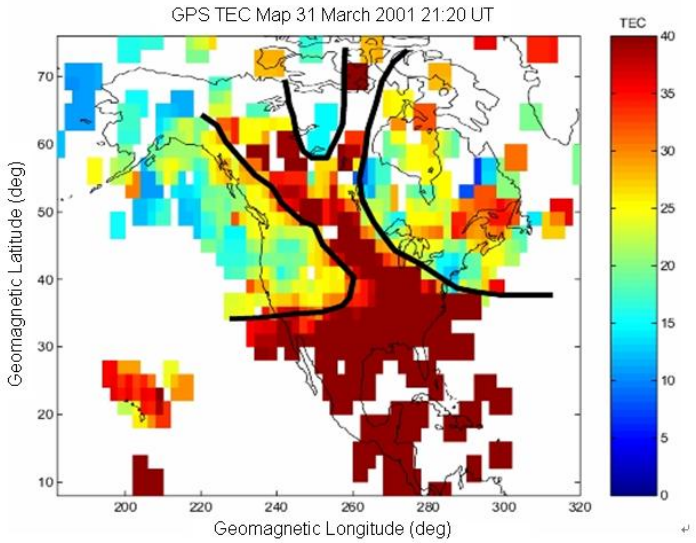

Figure 3.6 Storm enhanced density on March 31, 2001 [after *Skone et al.*, 2005]

3.3 IONOSPHERIC IMPACT ON GPS/GNSS SIGNALS

The ionosphere is an important error source for global navigation satellite systems. The ionosphere has more variability in error than the troposphere, which makes it difficult to model. For the ionosphere, the range error frequently changes at least one order of magnitude diurnally, in addition to variable activity that can greatly affect the ionospheric total electron content. The major ionospheric effects on GNSS signals are group delay, carrier phase advance, Doppler shift, Faraday rotation, refraction or bending of the signal, distortion of pulse waveforms, and scintillation effects [*Parkinson and Spilker*, 1996].

3.3.1 FIRST ORDER EFFECT

Radio-waves propagating through the ionosphere will experience effects dependent on the ionospheric electron content. The ionosphere is a dispersive medium which has slightly different effects on GPS L1 and L2 signals. A GPS receiver can measure two types of observables: code and carrier phase. The pseudorange and carrier phase measurements are formed under the assumption that GPS signals travel at the speed of light in a vacuum. However this assumption is not accurate in the ionosphere. It is the same as incorrectly considering the phase and group indices of refraction n_p and n_g of the propagation medium to be equal to 1.

The phase range and pseudorange can be calculated as:

$$\Phi = \int_{\text{path}} \lambda \, dN = \int_{\text{path}} \frac{\lambda_0}{n_p} dN = \int_{\text{path}} \frac{\lambda_0}{n_p} d\left(\frac{ct}{\lambda_0}\right) = \int_{\text{path}} \frac{c}{n_p} dt \tag{3.1}$$

$$PR = \int_{\text{path}} v_g \, dt = \int_{\text{path}} \frac{c}{n_g} dt \tag{3.2}$$

where v_g is the group velocity, c is the speed of light in vacuum, λ and λ_0 are true wavelength and vacuum wavelength respectively. The term dN is the cycles of carrier phase and dt is the travel time. Symbols Φ and PR are carrier phase range and pseudorange measurements in units of length.

In reality, the assumption of $n_g = n_p = 1$ is not correct for ionospheric (or tropospheric) signal propagation. For the ionosphere, n_p and n_g can be expressed as

$$n_p = 1 - \frac{1}{2}\frac{\omega_p{}^2}{\omega^2} = 1 - \frac{1}{2}\frac{(2\pi)^2\left(\frac{Ne^2}{m\varepsilon_0}\right)}{(2\pi)^2 f^2} = 1 - 40.3\frac{N}{f^2} \tag{3.3}$$

where N is the ionospheric electron density, e is the electron charge, m is the electron mass, ε_0 is the permittivity of free space, and f is the signal frequency. Equation (3.3) shows that the phase index of refraction n_p only depends on electron density in the ionosphere N. For group index of refraction n_g a similar expression is

$$n_g = n_p + f\frac{dn_p}{df} = 1 - 40.3\frac{N}{f^2} + 80.6 f\frac{N}{f^3} = 1 + 40.3\frac{N}{f^2} \tag{3.4}$$

The term $40.3\frac{N}{f^2}$ is the difference from a vacuum medium. This leads to the group delay and phase advance effects on GPS signals. The phase velocity is larger than the speed of light in a vacuum by the amount $\Delta v_p = \frac{c}{2}\frac{\omega_p{}^2}{\omega^2}$ (with the assumption of ω being much larger than ω_p for GPS applications, where ω is the signal frequency and ω_p is the ionospheric plasma frequency). The group velocity is less than the speed of light in a vacuum by the amount $\Delta v_g = -\frac{c}{2}\frac{\omega_p{}^2}{\omega^2}$. In equations (3.3) and (3.4) the higher order terms of ionospheric effects have been neglected due to a simplified representation of the refractive index. Only zeroth and first-order terms are considered. For the real ionosphere, magnetic field bending effects and the higher order ionospheric delay terms can all affect signal propagation - contributing as much as 1 percent of the ionospheric range error [*Brunner and Gu*, 1991; *Skone and Cannon*, 1999]. Despite this, equations (3.3) and (3.4) can still be used to derive ionospheric corrections for elimination of the first-order ionospheric effects using dual frequency

GPS receivers.

3.3.1.1 TEC MEASUREMENT

From another perspective, the existence of ionospheric delays for GPS signals can be exploited to measure the electron content along a satellite-receiver line-of-sight. The term $40.3\frac{N}{f^2}$ contributes to the ionospheric range error. After integrating, the range delay can be derived as

$$\frac{40.3}{f^2}\int_{path} Nds = \frac{40.3}{f^2}TEC \tag{3.5}$$

The TEC is the total electron content along 1 m^2 column along satellite-receiver line-of-sight. Sometimes for modeling simplicity the ionosphere is assumed to consist of a single very thin layer at 350 km, or 400 km, altitude.

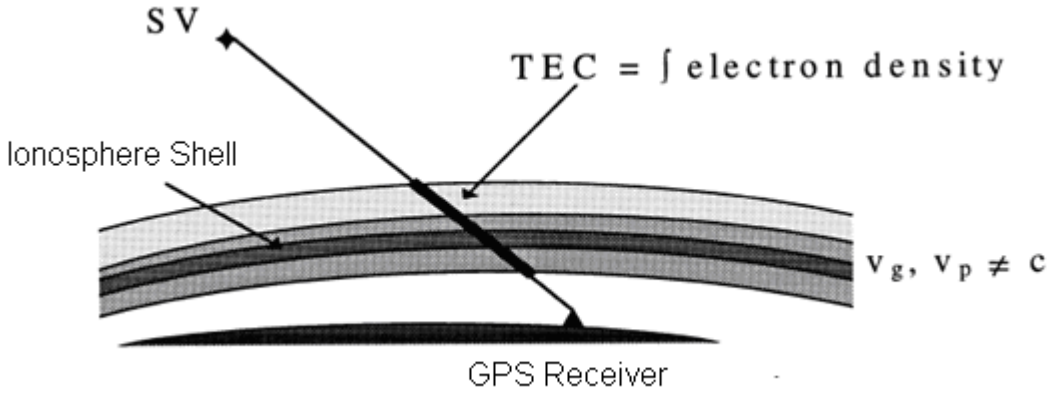

Figure 3.7 Slant TEC is illustrated along a single satellite-receiver line-of-sight [after *Skone and Cannon*, 1999]

Since GPS has multiple frequencies and the ionosphere is a dispersive medium, the TEC can be calculated by differencing range measurements on L1 and L2.

$$TEC = \frac{1}{40.3}\left(\frac{1}{\frac{1}{f_1^2}-\frac{1}{f_2^2}}\right)\left(PR_1 - PR_2\right) \qquad (3.6)$$

For ionosphere modeling usually the slant TEC in Figure 3.7 and equation 3.6 should be mapped to vertical TEC through multiplication by a mapping factor [details in *Schaer,* 1999]. There are two kinds of TEC measurements based on code or phase observations. Code-derived TEC is an absolute quantity derived with less precision than for phase measurements. Phase-derived TEC is a relative quantity (containing some biases). However, it has negligible noise and high precision. Dual frequency GPS receivers use the relative TEC to smooth the rough but absolute pseudorange-derived TEC to estimate first-order ionospheric range error corrections. This process is done automatically and is transparent to the user [*Skone*, 1998; *Schaer,* 1999].

3.3.2 SCINTILLATION EFFECTS

One primary focus of this research is ionospheric scintillations. Such effects have an impact on GNSS and satellite communications.

3.3.2.1 SCINTILLATION THEORY

Ionosphere scintillation is the rapid variation of signal amplitude or phase as the signal passes through ionospheric electron density irregularities [*Knight*, 2000].

Scintillation appears principally in the trans-ionospheric signals, which is caused by the relative phase shifts in the propagating wavefront and by subsequent diffraction [*Hunsucker and Hargreaves*, 2003]. This is illustrated in Figure 3.8.

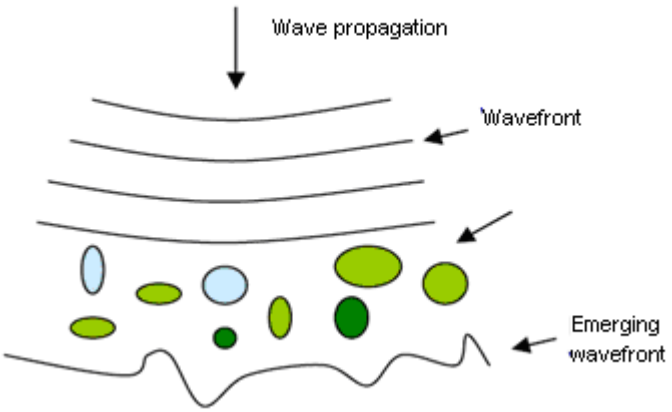

Figure 3.8 GPS signal propagating through the ionospheric electron density irregularities [*Skone et al*, 2008].

From Huygen's law, the wavefront is considered as a source of the secondary wavelets to build up the wavefront at further points. In diffraction theory this law is applied to determine how the amplitude and phase of a signal will change when propagating through the irregularities. The requirement for amplitude scintillation is that within the Fresnel zone distance there are several existing "small" irregularities [*Hunsucker and Hargreaves*, 2003].

3.3.2.2 GLOBAL MORPHOLOGY OF IONOSPHERIC SCINTILLATIONS

Figure 3.9 shows the global distribution of ionospheric scintillations. Occurrence of scintillation varies widely with the signal frequency, magnetic activities or solar activities, local time, season, and latitude and longitude [*Aarons*, 1982]. There is an obvious nighttime maximum globally. For the nighttime high-latitude region auroral

scintillation is present; spread-F (and associated irregularities leading to scintillation) occurs in the equatorial region after sunset due to the Rayleigh-Taylor instability. Scintillation is much stronger and more frequent during solar maximum versus solar minimum periods.

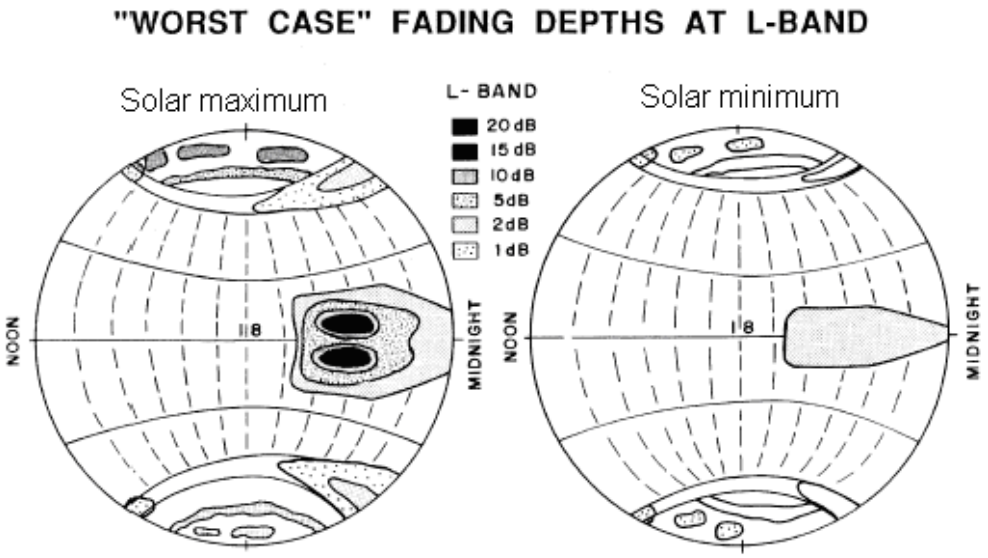

Figure 3.9 Global morphology of scintillation for L-band: solar maximum (left) and solar minimum (right) [after *Basu*, 2002].

For equatorial and high latitude regions, scintillation has different physical sources. Generally both amplitude and phase scintillation are strong at the equatorial region; only phase scintillation is common in the high-latitude auroral ionosphere. Auroral scintillation is due to irregularities arising from precipitation of energetic electrons along terrestrial magnetic field lines during substorm events. The occurrence and intensity of auroral scintillation increase with ionospheric activity [*Hunsucker and Hargreaves*, 2003].

3.3.2.3 SCINTILLATION MEASUREMENTS

There are several indices available to describe ionospheric scintillations. The S4 index is derived from GPS signals as the standard deviation of the signal power normalized to the average signal power. This quantity is used to measure the magnitude of amplitude scintillation.

$$S_4 = \left(\overline{p^2}\right)^{1/2} / \bar{P} \tag{3.7}$$

where $p = P - \overline{P}$, P is the power, and $\overline{P}$ is the mean power. Power is computed as $P = A^2$ and A is the amplitude.

Table 3.1 Phase and Amplitude Scintillation Classification [*Yu*, 2007]

Case	S_4	σ_ϕ (rad)
Strong	0.9	0.6
Moderate	0.6	0.3
Weak	0.4	0.2
Very weak	0.1	0.05

The term σ_ϕ denotes a phase scintillation index. This can be derived from GPS observations as phase variance [*Dubey*, 2006] for a given signal over intervals such as 1 s, 30 s or 60 s. The index σ_ϕ is derived from the standard deviation and the power spectrum of the detrended carrier phase observations. Table 3.1 shows the classification of scintillation indices for different levels of phase and amplitude scintillations.

GPS receivers experience degraded performance under scintillation conditions [*Leick*, 1995]. Amplitude fades may cause the signal to noise ratio (SNR) to drop below the receiver tracking threshold, resulting in a loss of code or phase lock. Strong phase scintillation may cause high phase dynamics (large frequency Doppler shifts) in GPS carrier signals; if such dynamics exceed the receiver's PLL (phase lock loop) bandwidth a loss of phase lock will occur. For semicodeless or codeless tracking technologies the signal will have an average loss of 14 to 17 dB and 27 to 30 dB [*Leick*, 1995]. In such cases the L2P(Y) PLL employs a narrow bandwidth of 1 Hz (compared with 15 Hz for L1) in order to eliminate excess noise. The result is that L2P(Y) is more susceptible to phase scintillation effects. Scintillation effects have been observed in many GPS observations. Some examples are shown in the next section.

3.3.2.4 PHASE CYCLE SLIPS

GPS phase cycle slips are loss of signal lock in the GPS receiver tracking loop. A cycle slip is observed as a discontinuity in the phase integer ambiguity. Cycle slips can occur under ionospheric scintillation conditions when high phase dynamics (exceeding receiver tracking loop bandwidths) arise from ionospheric irregularities. Figure 3.10 shows scintillation observations at Natal, Brazil for a solar maximum period [*Aarons*, 1993] and Figure 3.11 shows cycle slip occurrence at IGS BRAZ station in 2001. The cycle slip is calculated from TECMODEL software [*Skone*, 2006]. Good correlation can be found between the two plots, which illustrate the strong effects of ionospheric scintillation on GPS receivers. For the equatorial region, seasonal variations in scintillation are also found to be a function of longitude [*Beaujardiere et al.*, 2004].

Figure 3.10 Intensity of scintillation data at Brazil [after *Aarons*, 1993]

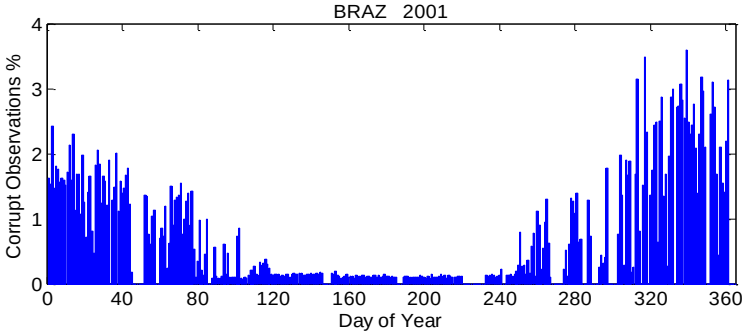

Figure 3.11 Daily occurrence of cycle slip for BRAZ station in 2001

Another example of cycle slip occurrence for a high latitude International GNSS Service (IGS) GPS station Yellowknife is shown in Figure 3.12. October 29 and 30 2003 are two days with severe geomagnetic storms within the whole Canadian region. The global Kp index for this period is shown in Figure 3.13. The average Kp value is higher than eight for the two disturbed days (Kp maximum possible value is nine). Accordingly the data for Yellowknife shows obvious high occurrence of GPS signal phase cycle slips for the two days time period. Both of the two examples in Figure 3.11 and Figure 3.12 show the occurrence correlation between ionospheric irregularities (present during the inferred high levels of ionospheric activity) and of corrupt observations at local IGS stations.

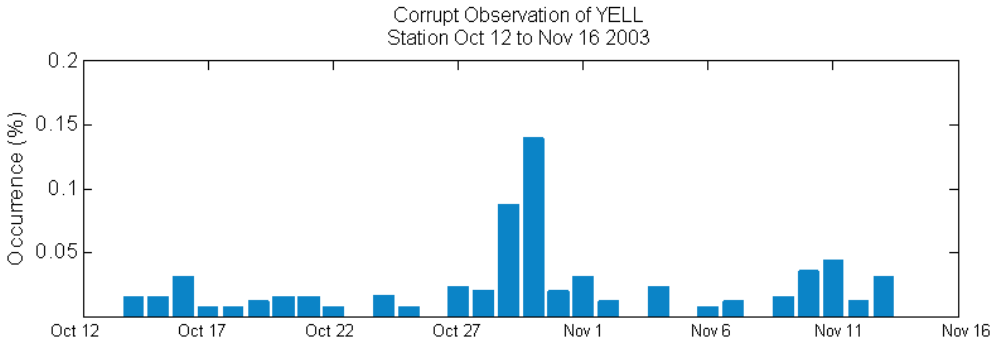

Figure 3.12 Daily occurrence of cycle slip for Yellowknife from October 14 to November 13 2003

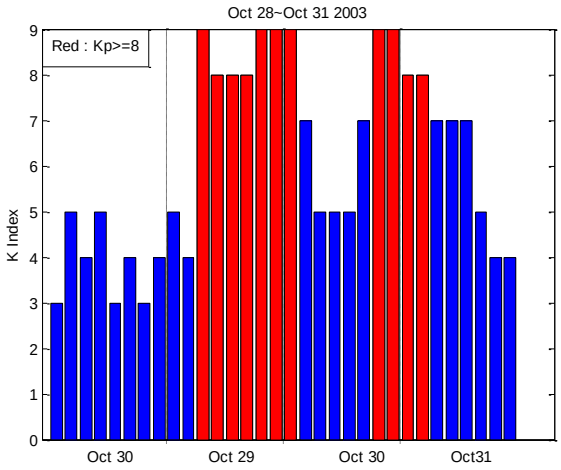

Figure 3.13 Kp index for October 28 to 31 2003

3.3.2.5 GPS POSITIONING ERROR

Scintillation effects can add perturbations and cause additional noise on GPS signals, with an impact on positioning accuracy. Correlation between scintillation intensity and position error have been studied by *Dubey et al.* [2005].

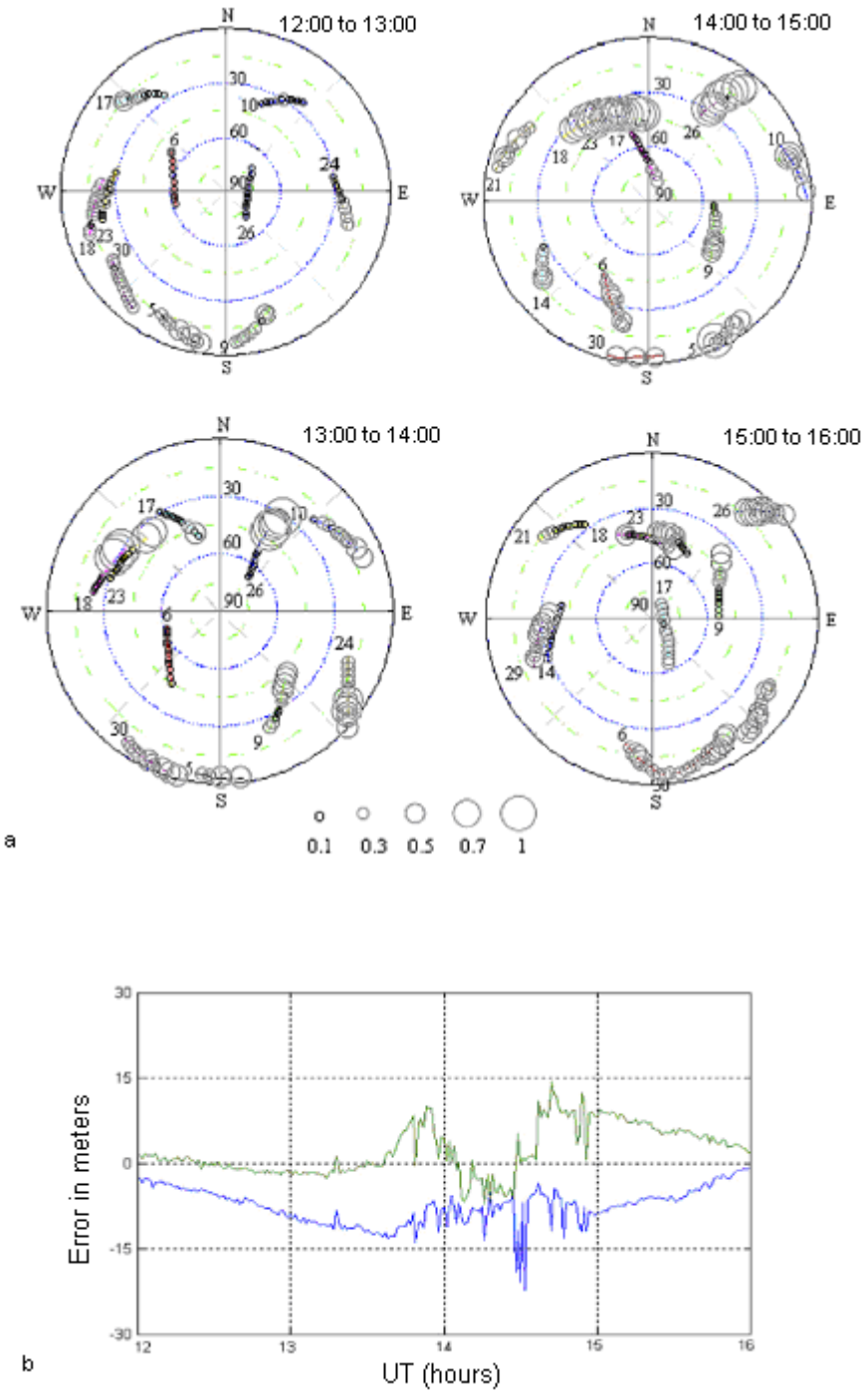

Figure 3.14 (a) Scintillation intensity (represented by size of circles) from 1200 to 1600 UT on March 19, 2001; (b) Latitudinal and longitudinal error of GPS position in meters [after *Dubey et al.*, 2006]. The blue line is latitudinal error and the green line is longitudinal error.

Figure 3.14 (a) shows the S4 plots for a GPS ionospheric scintillation monitor in the low latitude region (Chiang Rai, Thailand) 1200 to 1600 UT 19 March 2001. Figure 3.14 (b) shows the latitudinal and longitudinal variations of GPS positions for a fixed location nearby (19.6° N, 99.5° E). An intense scintillation period is observed between 1400 and 1500 UT (2100 to 2200 LT) with a maximum S4 index. The latitudinal error reaches 22 m and longitudinal error reaches 14 m [*Dubey et al.,* 2006]. This event is a typical case of equatorial irregularities causing scintillation after sunset during a solar maximum period.

3.3.2.6 FLUCTUATION OF RADIO OCCULTATION SIGNAL SNR

Figure 3.15 shows the SNR for GPS C/A code for a single CHAMP RO occultation event February 25, 2002. This is an event in the nighttime equatorial region. In the equatorial region after sunset the spread-F scintillation can be severe.

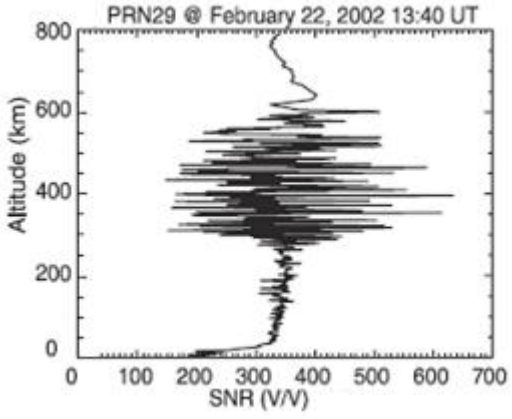

Figure 3.15 SNR plot for one radio occultation event for CHAMP on February 22, 2002 [after *Straus et al*., 2003]

In Figure 3.15 the C/A SNR fluctuates a large amount in the F layer altitudes (300-500 km); this is the result of irregularities in the F region ionosphere. Another scintillation event is observed in the high-latitude auroral region during a disturbed period. Figure 3.16 is the detrended RO signal SNR on July 10, 2005. The low-frequency trend of the profile is removed from the profile. High-frequency fluctuations are observed near 110 km altitude for both L1 and L2 signals; this corresponds to the AEI feature typical in the auroral region during substorms.

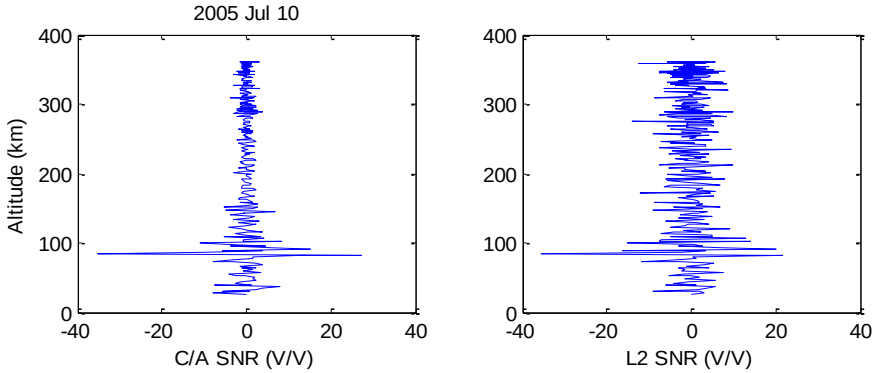

Figure 3.16 Detrended SNR plot for high-latitude radio occultation

CHAPTER 4

RADIO OCCULTATION TECHNIQUE

In this chapter general theory of radio occultation will be covered along with the Abel inversion retrieval method. The CHAMP and COSMIC missions are also introduced.

4.1 OVERVIEW OF RADIO OCCULTATION TECHNIQUE

Radio occultation missions such as CHAMP and COSMIC are used to sound the earth's neutral atmosphere and ionosphere via a radio link between a GPS navigation satellite and GPS receivers equipped on low Earth orbiter (LEO) satellites [*Lee et.al.*, 2001; *Gorbunov*, 1996]. Initially, radio occultation satellites were launched to sound other planets' atmospheres and surfaces in our solar system. The United States GPS meteorology (GPS/MET) experiment was the first mission to apply the radio occultation technique to the Earth successfully using GPS signals. Figure 4.1 is a diagram illustrating the RO technique. The direct radio link between the GPS and LEO satellite is occulted by the Earth's limb; as the electromagnetic radiation passes through the atmosphere it is refracted. The link between the two satellites can be maintained due to the refraction of signal. Signals received by the GPS receiver onboard the LEO includes propagation delays due to properties of the given atmospheric layer.

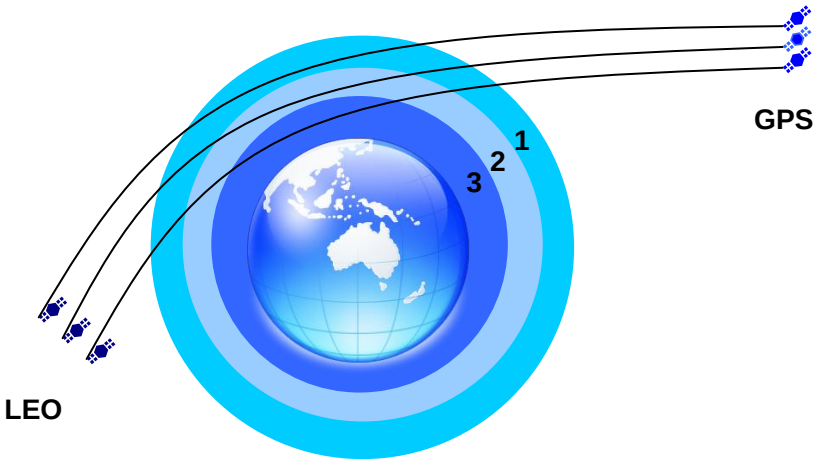

Figure 4.1 Concept of radio occultation observations

The magnitude of the refraction depends on the nature of the atmosphere. The bending of the signal is usually determined by the neutral components in the atmosphere or ionospheric electron density. As the LEO-GPS line-of-sight is occulted by the Earth's limb with the setting (or sometimes rising) movement of the LEO satellite, the GPS-LEO radio link successively scans the atmospheric layers at different altitudes. Refractivity profiles of the atmosphere are retrieved from such GPS-LEO signal observations by applying the Abel inversion; the fundamental observation for this processing is the excess phase delay caused by the propagation medium. As illustrated in Figure 4.1, for example, the earth's atmosphere can be assumed to consist of multiple layers; each layer is sounded by the RO signal successively as the GPS-LEO line-of-sight moves downward. The refractivity gradient of the first layer is later used to calculate the refractivity of the second layer, and the first and the second sounding provide the refractivity information to calculate the third layer's refractivity. Therefore, layer by layer, the vertical refractivity profile will be estimated as if peeling layers of an onion. The method of retrieving electron density will be explained in detail in the next section. Effects of the atmosphere on radio occultation signals are summarized by *Hajj et al.* [2002].

Atmospheric and ionospheric effects cause the change of signal and are measured to reveal information about atmospheric properties for different layers. Investigations have already proven that the accuracies of RO atmospheric retrieval parameters are comparable, if not better, than other traditional sensing methods [*Hajj et al.*, 2002]. Radio occultation techniques provide promising application in meteorology, climatology and ionospheric physics.

LEO-GPS missions are able to obtain vertical profiles of refractivity, density, pressure, temperature and water vapor pressure in the neutral atmosphere and electron density in the ionosphere. Applications include climate change detection, numerical weather predictions, gravity wave morphology studies, and ionospheric tomography. With more missions being conducted (and proposed), radio occultation techniques are expected to provide the advantage of all-weather, global coverage, high vertical resolution and long-term stability.

4.2 CHAMP AND COSMIC MISSIONS

4.2.1 CHAMP

The German CHAMP (CHAllenging Minisatellite Payload) satellite was launched from Plesetsk, Russia on July 15, 2000 by a COSMOS rocket. The primary purpose of this mission is precise gravity studies, magnetic field measurement and atmosphere/ionosphere sounding by radio occultation techniques [*Jakowski et al.*, 2002]. It carries the latest RO receiver from JPL (Jet Propulsion Laboratory, USA). The GPS flight receiver (“BlackJack”) is specially designed for radio occultation

sounding purposes. The enhanced L2 signal noise introduced by GPS antispoofing is reduced by the application of a high-gain GPS antenna to some extent, with higher signal to noise ratio than normal receivers [*Wickert et al.*, 2001]; this reduces the impact of GPS antispoofing effects on CHAMP's LEO receiver.

The CHAMP satellite orbit is almost circular and near-polar which is designed for homogeneous and better global coverage to remotely sense the earth's atmosphere with an inclination angle of 87.2° and initial altitude of 454 km [*Wickert et al.*, 2005]. The first CHAMP profiling experiment commenced operating on 11 February 2001 [*Wickert et al.*, 2001] and CHAMP continues to operate. CHAMP data are available at various levels and are publicly available at the CHAMP Information System and Data Center (ISDC) at the GFZ website: http://op.gfz-potsdam.de/champ. CHAMP data can be divided into three types: Atmosphere/Ionosphere, Orbit/Gravity, and Magnetic/Electric Field. Various levels of data exist in all three categories. Table 4.1 provides the classification of Atmosphere/Ionosphere CHAMP data. In this catalog the phase observations of L1 and L2 for the LEO onboard receiver and ground receiver are available in Level 1. The excess phase delay product, which is used to retrieve atmospheric parameters - such as electron density - is a Level 2 product.

The occultation table which provides a list of occultation events by date and time is in Level 2. In Level 3 the final products such as parameters of neutral atmosphere, electron density, and TEC along the GPS-LEO line of-sight are available. An average delay of 3 to 4 hours exists between measurements onboard CHAMP (Level 1) and the provision of the analysis data (excess phase of Level 2) [*Wickert et al.*, 2005].

Table 4.1 Classification of CHAMP Data under Atmosphere/Ionosphere Category [*ISDC*, 2009]

	Product type	**Description**	**Format**
Level 1	CH-A1-1-GPS-01S	High rate GPS ground tracking data, 1 Hz	RINEX 2.20
	CH-A1-1-HR	High rate CHAMP GPS-SST, 50 Hz,	RINEX 2.10
	CH-A1-1-MR	Medium rate CHAMP GPS-SST, 1Hz	RINEX 2.10
Level 2	CH-A1-2-PD	Atmospheric excess path delay	ASC II
	CH-A1-2-TAB	Occultation tables	ASC II
Level 3	CH-A1-3-ATM	Atmospheric parameters	ASC II
	CH-A1-3-IVP	Vertical electron density profiles	ASC II
	CH-A1-3-TCR	Occultation link related TEC data	ASC II

For ionosphere altitudes the resolution is from 0.5 to 3 km for 1 Hz data and approximately 30 m for 50 Hz data; this depends on the vertical RO ray path velocity. Moreover the altitude coverage is different between 50 Hz and 1 Hz products. The 50 Hz data usually starts around 130 km altitude, and is mainly used to measure the troposphere parameters and detect the sporadic E layer, while 1 Hz data starts around 400 km altitude and covers the ionospheric F1 region. There are approximately 200 to 250 CHAMP radio occultation events per day with locations distributed across the earth's surface depending on the satellite's ephemeris [*Wickert et al.*, 2001]. The CHAMP orbit changes the local time coverage by approximately 5.6 min per day for the equatorial region. It covers the 24 hour cycle for 130 days. The pattern repeat period could be shorter since the broad antenna field of view for CHAMP's RO receiver can possibly allow occultation from GPS satellites within ± 1 hour [*Wu*, 2006].

4.2.2 COSMIC

The newer COSMIC (Constellation Observing System for Meteorology Ionosphere and Climate) is a six identical FORMOSAT-3 satellites mission [*Schreiner et al*. 2007; *Anthes et al*., 2008]. All six satellites shared the same initial orbit at an altitude of 500 km. At the initial altitude the six satellites orbited very close to each other. This feature gave the opportunity to compare radio occultation data for different FORMOSAT satellites measuring the same parameters in close proximity. These types of observations can be used to estimate the precision of RO observations to some extent [*Anthes et al*., 2008].

The final orbit for the COMSIC satellites is Right Ascension of Ascending Node (RAAN) with an orbit altitude of 800 km. FM5 was the first satellite that reached the RAAN orbit. Satellites FM2 and FM6 arrived RAAN in February 2007. Figure 4.2 shows the history of FORMOSAT satellites' altitude until end of 2007. The FORMOSAT satellites become a dispersed distribution in local time after they reach the final orbits. Initially the satellites' configuration was designed for 24° separation between adjacent orbital planes. Later this was modified to 30° to obtain a more uniform global coverage [*Liou et al.*, 2007].

Each FORMOSAT satellite carries a GPS Occultation Experiment (GOX) payload developed by JPL. The GOX receiver is designed for open loop tracking. Another two payloads are also carried by all the COSMIC satellites: one is the Tiny Ionospheric Photometer (TIP) for electron density monitoring; the other is a Tri-Band Beacon (TBB) for ionospheric tomography and scintillation studies [*Ledvina et al.*, 2004].

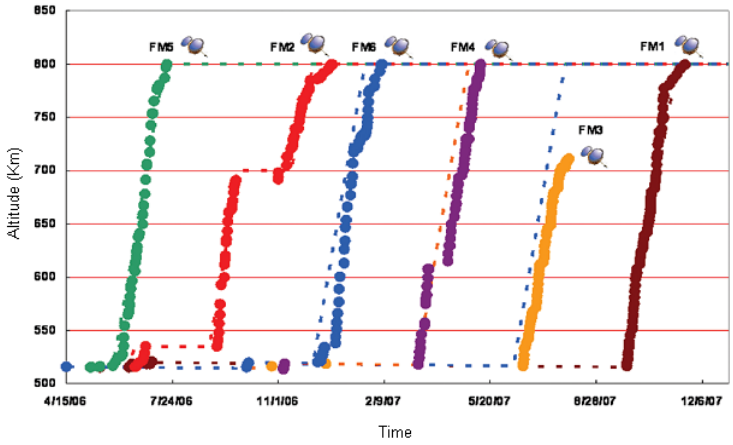

Figure 4.2 History of FORMOSAT-3/COSMIC's orbit altitude [after *Fong et al.*, 2008]

CDAAC (COSMIC Data Analysis and Archive Center) strives to combine the different data types to provide more accurate electron density profiles for ionospheric research purposes. Currently approximately 4000 globally distributed occultation events are provided each day; after quality control around 2500 remain. This offers much better spatial coverage than former RO missions. COSMIC data are available at http://cosmic-io.cosmic.ucar.edu/cdaac/. More options are provided for COSMIC products downloading than CHAMP; for example COSMIC has scintillation measurements available. Generally the high-level data products still include the following: profiles of temperature, pressure, humidity, refractivity, bending angles, and ionospheric electron density; and TEC. CDAAC aims to deliver the high quality data products within three hours [*COSMIC*, 2009]. COSMIC satellites' orbital periods are 100 minutes.

The COSMIC constellation mission, with its advanced technologies, was expected to provide near real time products, with global coverage, for different altitude observations of temperature, pressure, refractivity, water vapor, and ionospheric electron density [*Liou et al.*, 2007]. However this objective has not been maintained.

Figure 4.3 shows the COSMIC RO observation coverage for 100 min centered at 14:00 UT March 4, 2007. Different colors represent observations from different FM satellites. It is observed that not all the longitude sectors are covered during the specified 100 min.

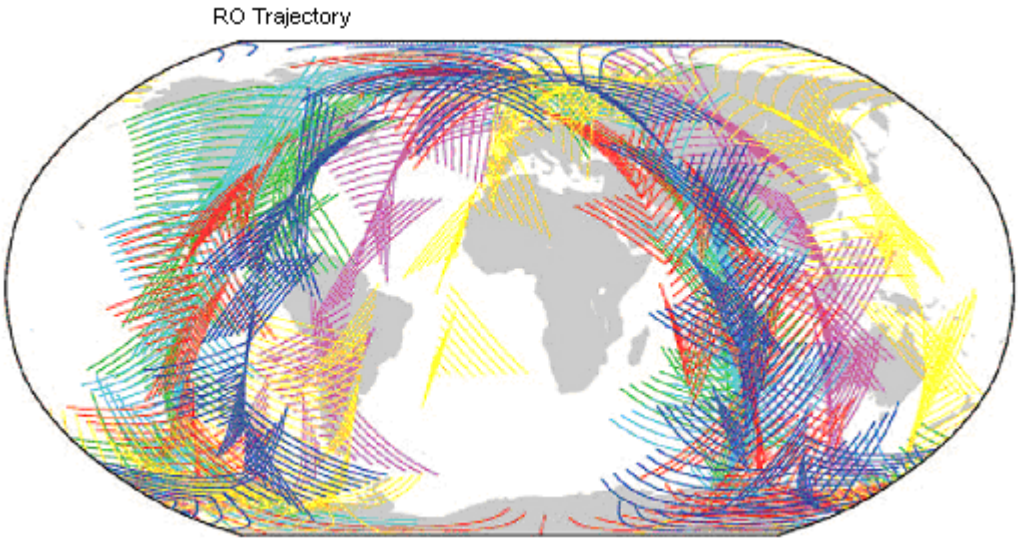

Figure 4.3 Transionospheric radio links between COSMIC satellites and GPS for 100 min, centered on 14:00 UT March 4, 2007. [after *Anthes et al.*, 2008]

A follow-up mission COSMIC II has been proposed. Improvements include processing of Galileo/GLONASS satellite signals. The latency of data processing is also expected to be greatly reduced. And a more improved tracking capability and antenna gain will allow lowest altitude moist troposphere sensing. Finally COSMIC II will also provide 12 additional LEO satellites in space. The future COSMIC II will be more challenging and powerful for ionospheric research and space weather forecasting.

4.2.3 COMPARISON BETWEEN CHAMP AND COSMIC

This section compares two aspects - observation coverage, and altitude range - between the CHAMP and COSMIC missions.

Orbital Altitude

The COSMIC satellites' altitude is much higher than that for CHAMP, which results in observations obtained at F2's higher altitude for the COSMIC mission. An example is shown in Figure 4.4 for comparison of ionospheric electron density products for 1 Hz observations of CHAMP and COSMIC on 28 September 2006. In Figure 4.4 it is observed that the FM2 orbit is about 700 km and the FM5 orbit is 800 km on the given date. The altitude range of observations in Figure 4.4 basically reflects the LEO altitudes (since the GPS satellite orbits are much higher). Altitudes for CHAMP observations are all below 400 km, which makes parts of the ionospheric F2 region invisible (F2: 200 - 900 km). Currently all FORMOSAT satellites of COSMIC have reached their final orbits; the range of all COSMIC satellites observations extend to altitudes around 800 km.

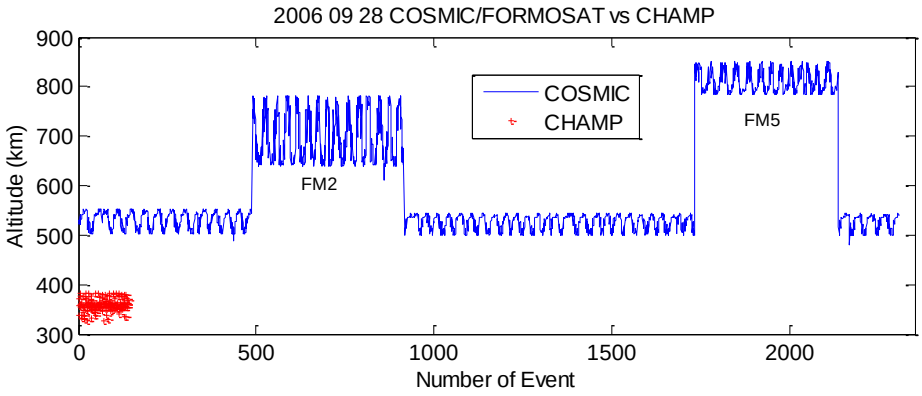

Figure 4.4 Starting altitude for 1 Hz electron density product by COSMIC and CHAMP on September 28, 2006

Observation Coverage

From Figure 4.4 it can be observed that COSMIC has more records for electron density product than CHAMP on a single day. This is due to the number of LEOs available: COSMIC mission has a constellation of six satellites and CHAMP is a one-satellite mission. Observation coverage for one day (September 28 2006) is shown for COSMIC and CHAMP in Figures 4.5 and 4.6. There are 3937 events for COSMIC and 814 for CHAMP before the quality control. In Figure 4.6 it is observed that for one day the observations of CHAMP are sparse and cannot provide global overage compared with COSMIC. There is a very distinct longitude selection for CHAMP.

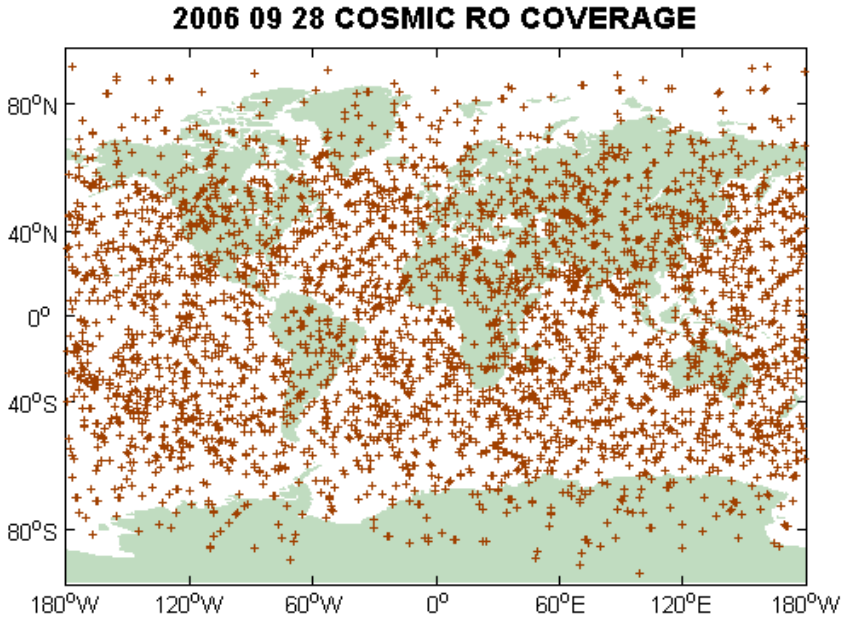

Figure 4.5 COSMIC observations coverage on September 28, 2006

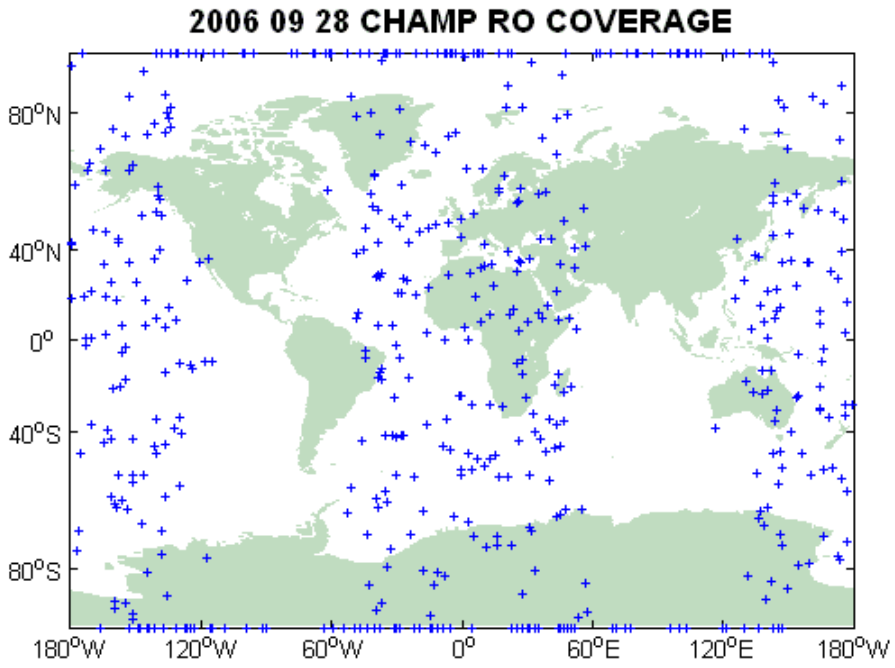

Figure 4.6 CHAMP observations coverage on September 28, 2006

4.3 RADIO OCCULTATION DATA PROCESSED BY CDAAC

For RO missions (eg: COSMIC, CHAMP) there are generally two kinds of data rates provided. One is 50 Hz for lower atmosphere (troposphere) observations and the other is 1 Hz for ionosphere observations. Spatial resolution is directly dependent on data rate. An example of a CHAMP RO event is shown in Figure 4.7. Usually 1 Hz data can cover the major part of the ionosphere (e.g. F layer) with adequate spatial resolution while the 50 Hz data with higher resolution can only provide observations for lower E and D region. The lack of high rate observations for the ionosphere F region arises from considerations of data management onboard the satellite.

CDAAC (COSMIC Data Analysis and Archival Center) has developed a GPS RO data processing system for COSMIC. The retrieval methods are introduced with reference to information provided on the CDAAC website [*COSMIC*, 2009].

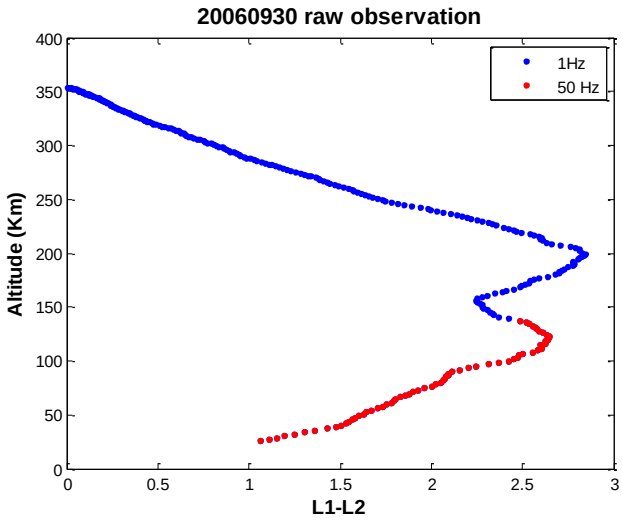

Figure 4.7 Altitude coverage of 1 Hz (blue) and 50 Hz (red) observations for one RO event from CHAMP dataset

4.3.1 ALGORITHMS FOR RADIO OCCULTATION INVERSIONS IN THE IONOSPHERE

For COSMIC, the inversion method for ionosphere radio occultation is based on an assumption of local spherical symmetry. The assumption is that the electron density within a few thousand kilometers radius around the tangent point of the ray path is locally spherically symmetric. This assumption cannot always be valid since it ignores the physical presence of horizontal density gradients. The retrieved electron density profile may have errors in cases when ionospheric conditions differ greatly from assumptions. In particular, for altitudes below the E region negative values can often

be found in the density profiles generated by CDAAC. Another issue of note is that the vertical electron density profile is determined for different horizontal geographic locations of the ray path bottom versus top; the horizontal distance bottom versus top of the profile can be one hundred kilometers. The profile does not represent the ionosphere for the same longitude and latitude at different altitudes.

Phase measurements of the RO signal are fundamental observations necessary to derive the refractivity. The refractivity is then used to derive the electron density profile in the ionosphere (or temperature and pressure profile in the neutral atmosphere). Abel inversion is a common technique for processing RO data which is sensitive to vertical structures. The GPS/MET mission was the first to perform the application of Abel inversion to RO retrieval. Usually there are two types of retrieval based on different kinds of observations. One is based on bending angle. The other is based on slant total electron content (STEC) observations [*Garcia-Fernandez*, 2002; *Schreiner*, 1999]. Only the second method is introduced here.

4.3.1.1 ABEL INVERSION

In physics or engineering it is common to have two functions such that one is the integration of the other: $f(a) = \int_a^b g(t)K(\omega,t)dt$. The function $f(a)$ is the integral transform of the function $g(t)$. As the integral transforms comprise a special subset of the equations, the inverse transform can be found as follows: $g(t) = \int_\alpha^\beta f(a)\kappa(\omega,t)da$. One of the widely used integral transforms is the Fourier transform. Abel transform is another one that has requirements for both of the functions. The Abel transform is widely applied for atmospheric profile retrievals using radio occultation observations.

The general transform can be defined as follows:

$$f(a) = \int_0^\infty g(r)K(r,a)dr \tag{4.1}$$

where $K(r,a) = \begin{cases} \dfrac{2r}{\sqrt{r^2 - a^2}} & if \quad r > a \\ 0 & otherwise \end{cases}$

or alternatively $$f(a) = \int_a^\infty g(r)\frac{2r}{\sqrt{r^2 - a^2}} \tag{4.2}$$

In many applications the function $f(a)$ is an abscissa function and $g(r)$ is a radial function. The variables r and a represent a radius and an abscissa respectively. An inverse Abel transform exists in the form

$$g(r) = -\frac{1}{\pi}\int_r^\infty \frac{f'(a)}{\sqrt{a^2 - r^2}}da \tag{4.3}$$

For more description of Abel inversion one can refer to [*Eshleman,* 1973] and [*Hinson et al.*, 1998]. For GPS RO usually $g(r)$ is the electron density as a function of altitude and $f(a)$ is the TEC measurement along the GPS-LEO ray. The Abel inversion is applied to electron density retrieval and will be discussed in the next section.

4.3.1.2 INVERSION USING SLANT TEC MEASUREMENTS

Inversions based on slant TEC measurements should assume that the LEO-GPS ray bending angle is very small. For the ionospheric F region altitude this assumption is valid. The inversion based on slant TEC (STEC) is an onion-peeling method as

illustrated in Figure 4.1. Details of this method can be found in *Garcia-Fernandez* [2002] and *Schreiner et al.* [1999]. For electron density retrieval by CDAAC this method is used instead of using inversions from bending angle.

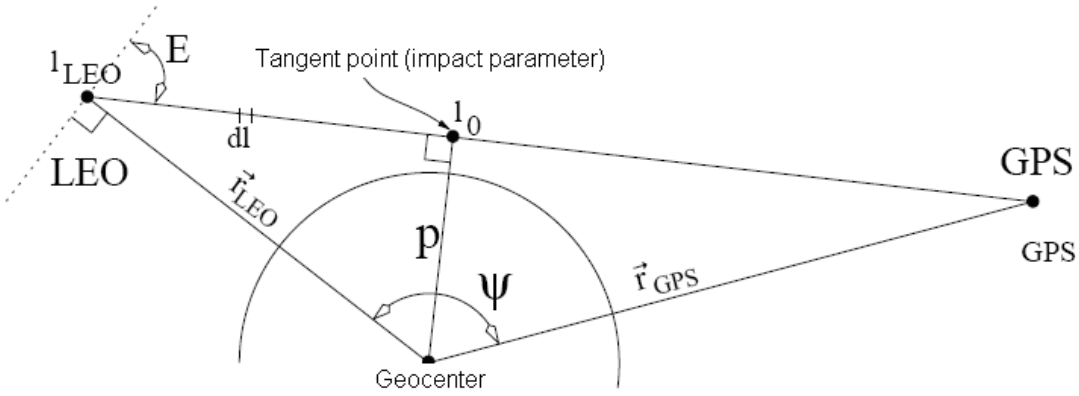

Figure 4.8 Illustration of occultation geometry with straight line GPS-LEO ray [after *Garcia-Fernandez*, 2002]

Total electron content (TEC) along the GPS-LEO ray can be expressed as follows.

$$TEC = \int N dl = -\frac{f^2}{40.3\times 10^6}\int (n-1) dl = -\frac{f^2 S}{40.3} \qquad (4.1)$$

where N is electron density, n is the ionospheric index of refractivity and S is the excess phase product (which is obtained directly from COSMIC data archives). TEC can be calculated from either L1 or L2 excess phase observations or from a linear combination of both:

$$\mathrm{TEC} = -\frac{f_1^2 S_1}{40.3} = -\frac{f_2^2 S_2}{40.3} = -\frac{f_2^2 S_2}{40.3} = \frac{1}{40.3}\left(\frac{1}{\frac{1}{f_2^2}-\frac{1}{f_1^2}}\right)\left(S_1 - S_2\right) \qquad (4.2)$$

TEC computation from a single frequency observation contains effects of orbital motion and drifts of GPS transmitter and receiver clocks; these must be estimated

through additional processing using ground reference data. For dual frequency TEC calculations the orbit and clock error are eliminated in formation of the dual-frequency linear combination - due to the fact that such errors are identical for L1 and L2 measurements. However in formation of the dual-frequency combination additional noise (primarily from L2) will be introduced into TEC estimates. This error can be neglected in the future with improved civilian L2 signals from GPS modernization efforts. TEC along the GPS-LEO link in Figure 4.8 is expressed as

$$STEC(p) = \left[\int_{l_0}^{l_{LEO}} + \int_{l_0}^{l_{GPS}} \right] Ne(r)dl = \left[\int_{l_0}^{l_{LEO}} + \int_{l_0}^{l_{GPS}} \right] \frac{Ne(r)r}{\sqrt{r^2 - p^2}} dr \qquad (4.3)$$

where r is the altitude of LEO satellite and p is the tangent point altitude. $Ne(r)$ is the electron density along the line of LEO-geocenter. With the assumption of spherical symmetry, STEC along the GPS-LEO ray is transformed into the density profiled along the LEO and geocenter line. The electron density above the GPS satellite is also neglected in calculations. The spherical symmetry assumption will introduce error since the ionosphere can have large horizontal gradients within several kilometers as small ionospheric irregularity exists. The validation of Abel inversion for electron density products of radio occultation is discussed in Chapter 5. It is assumed that STEC from tangent point of the GPS satellite is the same as STEC from tangent point to LEO in Figure 4.8 and expressed as

$$STEC = (*)2 \left[\int_{l_0}^{l_{LEO}} \right] \frac{Ne(r)r}{\sqrt{r^2 - p^2}} dr \qquad (4.4)$$

The Abel inversion is applied to this formulation and the retrieval process is conducted using the following equation.

$$N_e(r) = -\frac{1}{\pi}\int_{r}^{r_{LEO}} \frac{dSTEC(p)/dp}{\sqrt{p^2 - r^2}}\,dp \tag{4.5}$$

In processing conducted by CDAAC to retrieve the electron density, the measured and calibrated TEC is inverted to an electron density profile using the onion peeling method:

$$N_e(p_i) = \frac{3}{4}\frac{TEC(p_i)}{\sqrt{2p_i(p_{i+1} - p_i)}} - \sum_{k=1}^{n-i} c_{k,i} N_e(p_{i+k}) \tag{4.6}$$

where the coefficients, $c_{k,i}$ are derived in *Syndergaard et al.* [2004], N_e is the electron density, and p is the impact parameter. Index i stands for different layers in the ionosphere. Usually the electron density obtained for higher altitude layers will be used to retrieve electron density for lower altitude layers during a RO event. For more about the ionospheric electron density retrieval method one can refer to the documentation on CDAAC website [*COSMIC*, 2009].

CHAPTER 5

VALIDATION OF RADIO OCCULTATION OBSERVATIONS BY GROUND OBSERVATIONS

5.1 GROUND OBSERVATIONS

In addition to radio occultation observations from COSMIC and CHAMP, several complementary high-latitude datasets are used in the studies presented here. This chapter contains a brief introduction to the ground datasets. Some datasets are used for validation; other datasets are used in later chapters to identify the presence of ionospheric disturbances.

5.1.1 SCINTILLATION OBSERVATIONS

Since 2003 the University of Calgary has operated several GPS scintillation receivers in Canada. Scintillation is recorded by three GPS receivers as part of CANGIM (CANadian GPS Network for Ionosphere Monitoring). The receivers are NovAtel Euro4 receivers capable of deriving phase and amplitude scintillation information. Figure 5.1 shows their locations. The three stations are almost aligned along the same meridian at different latitudes spanning the sub-auroral, auroral and polar cap regions (depending on level of ionospheric activity). Yellowknife is a high latitude site where aurora is commonly observed. In this thesis nightside auroral scintillation conditions are identified from the extensive CANGIM GPS dataset.

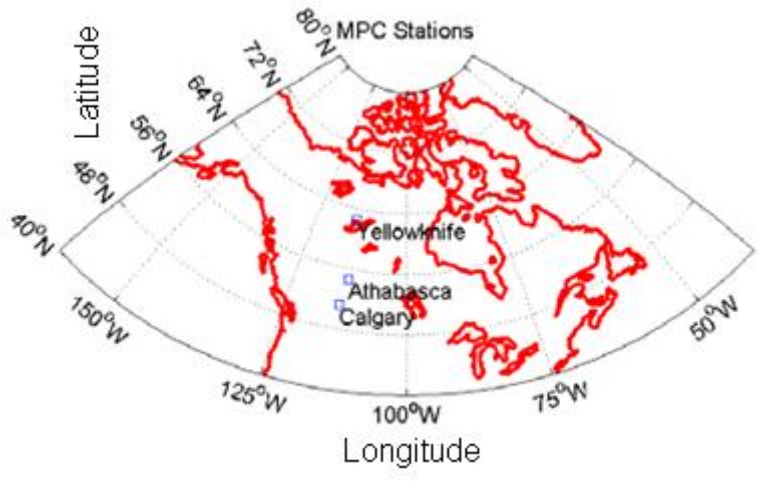

Figure 5.1 Geodetic locations of three scintillation GPS receivers: Calgary, Athabasca, Yellowknife [*Skone et al.*, 2008]

5.1.2 MAGNETOMETER OBSERVATIONS

The level of magnetic activity is recorded in magnetometer observations. Local magnetometer observations are more related to local ionospheric disturbed conditions than the global Kp geomagnetic index. There are two websites with relevant publicly available magnetometer datasets. One is maintained by GSC (Geological Survey of Canada): http://geomag.nrcan.gc.ca. The other is the CSSDP (Canadian Space Science Data Portal): http://portal.cssdp.ca. GSC and CSSDP magnetometer sites are shown in Figures 5.2 and 5.3 respectively. CARISMA (Canadian Array for Realtime Investigations of Magnetic Activity) stations from CSSDP are shown. There are sites along the same meridian (from TALO to PINA) in CARISMA; these are used to infer the auroral oval boundaries.

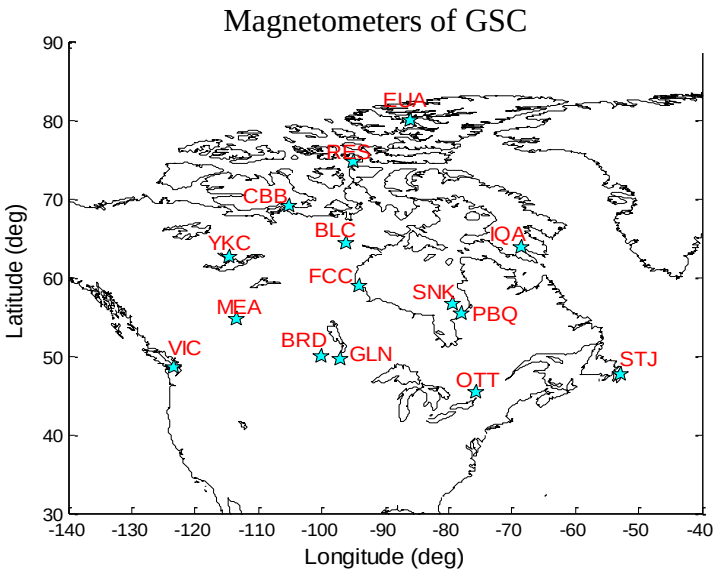

Figure 5.2 Geodetic locations of GSC Observations

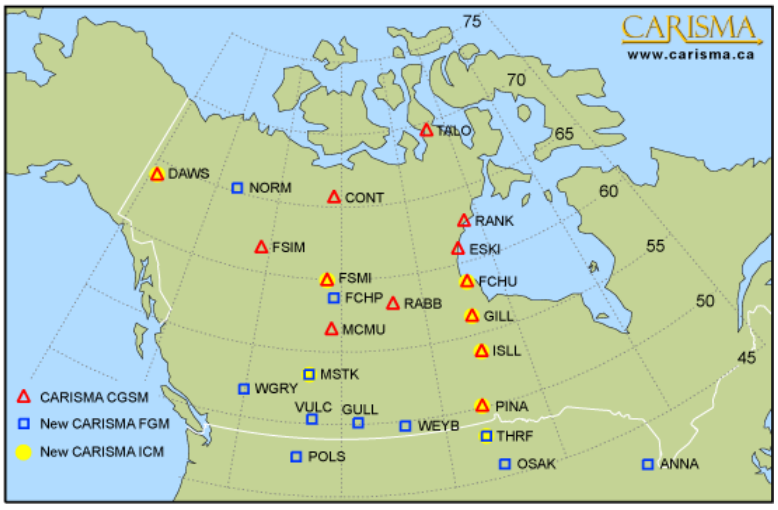

Figure 5.3 Geodetic locations of CARISMA magnetometers [*CARISMA*, 2009]

Another magnetometer array called GIMA (Geophysical Institute Magnetometer Array) is also used to validate the disturbed ionospheric conditions. These sites are close to the incoherent scatter radar PFISR in Alaska.

5.1.3 INCOHERENT SCATTER RADAR

Incoherent Scatter Radar (ISR) data are used to validate the electron density profiles from radio occultation. ISR data can be downloaded from the Madrigal database maintained by Haystack Observatory. Madrigal is a database of ground-based measurements and models of upper atmosphere and ionosphere [*AMISR*, 2009].

Locations of the world's incoherent scatter radars are shown in Figure 5.4 [*Haystack*, 2009]. The AMISR at top left of the map is in Poker Flat ISR (PFISR) in Alaska.

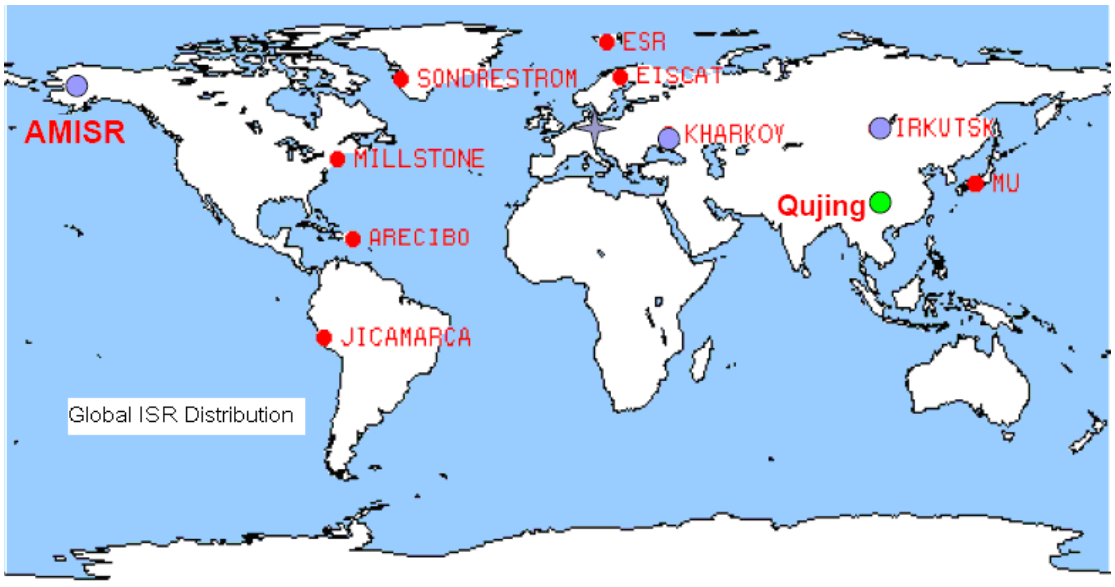

Figure 5.4 Geodetic locations of ISR instruments [after *Haystack*, 2009]

All such ground-based instruments assist in the analysis of radio occultation capabilities. In the following section RO measurements are validated by ISR and ionosonde. For the purposes of this thesis only measurements for ionosphere (no troposphere) are validated.

5.2 VALIDATION BY INCOHERENT SCATTER RADAR

5.2.1 PUBLISHED VALIDATION

Incoherent scatter radar can be used to validate radio occultation electron density measurements - since it can provide the whole electron density profile. *Lei et al.* [2007] compared electron densities from COSMIC RO observations with ISR. Data from June 27 to July 1 and September 20-22 2006 at Millstone Hill and Jicamarca were used.

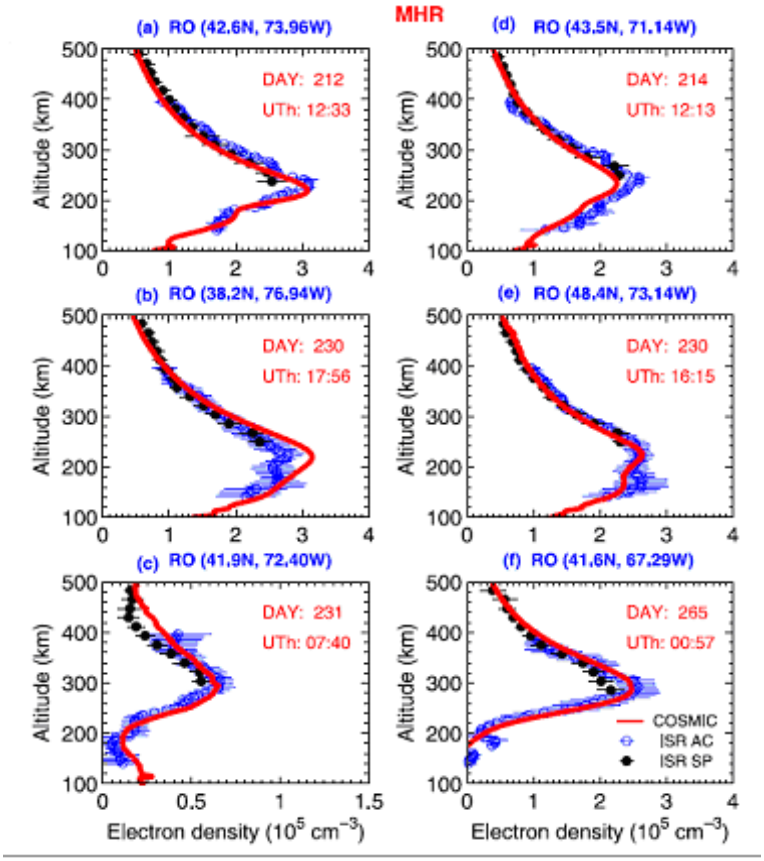

Figure 5.5 Six comparisons of electron density profiles between COSMIC RO (solid lines) and Millstone Hill ISR (circles). Error bars are standard deviations for the ISR data over 1 hour [after *Lei et al.*, 2007]

Radio occultation events with tangent points at the F2 peak height within 6° latitude and 6° longitude of the ISR data were selected. The time bin for selection is 1 hour. Figures 5.5 are 5.6 are typical events from Millstone. Good agreement was found between the two observation tools. COSMIC retrieved electron density profiles are within the ISR error bars except in Figure 5.5 (b) where COSMIC measurements are larger than ISR by 15%. Differences in the profiles arise from three factors: 1) mis-collocation between two measurements; 2) incorrect spherical symmetry assumption in RO inversion; and 3) ISR measurement noise [*Hajj et al.*, 2000]. Another comparison case was shown by *Hajj et al.*, [1998] for GPS/MET radio occultation and the Millstone ISR in 1998 (Figure 5.6). Both of the comparisons demonstrated general good agreement for the F2 peak at approximately 350 km altitude. In these cases the ISR profiles capture the same profiles as radio occultation observations. Comparisons were conducted only for a limited number of cases since it was not easy to find RO at the same location of ISR during the same period. Statistical analysis with an extensive ISR validation dataset has not been conducted.

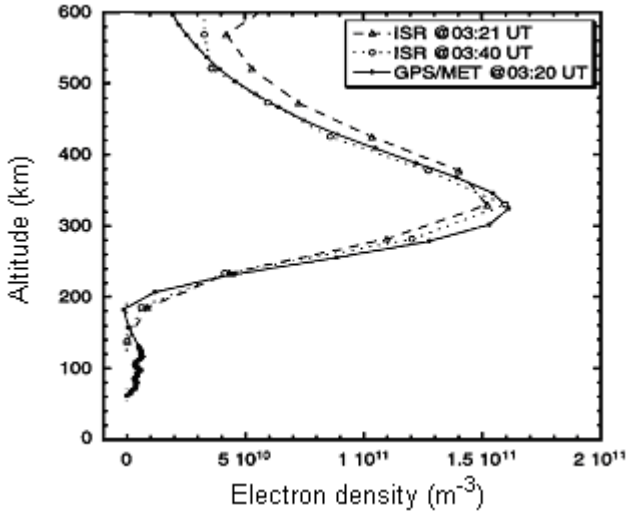

Figure 5.6 Electron density profile comparison between GPS/MET and Millstone Hill ISR [after *Hajj et al.*, 1998]

5.2.2 VALIDATION UNDER DISTURBED CONDITIONS

5.2.2.1 COMPARISON WITH INCOHERENT SCATTER RADAR OBSERVATIONS

Validation in the previous section was not specified for active ionospheric conditions. However, for the purposes of this thesis, the accuracy of RO measurements under "disturbed" ionospheric conditions must be determined. Validation by high-latitude PFISR and EISCAT ISR is conducted for selected disturbed RO events. Events are selected with obvious AEI features being observed during auroral nighttime. Poker Flat ISR (PFISR) is at (65.12° N, 212.56° E); this is an auroral latitude in Alaska. PFISR has operated continuously since March 1 2007. The EISCAT ISR is at (77.90° N, 16.00° E) in the polar cap region; this is usually poleward of the auroral oval. Calibrated PFISR and EISCAT ISR electron density profiles for 2007 and 2008 are selected for periods during which magnetic disturbances were observed in local magnetometer observations.

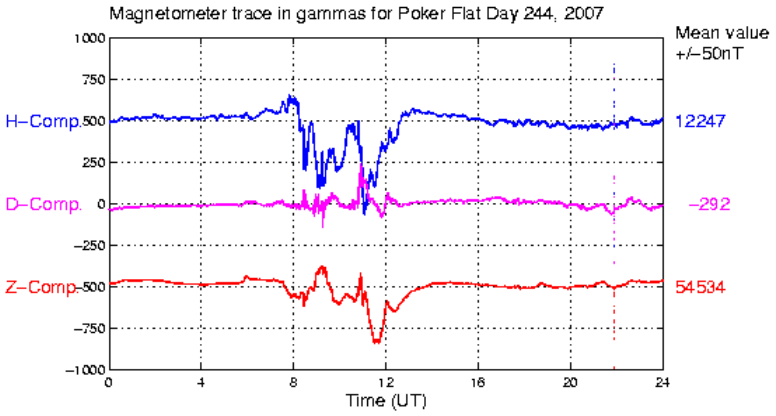

Figure 5.7 Magnetic field measured near Poker Flat (PFISR) on September 1 2007, [*GIMA*, 2009]

Concurrent and co-located COSMIC measurements with median tangent points for one event within 6° latitude and 6° longitude of the Alaskan ISR (PFISR) location are selected for comparison. For example, severe aurora were observed nightside in Canada on September 1 2007. GIMA magnetometer observations near PFISR are shown in Figure 5.7 [*GIMA*, 2009]. The electron density profile comparison is shown in Figure 5.8 for a 0958 UT event. Radio occultation tangent points and PFISR beam locations are shown in Figure 5.9. Red lines represent the PFISR beams mapped into two dimensions for the ISR operation.

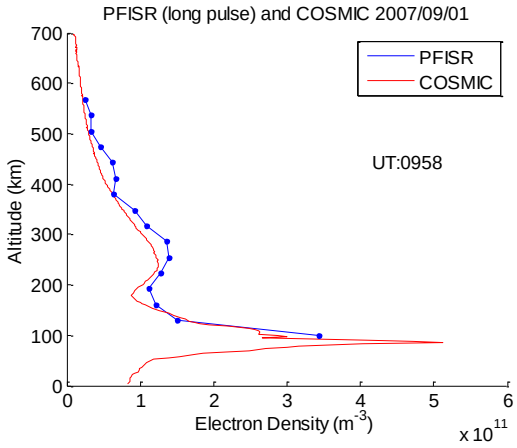

Figure 5.8 Electron density profiles from COSMIC and PFISR 0958 UT 1 September 2007

Figure 5.10 shows both the COSMIC retrieved electron density profiles and the corresponding ISR profiles at PFISR or EISCAT for four "disturbed" events. It can be observed that (at approximately E region altitudes of 100 km) the RO-retrieved AEI feature is generally in good agreement with PFISR ISR data. All four comparisons demonstrate general consistency for the altitude range of E layer precipitation.

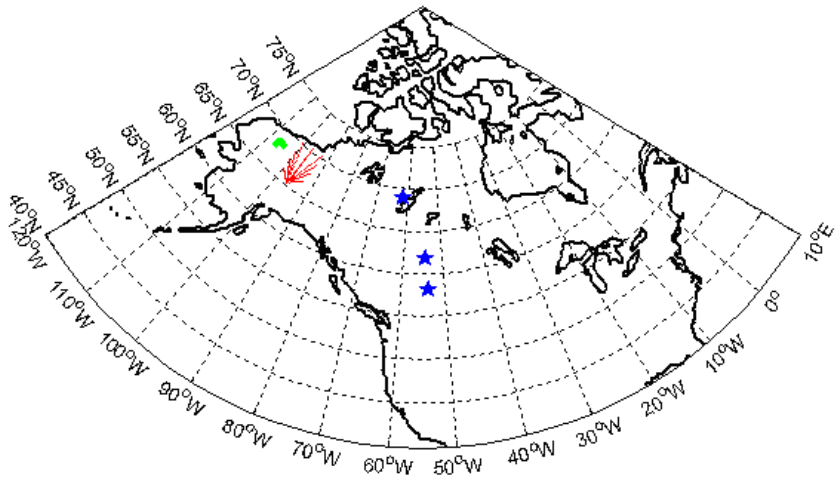

Figure 5.9 Geomagnetic locations of RO event (green) slant beams of PFISR (red), and three CANGIM scintillation receivers (blue stars)

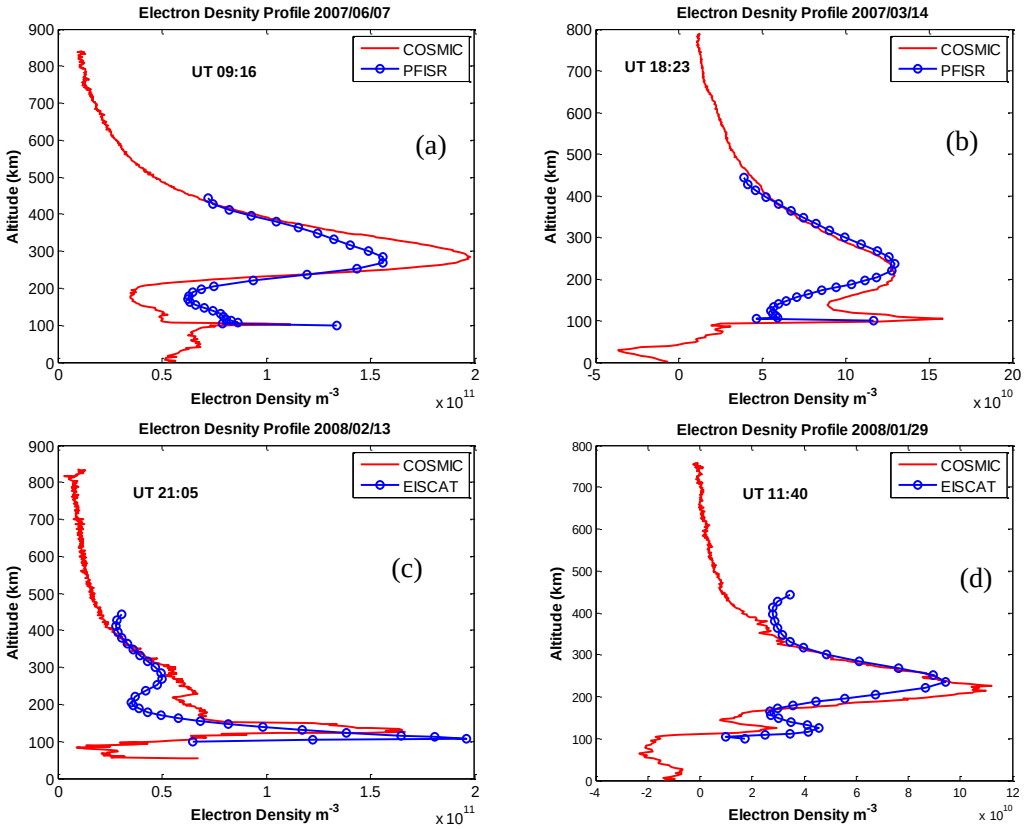

Figure 5.10 Comparison of COSMIC electron density profiles (red) near ISR with those measured by ISR concurrently (blue) (a, b, c, d)

However the values of AEI peak electron density are not identical for the two types of observations, especially for case (c). It is noted that the RO events are not exactly co-located with ISR observations. RO events do not occur coincidentally above the ISR sites. And during nighttime auroral conditions the electron density irregularities at 110 km altitude associated with AEI can be quite localized: the horizontal scale size ranges from 20 to 400 km [*Coker et al.*, 1995]. The geographic location of the RO ray path tangent points for one RO event can change by several hundred kilometers beginning (top) versus end (bottom) of the profile.

Therefore the differences between observations in the E region may arise from the localized nature of the irregularity and location mismatch between the two types of observations. The assumption of local spherical symmetry of electron density in a large region could be another error source for RO inversion. This assumption becomes inadequate under disturbed ionospheric conditions since horizontal ionospheric gradients are present in the nighttime aurora.

There is also some disagreement in the Figure 5.10 COSMIC and ISR profiles at F region altitudes. The most obvious case is (a) with N_mF_2 (density of F2 peak) measured by COSMIC being about 0.4×10^{11} el/m^3 larger than the ISR measurement. The H_mF_2 (altitude of F2 peak) is in good agreement with ISR data. And the profile shape between the two measurements generally matches well. Other comparison profiles are not shown here. Figure 5.11 provides the summary of comparisons with ISR. Correlation of the electron density peak at AEI altitude is 0.78 for 28 events selected during disturbed nighttime periods. Generally for all the cases COSMIC RO electron density profiles are in agreement with those observed by ISR. Most differences of measured AEI are within 0.5×10^{11} el/m^3 for the selected 28 cases.

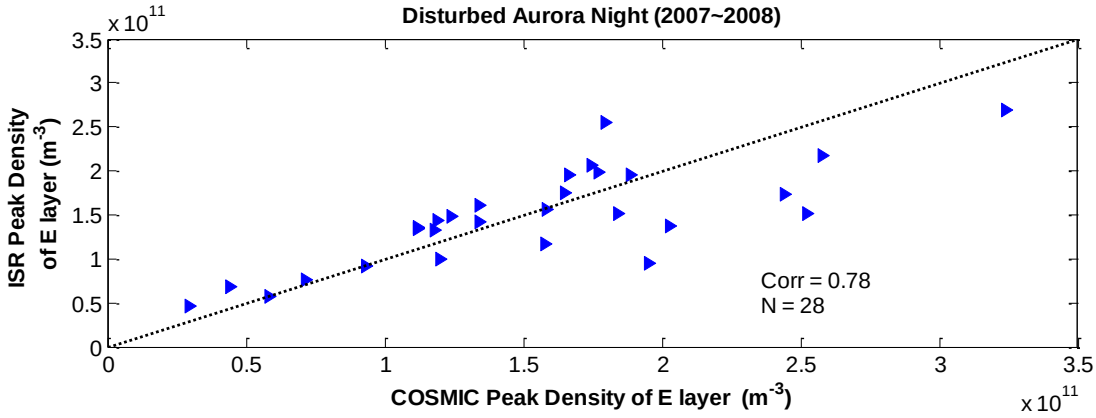

Figure 5.11 Correlation between the COSMIC E region precipitation density and those from ISR during disturbed auroral nighttime periods in 2007 and 2008

For the F region, comparisons do not show large differences for N_mF_2 or H_mF_2 (in the published results by *Lei et al.* [2007], *Hajj et al.* [2000] and *Hajj et al.* [1998]). The agreement of E region precipitation also appears to be good with the limited dataset. For comparison of AEI at 110 km altitude, results show that the altitude of E layer precipitation is generally well captured by COSMIC RO measurements. The differences are the peak values between the two types of measurements, which could result from the presence of non-constant horizontal gradients and spatial mismatch between the two measurements. This deficiency of the Abel inversion is more significant for disturbed ionospheric conditions. Overall agreements are obtained in the selected AEI cases with correlation coefficient of 0.78.

5.3 VALIDATION BY IONOSONDE

Another common tool for ionosphere observation is the ionosonde. *Lei et al.* [2007] conducted comparisons between the retrieved electron density peaks (NmF2) from COSMIC observations and measurements from 31 globally distributed ionosondes. A

dataset of 276 coincident events were identified and validated for June 2006. All RO events were required to be within 2° latitude and 2° longitude of the location of a given ionosonde. The NmF2 electron densities were compared. The correlation result is shown in Figure 5.12 with a correlation coefficient of 0.85. *Hajj et al.* [2000] conducted another comparison of RO profiles with ionosondes. A dataset of 4111 RO occultation events from GPS/MET were selected with tangent points within 1200 km of the ionosonde location and within 1 hour period. A scatter plot of NmF2 correlation is shown in Figure 5.13 (a) and a histogram of the differences in density (NmF2 (GPS/MET)-NmF2 (ionosonde)) is shown in Figure 5.13 (b).

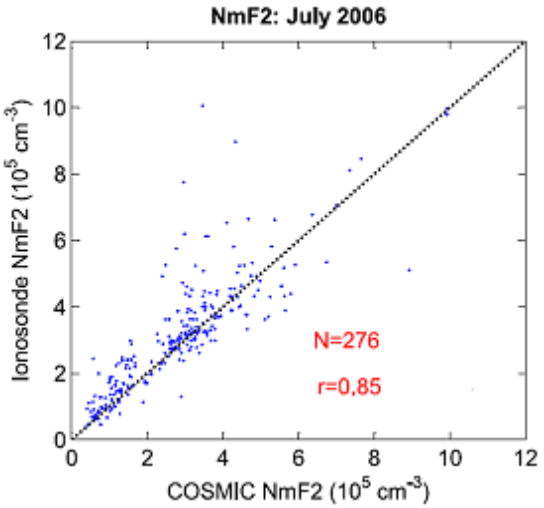

Figure 5.12 Correlation between COSMIC NmF2 and ionosonde measurements for July 1 to 31 2006 [after *Lei et al.*, 2007]

Hajj et al. [2000] also analyzed the measurement differences as a function of local time. Analysis showed that the fractional difference is larger during pre-dawn periods. Since the spherical symmetry assumption is inadequate when the ionosphere is full of irregularities and structures (which can introduce large errors to the electron density retrieval by RO) the large fractional errors of NmF2 at night reflect that ionospheric

horizontal gradients are generally more significant at nightside.

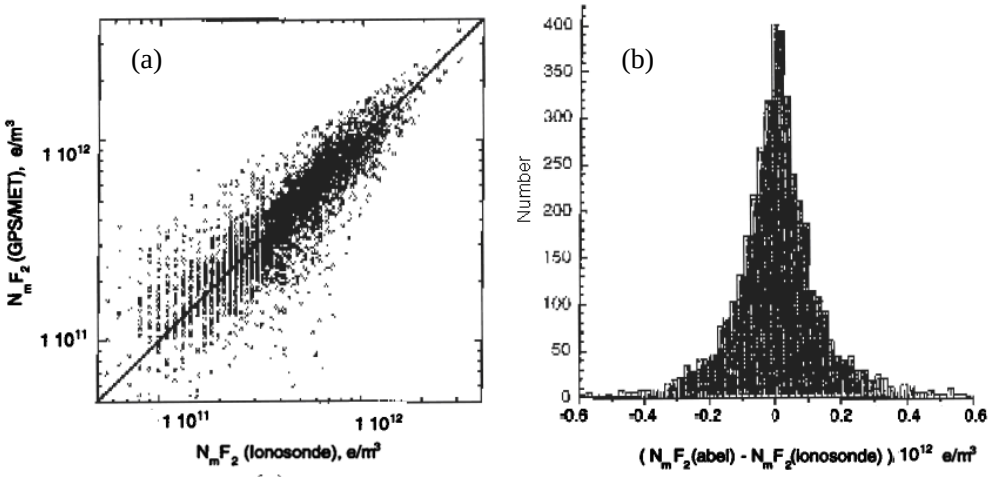

Figure 5.13 (a) Correlation of 4111 coincident events between ionosondes and RO from GPS/MET, and (b) Statistical analysis of the 4111 events [after *Hajj et al.*, 2000]

Stratus [1999a; 1999b] reached a similar conclusion. Beyond using different observation tools there have also been other analyses conducted: for example comparisons between RO profiles that took place in close proximity. Please refer to *Hajj et al.* [2004], *Schreiner et al.* [2007], *Anthes et al.* [2008] and *Kuo et al.* [2004].

5.4 VALIDATION SUMMARY

This chapter provided an overview of RO electron density profile validation. A dataset of disturbed days was selected to validate the RO electron density profiles using ISR observations. The limited datasets demonstrated an agreement between the two types of observations. Under disturbed ionospheric conditions COSMIC RO can capture the altitude of E region precipitation and provide realistic electron density profiles. The presence of non-constant horizontal gradients and spatial and temporal mismatch

between two measurements contribute to any major discrepancies. *Syndergaard et al.* [2006] concluded that the largest error source for GPS RO electron density profile is the strong horizontal gradients; assumptions made in the Abel inversion become less valid with the existence of strong electron gradients in the ionosphere. Incorrect assumptions can result in either positive or negative errors larger than 10^5 el/cm^3 at the bottom of the retrieved profiles in certain cases [*COSMIC*, 2009]. A method to overcome the horizontal inhomogeneity of the ionosphere is to include external information during the inversion process [*Kuo et al.*, 2004]. There is also ongoing research to improve the retrieval algorithm [*Hajj and Romans*, 1998; *Schreiner et al.*, 1999]. For future work more extensive validation needs to be carried out for "disturbed" electron density profiles.

CHAPTER 6

CHARACTERISTICS OF RADIO OCCULTATION OBSERVATIONS UNDER DISTURBED IONOSPHERIC CONDITIONS

6.1 METHODOLOGY

Results of Chapter 5 demonstrated that electron density profiles derived from radio occultation measurements can realistically represent ionospheric variations under disturbed conditions. In this chapter RO observations under disturbed ionospheric condition will be analyzed. Information about the ionospheric disturbances is then inferred. Firstly the characteristic trends due to large scale ionospheric structures is filtered out [*Wu et al.*, 2006; *Wu et al.*, 2005; *Wu et al.*, 2002; *Tsybulya and Jakowski* 2005; *Hocke et al.*, 2001; *Straus et al* ., 2003]. The signal to noise ratio, excess phase observation, line-of-sight (GPS-LEO) TEC, and electron densities are used to infer variation in the RO observations due to the effects of ionospheric irregularities. In order to remove large-scale structures and reveal details of smaller scale ionospheric irregularities a twenty points cubic polynomial approximation filter is chosen [*Tsybulya and Jakowski*, 2005]. One example is shown in Figure 6.1. The same RO event from Figure 5.8 is used. The approximation is based on selecting a polynomial function of degree three and finds the coefficients of the polynomial that fits the data of every twenty points of the observations best in a least square sense. The polynomial approximation usually results in a spline that can fit the trend of the observation profiles. After subtracting the approximation result the detrended smaller scale information of the profiles can be obtained.

6.1.1 DETRENDING METHOD DESCRIPTION

Studies of the ionospheric irregularities are conducted by detrending the electron density profiles. For 1 Hz electron density measurements a twenty-point cubic polynomial approximation is applied to the COSMIC observations in order to remove the large scale structures (trend) of the electron density [*Tsybulya and Jakowski*, 2005]. The polynomial approximation to electron density observations is conducted along with the RO TPD (tangent point displacement) estimation. The approximation result by polynomial is subtracted from the original observation profile. The remaining differences are then mapped to altitude. One example of polynomial detrending is shown in Figure 6.1. Some data products do not include altitude information. In such cases the mapping between time and tangent height is conducted by using the satellite's ephemeris, assuming straight line propagation in the ionosphere and upper stratosphere.

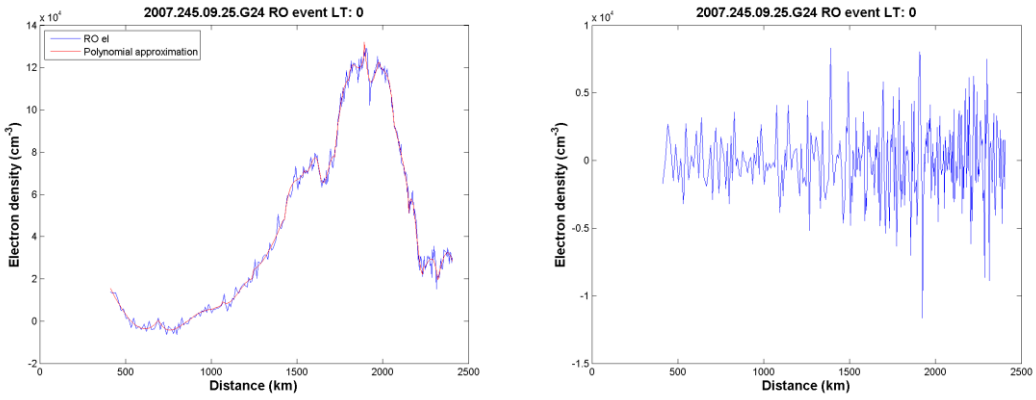

Figure 6.1 Electron density along tangent points and polynomial approximation (left), and differences between original RO electron density and polynomial approximation (right)

6.1.2 GENERAL CHARACTERISTICS OF AURORAL EVENTS

6.1.2.1 LOW FREQUENCY OBSERVATIONS

The local geomagnetic field on September 1 2007 indicated ionospherically disturbed conditions in Alaska during 0800 to 1200 UT (refer to Figure 5.7) [*GIMA*, 2009]. One RO event occurred at 0958 UT close to the GIMA magnetometer network (refer to Figure 5.9). The COSMIC data products recorded in “ionPhs” and “ionPrf” files are plotted and detrended for the selected RO event. Figure 6.2 from top to bottom shows the GPS TEC measurement, C/A code SNR, L2 SNR, and electron density measurements.

The SNR plots (Figure 6.2 (b) and (c)) and electron density profile (Figure 6.2(d)) show an obvious enhancement at 110 km altitude (E region). Measurements in Figure 6.2 start from a tangent height around 600 km. All the detrended plots show obvious fluctuations at 110 km altitude corresponding to the AEI feature during auroral nighttime. The decrease in C/A and L2 SNR indicates that AEI structures at 110 km altitude are introducing amplitude scintillation for the LEO-GPS link. TEC and density measurements both show an enhancement of ionospheric delay and fluctuation in the E region. In this example SNR, raw observations, and retrieved electron density exhibit good consistency with the expected altitude (110 km) of ionospheric disturbances during AEI.

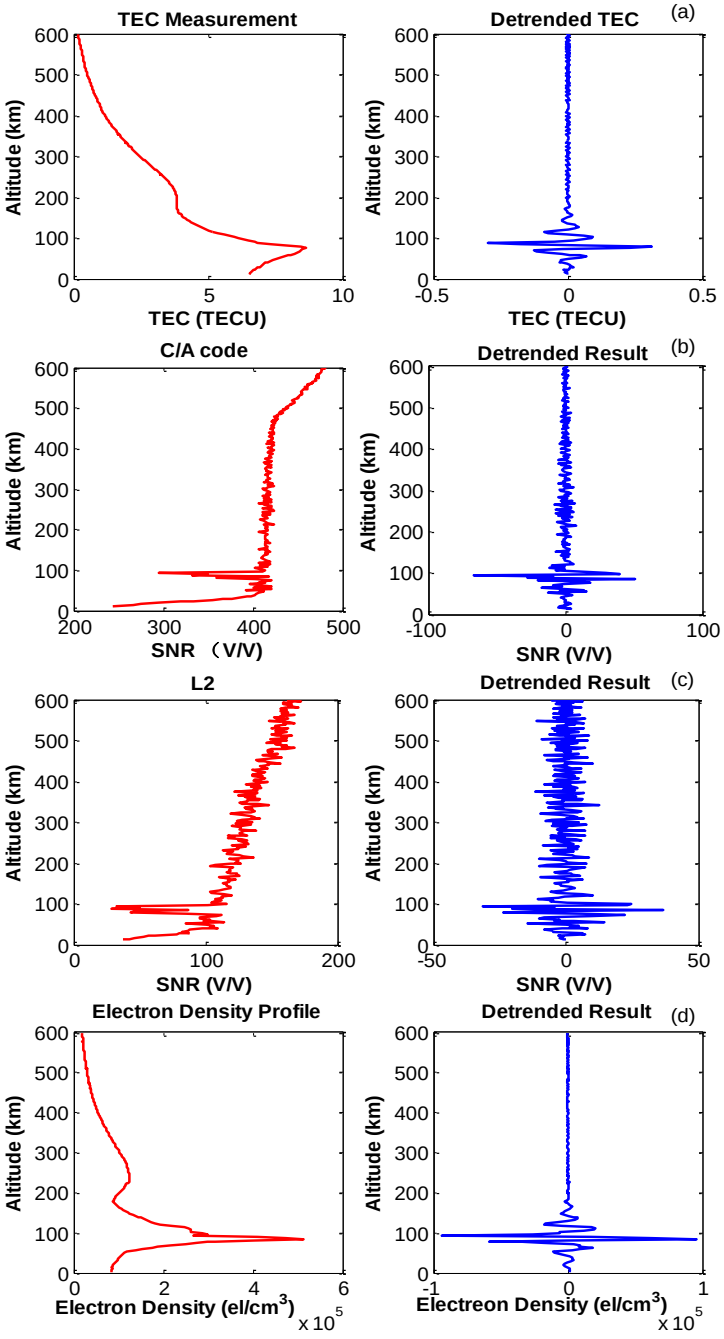

Figure 6.2 COSMIC level 1 and level 2 products for 1 Hz RO observations on September 1 2007 at 0958 UT (left) and the perturbation extracted from polynomial approximation detrending (right) for (a) 1 Hz TEC measurements from L1 and L2 phase observation, (b) C/A code SNR, (c) L2 SNR, and (d) electron density profile

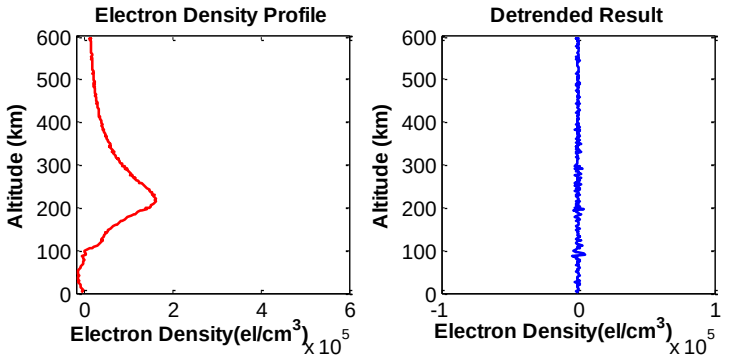

Figure 6.3 COSMIC electron density products for RO on 24 August 2007

Figure 6.3 shows RO observations on 24 August 2007. This is another event that occurred close to an Alaskan magnetometer at local midnight. However August 24 was a magnetically quiet day with K indices (magnetic fluctuations) at College Alaska being 0 for the period studied. The plot axes are the same as in Figure 6.2 (d). It is observed that the F region peak density (HmF2) for both the "quiet" profile and the "disturbed" profile occur near 250 km altitude with a maximum density magnitude of 10^5 el/cm^3. It can be observed in Figure 6.3 that for altitudes lower than 100 km there are some negative electron density values. In reality it is impossible to have negative electron density values. The false density values arise from the increasing neutral component for troposphere altitude range. Usually below 50 km altitude the bending contributions from air/water are generally larger compared to electron density effects [*Wu et al.*, 2005]. Another factor to contribute the negative value of electron density is the spherical symmetry assumption made for the Abel inversion [*Lei et al.*, 2007]. However the altitude range being considered for ionosphere effects is usually above 90 km altitude. The negative values of electron density for lower altitude range can be neglected for the study of this thesis.

The major difference between the "disturbed" (Figure 6.2) and "quiet" (Figure 6.3) profiles is the sudden enhancement appearing at E region altitudes (approximately 110

km) for the disturbed profiles (which corresponds to AEI structure). The NmF2 in Figure 6.2 is 1.2×10^5 el/cm^3 while the NmF2 in Figure 6.3 is a bit larger at 1.8×10^5 el/cm^3. Considering that the quiet case shows the nominal electron density profile at midnight, the enhancement associated with AEI is noted to start from 150 km altitude downward in Figure 6.2 (d).

6.1.2.2 HIGH FREQUENCY OBSERVATIONS

As described previously 50 Hz RO measurements are only available from approximately 150 km altitude due to satellite data payload concerns. Analysis of 50 Hz data is shown in Figure 6.4.

Figure 6.4 shows 50 Hz SNR and L1 and L2 phase measurements of the same COSMIC event on 1 September 2007. Starting from a tangent height at around 130 km, 50 Hz data scans through the E region at a descending rate around 2.2 km/s. Here the SNR can vary substantially from occultation to occultation [*Wu et al.*, 2005]. In this example the SNR is larger than 5000 and decreases below 30 km altitude because of defocusing effects in the neutral atmosphere. The SNR exhibits abrupt variations at tangent heights around 100 km indicating the existence of sharp ionospheric structures in that region.

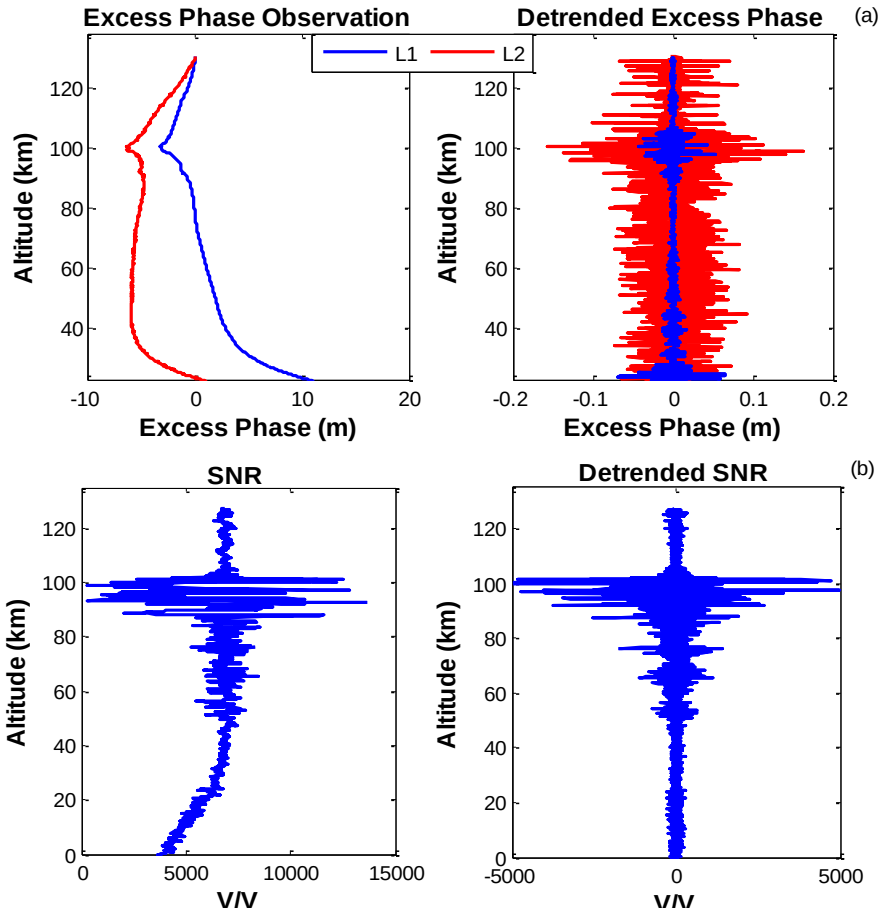

Figure 6.4 50 Hz RO observation analysis for September 1 2007 at 0958 UT (left), and the perturbation extracted from detrending (right): (a) Excess phase of L1 and L2 (b) C/A code SNR

Both the excess phase profile and detrended excess phase show the existence of local ionospheric structures at altitudes near 110 km that introduce additional decrease in excess phase measurement (and fluctuations for detrended excess phase). The detrended excess phase shows bigger fluctuations for the L2 signal versus L1, which probably occurs because of the generally low L2 signal SNR. The L2 SNR is not shown because of its low values and the applied semi-codeless tracking technique that can introduce more noise into the signal.

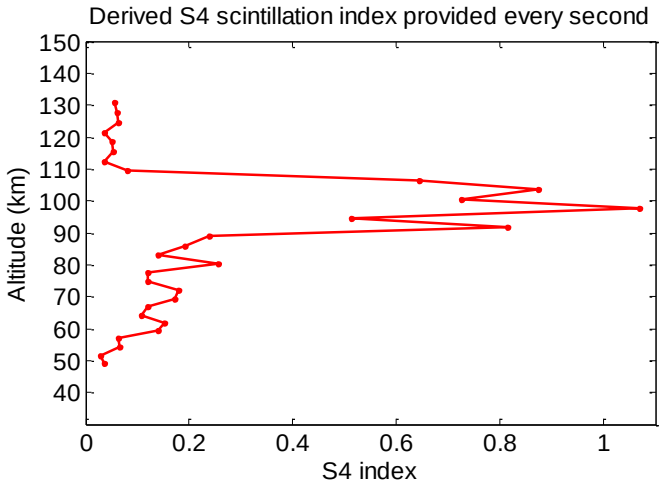

Figure 6.5 S4 index provided by CDAAC (COSMIC)

Figure 6.5 shows the S4 index plot for the September 2007 event. The S4 index is derived from the signal to noise intensity fluctuations in the raw 50 Hz L1 amplitude measurements [*Syndergaard*, 2006]. It is used to show the amplitude scintillation of RO signal received by LEO. In Figure 6.5 the scintillation is observed to be significant at tangent heights in the E region due to the electron density irregularities from AEI, which correspond to the same altitudes determined in previous analyses. Both the 1 Hz and 50 Hz observations exhibit great agreement in identifying the altitude of AEI occurrence. For scintillation studies of the high latitude region, the auroral irregularity altitude and the intensity of signal fluctuation, as well as correlation distance, are necessary in order to build three-dimensional phase screens for ionosphere simulations.

6.1.3 DATA PROCESSING

The auroral E-ionization region is associated with large variations in electron density at specific scale sizes. To extract small-scale structures of aurora the electron density

profile is detrended. The COSMIC level 1 product "ionPhs" is used to derive electron density profiles by using University of Calgary in-house software. SNR, L1 and L2 raw observations are used from data recorded in "atmPhs" files. Disturbed periods are selected based on a local magnetometer dataset or CANGIM scintillation observations described in Section 5.1. The intensity and boundary of the aurora can be inferred from the magnetometer observations. The CANGIM dataset is used to indicate the presence of ionospheric scintillation (detected at ground locations). RO events are selected during disturbed periods and within active ionosphere regions. Detrending and power spectral density (PSD) analyses are applied to the "disturbed" RO measurements to determine information about ionospheric instabilities in the high latitude region. A flow chart of the whole process is shown in Figure 6.6.

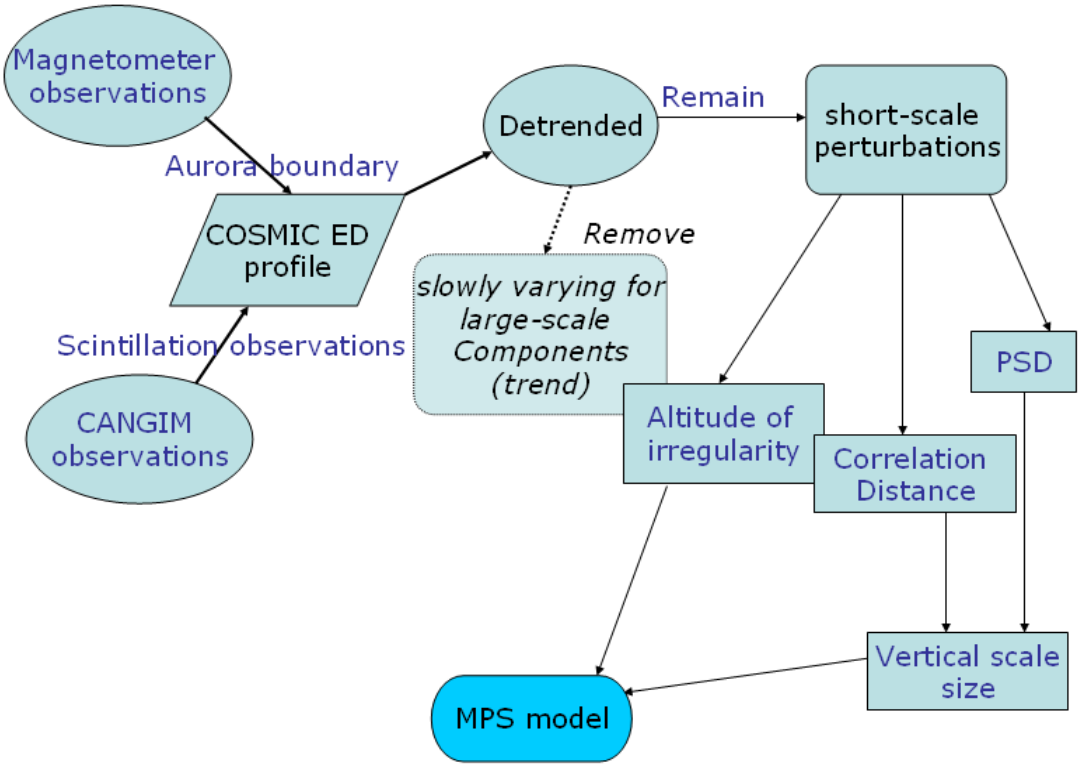

Figure 6.6 Flow chart of data processing

In this thesis study the following processing and analyses are conducted by the candidate.

- The “disturbed” electron density profiles from the radio occultation observations are selected based on CANGIM and magnetometer network observations for the Canadian region.

- Electron density profiles are detrended in order to remove the large-scale components. Then the remaining small-scale perturbations are input for further PSD analyses.

- Altitude, scale size and intensity information of ionospheric irregularities is derived. In future such information can be used for multi-phase screen scintillation simulation modeling. However the modeling part is beyond the scope of this thesis.

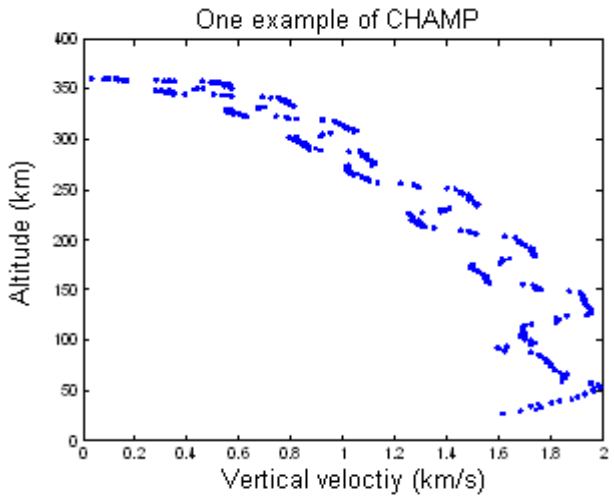

Figure 6.7 Vertical velocity for one RO observation with 1 Hz data rate in the ionosphere at different altitudes

For PSD analysis, because radio occultation observations are not evenly sampled in the spatial domain (shown in Figure 6.7), an alternative technique to the Fast Fourier Transform named “Lomb method” is chosen. For the “Lomb method” [*Lomb*, 1976] the power spectral density is derived from a least squares adjustment (fit) to each discrete wave number.

6.1.4 AURORAL BOUNDARY PREDICTION

The aurora oval location is predicted using software developed at University of Calgary. Predictions are computed using ground magnetometer data at different latitudes, for example the CARISMA magnetometer line (from TALO station in the north to PINA station in the south) [*CSSDP*, 2009]. Satellite-based observations for auroral energy and GUVI (Global Ultraviolet imager) are also used as complementary observations.

The fundamental method is described as follows. The magnetometers measure the north-south component of the magnetic field (X), the east-west component (Y) and the vertical component (Z). The three components are continuously measured. Once the magnetic field becomes disturbed the east-west auroral electrojet current grows. The dominant westward electrojet causes a decrease in the X component. The Z component then gives the location of the boundary of the east-west currents; peaks in the Z component are used to define the edges of the electrojet, which defines the auroral boundary.

Evolution of the electrojet width and position for a certain longitude can be obtained by using magnetometer observations at different latitudes along a meridian to profile the auroral electrojet. The real-time auroral oval mapping is generated at

http://portal.cssdp.ca. Figure 6.8 shows the auroral boundary defined by the software developed at University of Calgary.

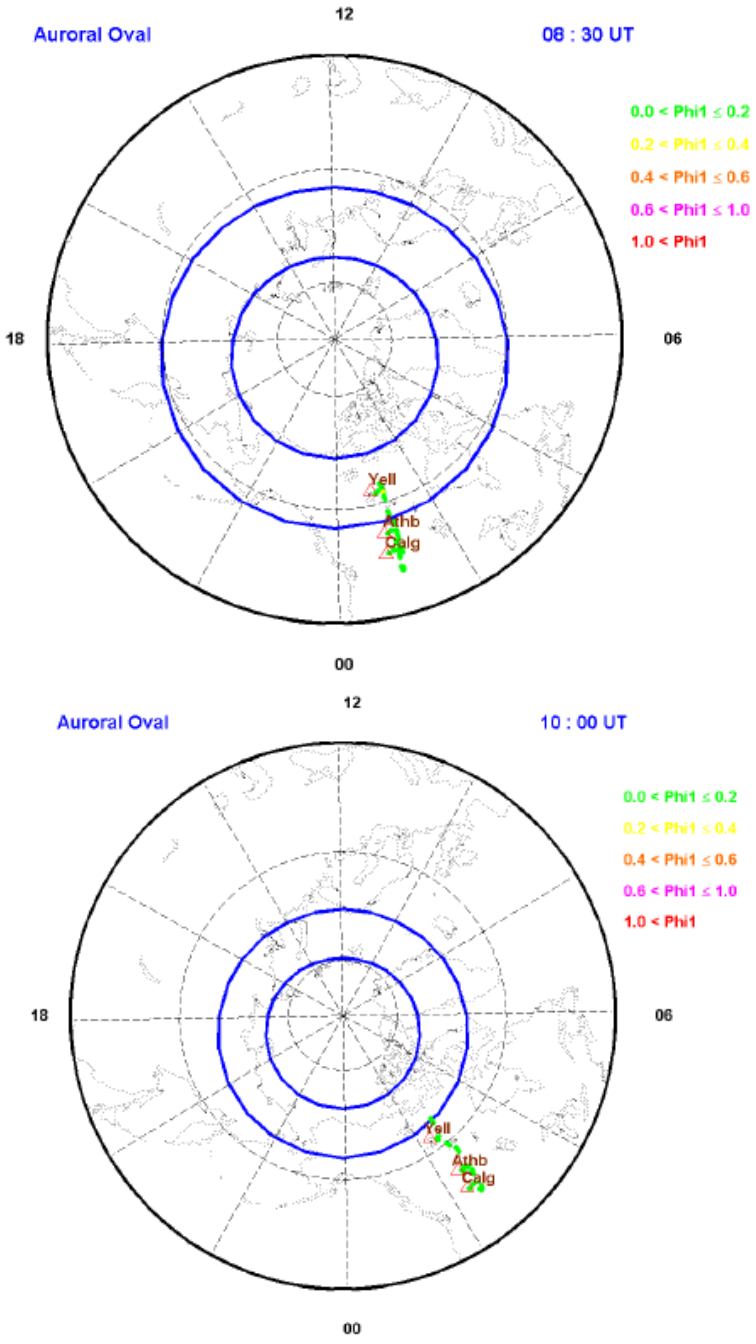

Figure 6.8 Auroral boundary (blue) at 0830 and 1000 UT October 3 2007. The three triangles show locations of CANGIM scintillation receivers.

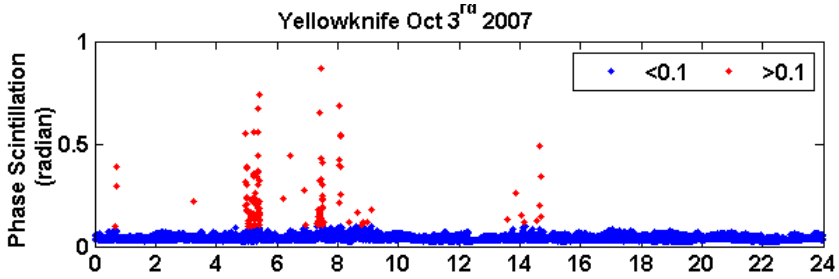

Figure 6.9 Phase scintillation observations at CANGIM site Yellowknife, October 3 2007

Phase scintillation observations at Yellowknife are shown in Figure 6.9 and used to validate the presence of ionospheric scintillations. The red points indicate values larger than 0.1 rad. At 0830 UT some severe scintillation is observed. In Figure 6.8 the location of Yellowknife is in the middle of the auroral oval. At 1000 UT there are no large phase scintillation values observed in Figure 6.9. Accordingly in Figure 6.8 the auroral oval is at higher latitudes (poleward of Yellowknife). This is a simple example to exhibit the correlation between auroral phenomenon and phase scintillation observed at ground sites. In the analyses conducted here both magnetometer measurements and CANGIM observations are used to identify disturbed ionospheric conditions. Electron density profiles and other RO measurements are then selected according to the ground observations to demonstrate the in situ ionospheric characteristics during high-latitude ionospherically disturbed conditions.

6.1.5 EVENT SELECTION

As mentioned previously RO events are selected for ionospherically disturbed conditions with tangent points located within auroral boundaries during periods with

ground scintillation effects observed by CANGIM. Events are specified for two types of ionospheric phenomena: aurora during substorm periods and SED for major magnetic storms.

6.2 HIGH LATITUDE RADIO OCCULTATION EVENTS UNDER IONOSPHERICALLY DISTURBED CONDITIONS

6.2.1 EVENT ANALYSES

In this section high-latitude electron density profiles retrieved from RO observations are studied; data are selected based on ground observations (phase scintillations and magnetometer data) under disturbed ionospheric conditions. A substorm on October 1 2007 and the severe storm period on October 29, 2003 are chosen. Corresponding RO events are selected to investigate the irregularity intensity and distribution during high latitude ionospherically disturbed times.

6.2.1.1 AURORAL EVENTS

Two events are selected for auroral substorm periods, as detected by magnetometer observations, in which RO observations are available at auroral oval latitudes. The tangent points of RO profiles are shown as blue lines in Figure 6.10. CANGIM scintillation ionospheric pierce points (IPP) are also shown in green (moderate phase scintillation in the range 0.2-0.5 rad) and red (strong phase scintillation larger than 0.5 rad) [*Yu*, 2007].

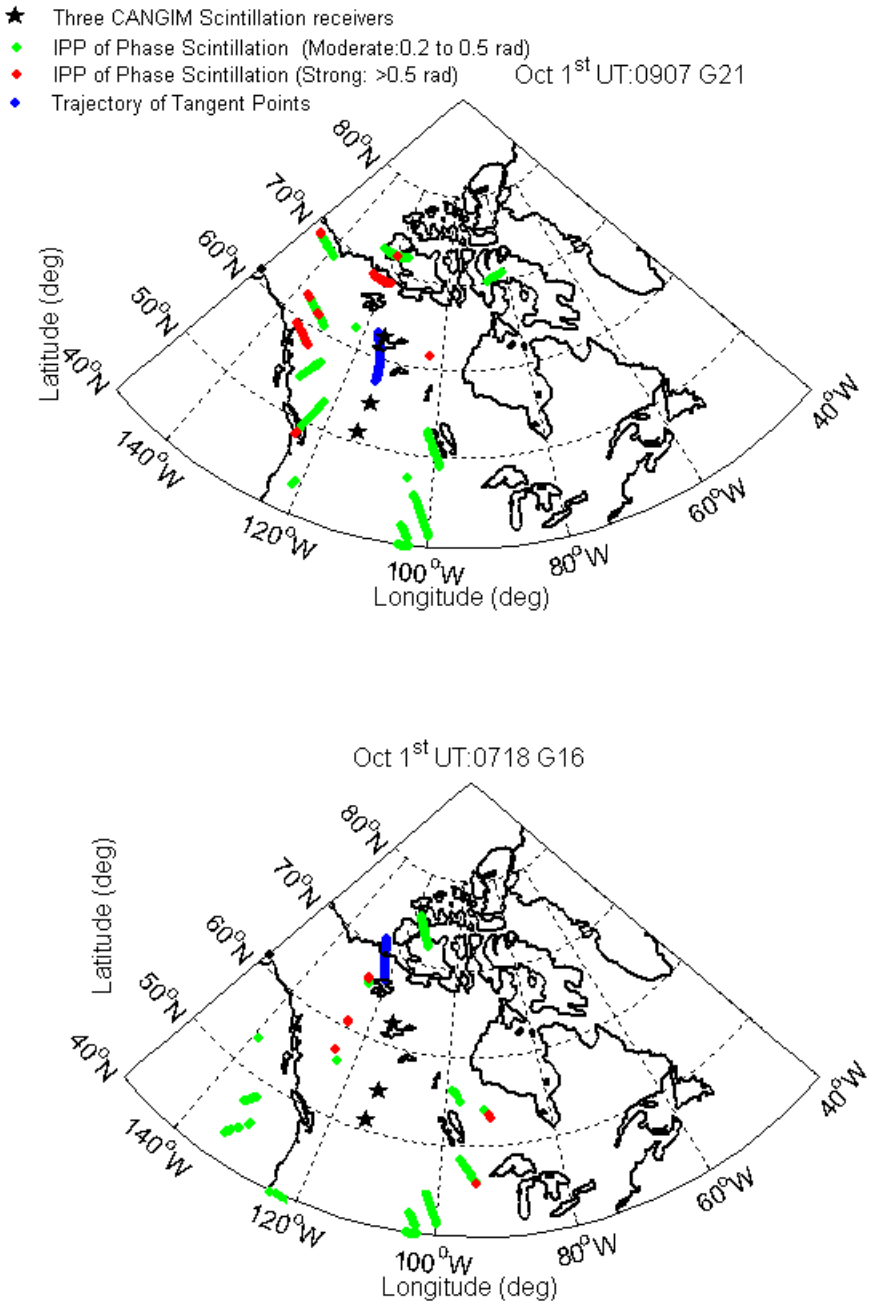

Figure 6.10 Two cases of COSMIC RO events with tangent points inside the auroral oval during disturbed nighttime conditions, with trajectory of tangent points (blue) and CANGIM scintillation observation larger than 0.5 rad (red) and between 0.2 rad and 0.5 rad (green)

RO tangent points are within the area of observed scintillation. Figure 6.11 shows a time series of phase scintillation observed at CANGIM site Yellowknife. RO profiles are available during the two periods of strong scintillation. It is expected that ionospheric irregularities exist at these times.

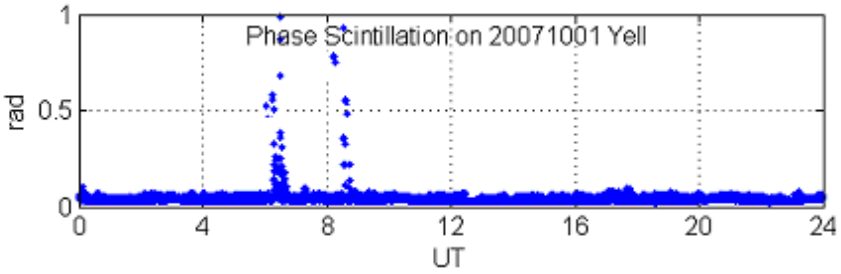

Figure 6.11 Yellowknife scintillation observations on October 1 2007

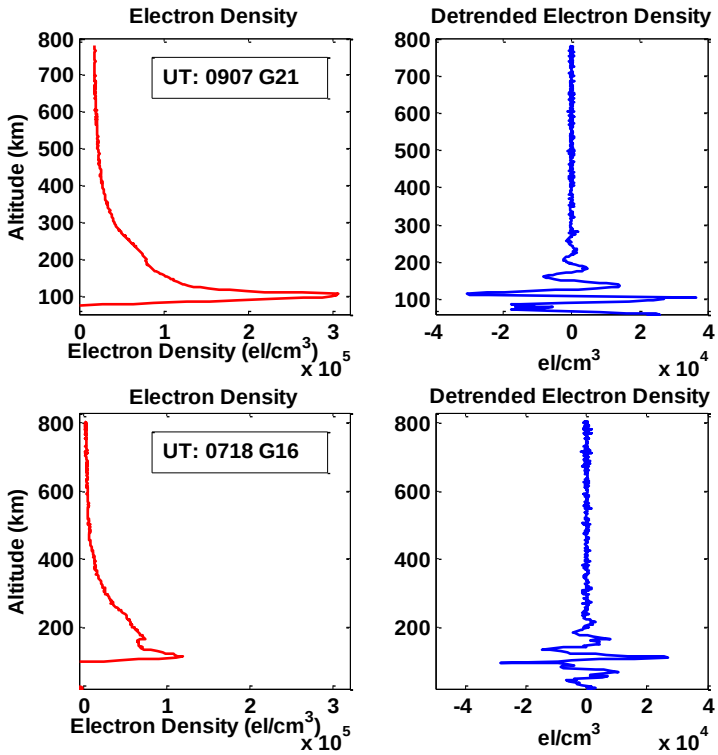

Figure 6.12 Electron density and detrended results for two auroral RO events on October 1 2007

Figure 6.12 shows electron density profiles for the two auroral events. An AEI feature

is observed around 110 km altitude. Recall Figure 6.3 is an electron density profile at local midnight during an ionospherically quiet period for comparison purposes. No AEI feature is observed in the quiet profile. And the density peak for the quiet data is at altitudes above 200 km in the F region. Figure 6.12 also shows the detrended electron density profiles for smaller scale sizes in which ionospheric disturbances can be identified. A twenty-point cubic polynomial approximation is applied to the full COSMIC electron density profile in order to remove the large-scale structures (low frequency trend) and show detailed information about small-scale ionospheric disturbances. The remaining high frequency components are then mapped to altitude.

After the density profiles are detrended the results for the first event (top plot of Figure 6.12) show that the electron density can have fluctuations of 3×10^4 el/cm^3 for vertical scale sizes of 10 km. For the two auroral events it can be observed that the E-region enhancements and structures developing from energetic electron precipitation are dominant while the F-region variations are only a few percent of the background values. Large phase scintillation values observed at the Yellowknife CANGIM station are consistent with E-region irregularities developing from energetic electron precipitation.

Figure 6.13 shows the 50 Hz GPS signal SNR observations. The E-region irregularity in electron density is observed near 110 km altitude, corresponding to the SNR fluctuations at 110 km. The corresponding ground scintillation is observed by the nearby Yellowknife receiver, which demonstrates the effects of auroral irregularities of AEI on GPS signals.

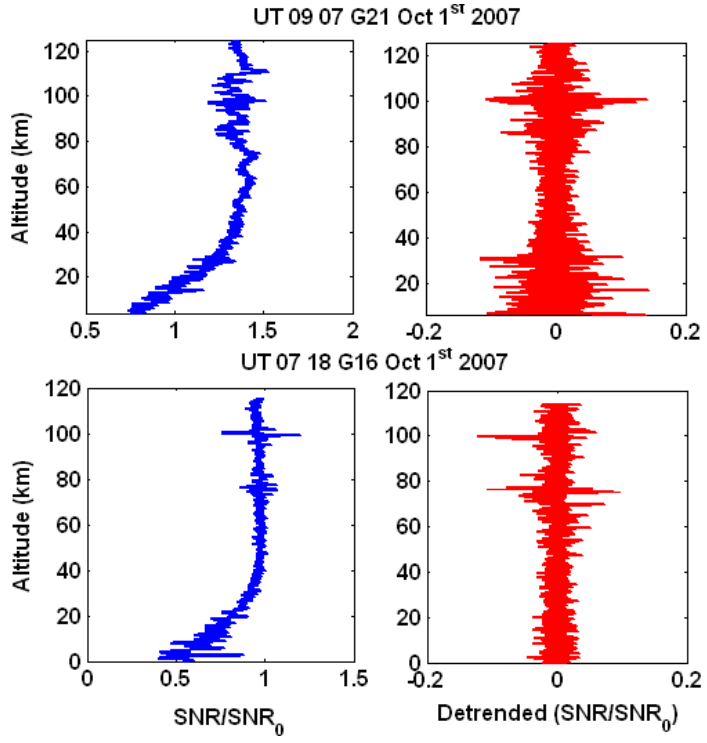

Figure 6.13 Detrended 50 Hz SNR observations

Both Figures 6.12 and 6.13 show the fluctuation of COSMIC observations near altitudes of approximately 110 km corresponding to the altitude of AEI. Figure 6.13 shows the phase variation, which is the phase scintillation introduced to the GPS signal along the LEO-GPS ray. The detrended plot in Figure 6.13 is the variation of SNR which demonstrates the presence of amplitude scintillation along the LEO-GPS ray. Both results show that the AEI near 110 km altitude causes phase and amplitude variations on the GPS signal received by the LEO. Ground scintillation observations are larger when the ray passes through the ionosphere region of AEI.

Power spectral analysis is conducted for the RO electron density profiles on October 1 2007 and the quiet event (Figure 6.3) for comparison purposes. The Lombscargle method instead of the ordinary Fourier transform is chosen since RO measurements are unevenly spaced vertically. Figure 6.14 shows the PSD analysis with X axis as the

wave number. For each event the top plot is the power spectral analysis with wave number less than 0.05 km^{-1}. The electron density profile for the quiet day (blue line) is dominated by one major peak at 0.0025 km^{-1} which corresponds to a wavelength of approximately several hundred kilometers.

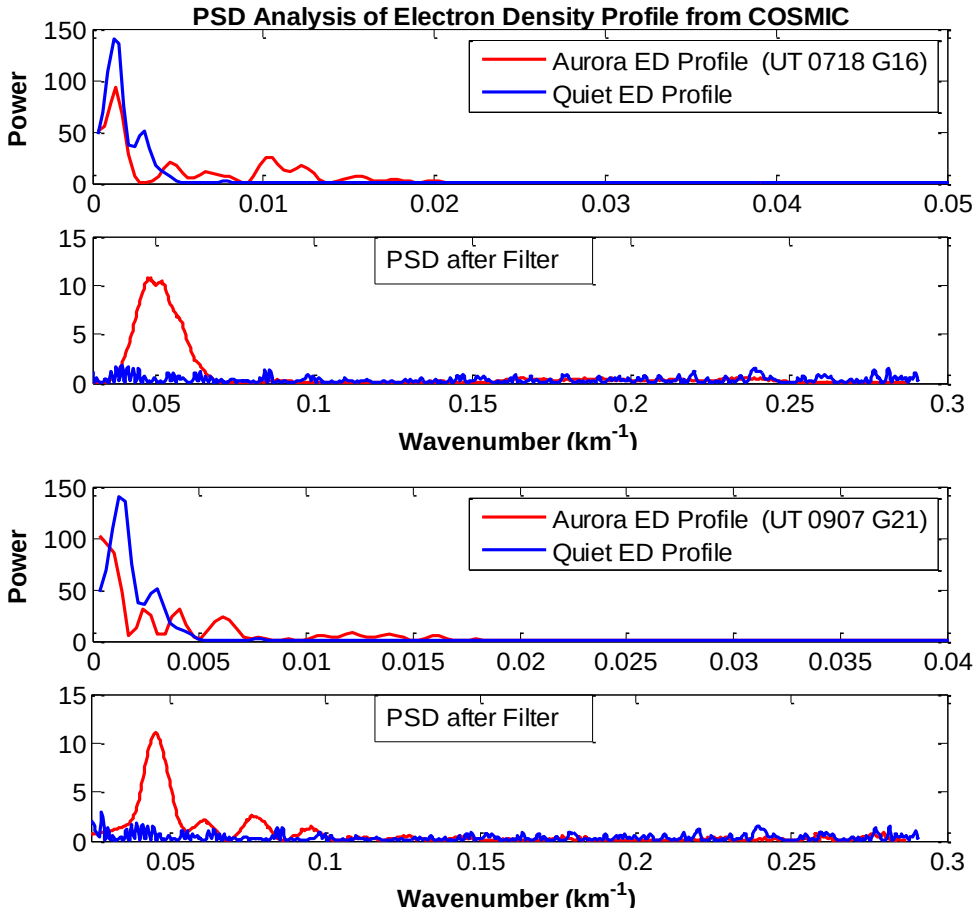

Figure 6.14 Power spectral analyses of electron density profiles for the two selected auroral events

The blue line is the quiet event (from Figure 6.3) for comparison purposes. From analysis of the two events it can be expected that structures with scale sizes of 50-100 km have peak power in the disturbed profile. The bottom plot of each event is the PSD for small wavelengths. Only structures with scale sizes less than 30 km remain.

Two obvious peaks around 0.05 km^{-1} wave number (corresponding to a wavelength of 20 km) are observed for the "auroral" electron density profiles. In reality the PSD analysis of ionospheric structures is limited by the vertical resolution of RO measurements. There is no significant difference for wavelengths less than 10 km between "auroral" and quiet electron density profiles. The conspicuous peak at 20 km wavelength (red line) may arise from the enhanced E region at 110 km with vertical scale size of tens of kilometers.

An autocorrelation function is calculated for the two "auroral" electron density profiles and the quiet profile. In Figure 6.15 the correlation distances for the two auroral events are much smaller compared with the quiet profile, which mainly comes from the structure of electron precipitation in the E region. The sharp and thin layer with sudden enhancement near 110 km also comprises small scale electron density irregularities. Signals transmitted by satellite navigation systems will experience strong scintillation effects due to the instabilities in this thin layer. The autocorrelation function also reveals that the thickness of AEI is approximately tens of kilometers, while the correlation coefficient drops to 0.5 at around 20 km wavelength.

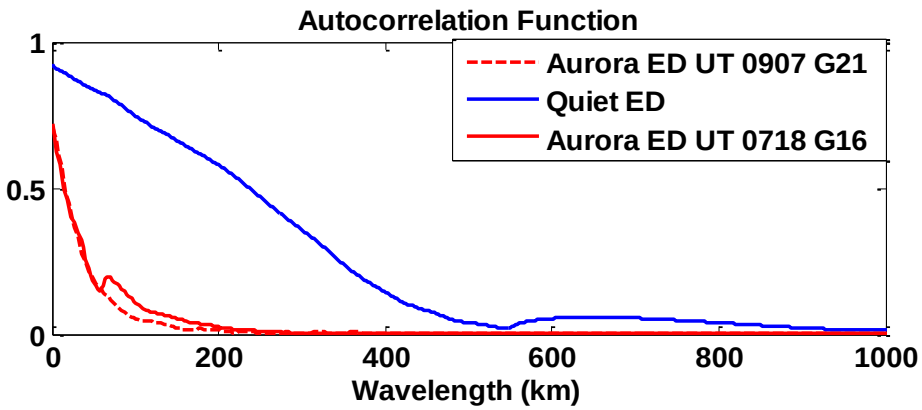

Figure 6.15 Autocorrelation function for the two "auroral" electron density profiles and the quiet profile

Wavelet powerspectrum analysis is also applied to study the three electron density profiles in Figures 6.16 and 6.17. Wavelets can be solved with a flexible resolution for the spectrum in both frequency and time domains. For RO observations the spectrum is mapped into altitude and wave number domain. Here the popular "Morlet" wavelet is chosen as the mother wavelets. A filled contour plot is used to visualize the powerspectrum [*Trauth*, 2007].

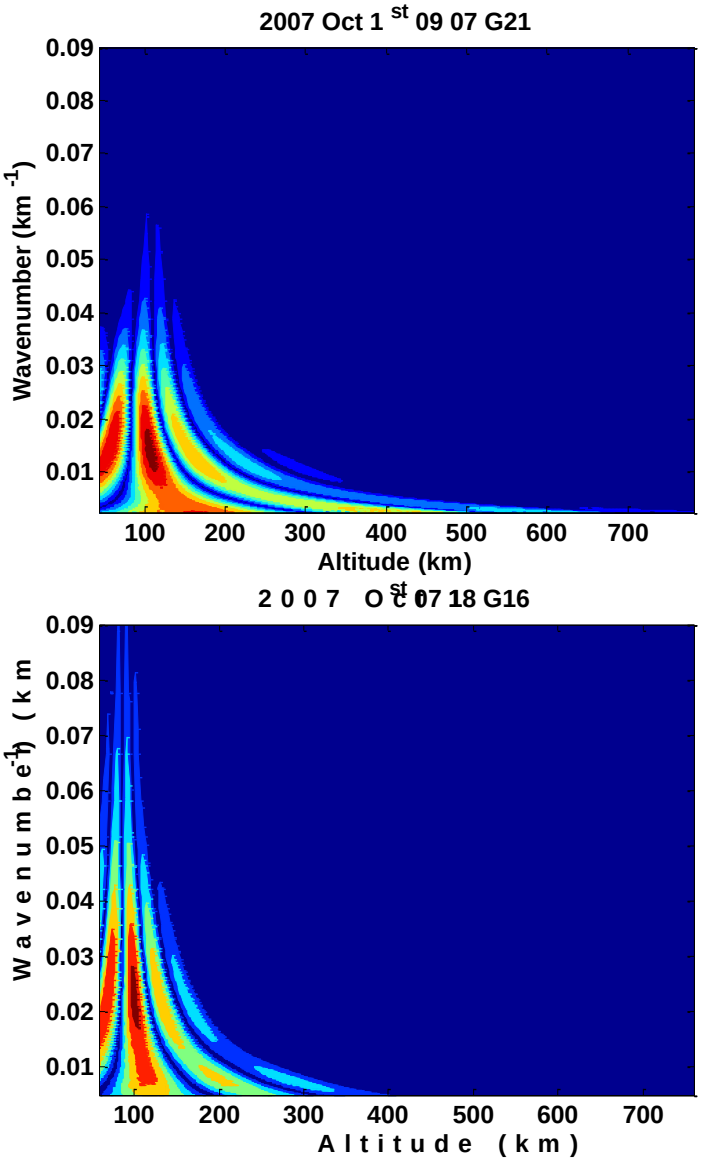

Figure 6.16 Wavelet power spectrum analysis for the electron density profiles in auroral region

The reason why wavelet method has been chosen to analyze electron density profiles is the benefit of providing power distribution in both the time and frequency domains. For the dataset studied here the power can be related to both the wavelength range and altitude. And it is preferable to know the altitude for different scale sizes; this information is not provided by normal Fast Fourier transform. Another advantage of wavelet analysis compared with Fast Fourier transform is that it is advantageous to resolve power distribution for functions which have discontinuities and are non-periodic [*Trauth*, 2007]; this is directly applicable to the COSMIC electron density profiles.

Power for the two "auroral' event electron density profiles is mainly concentrated from 100 km to 150 km altitude which reflects the E-region fluctuations. There is high power at 110 km for both of the power spectrums. For the event at 0907 UT the corresponding dominant wavelength is 50-100 km. For the 0718 UT event one wavelength is dominant in the range 30-50 km. Both of the high-power regions are associated with the sudden enhancement of electron precipitation in the E region during disturbed auroral periods. Wavelets can be used to determine the altitudes of such structures. Dominant effects are observed at 110 km altitude. In contrast for the wavelet power spectrum of the quiet event in Figure 6.17, the power is mainly concentrated in wavelengths larger than 200 km.

It is noted that the scale sizes determined in both the PSD analysis and the autocorrelation calculations do not necessarily represent the real scale sizes of ionospheric irregularities (which may be smaller in scale and below the resolution threshold for the observation sample rate). However the observed electron density variations (obtained by detrending or by wavelet analyses) are primarily associated with plasma irregularities. In comparison with the power spectrum (Figure 6.17) of

the “quiet” electron density profile (Figure 6.3), more power can be found within smaller wavelength ranges for disturbed events which is consistent with the existence of small instabilities during high levels of ionospheric activity. The wavelet analysis of COSMIC RO electron density shows good correlation of irregularities for altitude ranges determined from the detrending analysis.

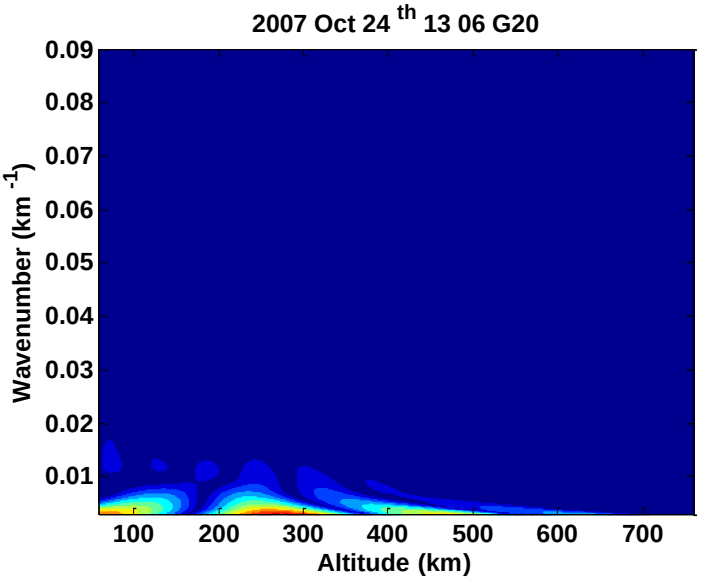

Figure 6.17 Wavelet power spectrum analysis for the quiet electron density profile 1306 UT (G20) on October 24 (the corresponding density profile is shown in Figure 6.3)

6.2.1.2 EXTREME STORM EVENTS

Amplitude scintillation is not common for high latitudes. However, during an extreme storm on October 29 2003 amplitude scintillation was recorded in CANGIM observations. Two RO events from CHAMP were identified with ground amplitude scintillation observed by CANGIM (Figure 6.18). The S4 index and phase scintillation index at Yellowknife is shown in Figure 6.19. Phase scintillation reached high values of 1 rad which is considered to be severe scintillation.

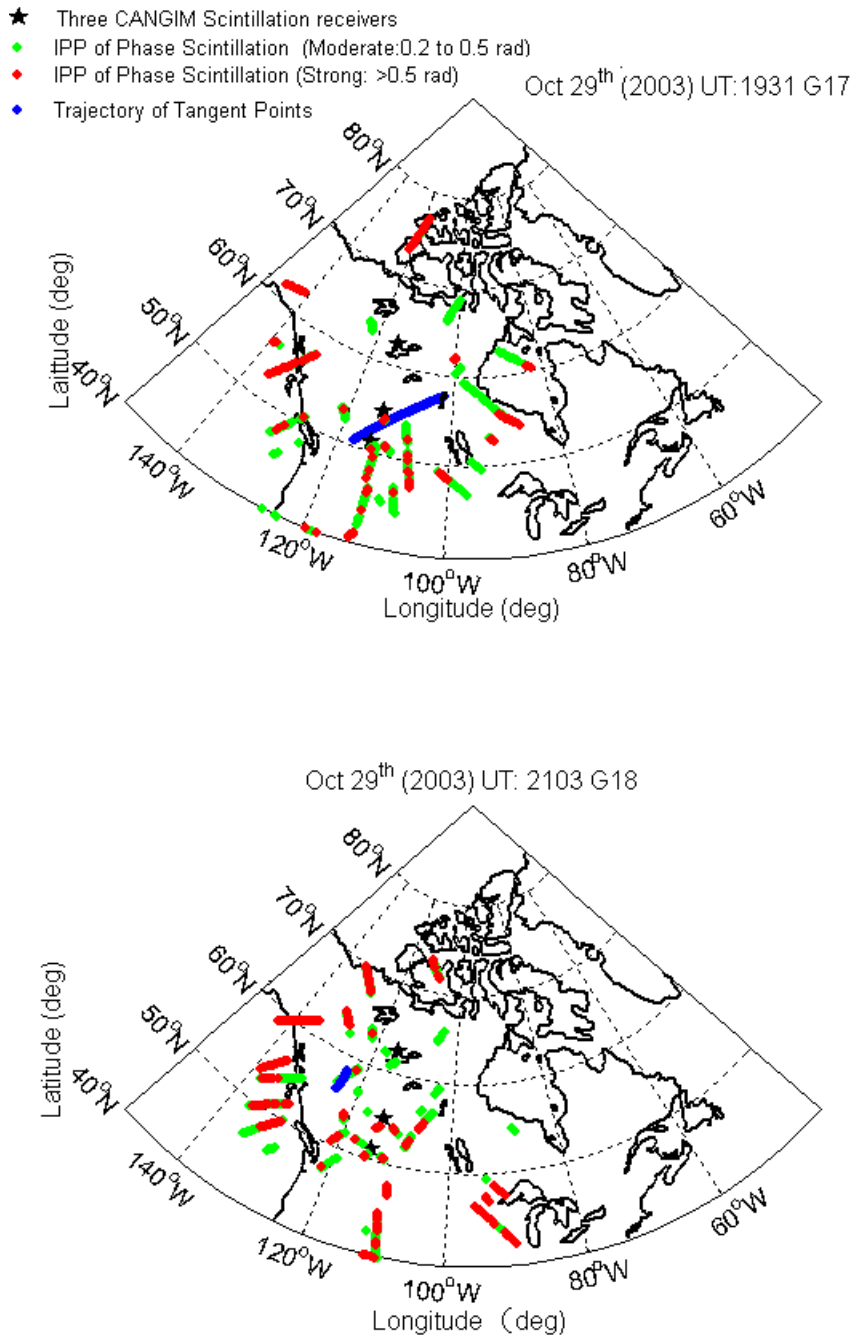

Figure 6.18 Two COSMIC RO events during the severe storm on October 29 2003 and phase scintillations observed by CANGIM with threshold of 0.5 rad (red), and between 0.2 rad and 0.5 rad (green)

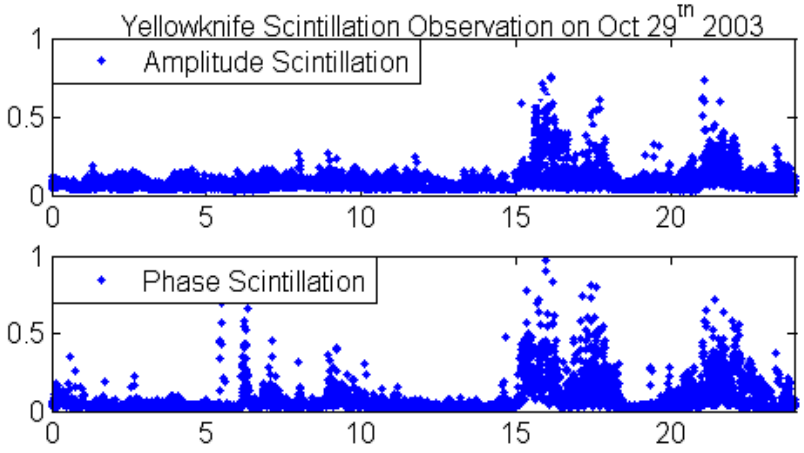

Figure 6.19 Yellowknife scintillation observations on October 29 2003

Electron density profiles for the two CHAMP RO events are shown in Figure 6.20. From the raw density and detrended results it is observed that both profiles show large E region enhancements and fluctuations extending to the F region. The electron densities are generally larger than those observed in other events (in previous sections). The events shown in Figure 6.20 are for the daytime sector (with solar radiation creating more electron density). Also, on October 29 2003 (during the storm period), the ionosphere was severely disturbed with the presence of SED causing large gradients and density enhancements.

Both events occurred at the time and location consistent with amplitude scintillation observed at ground CANGIM receivers. Amplitude scintillation at L-band is not as common for high latitude regions as phase scintillation. However, during severe storm periods the entire ionosphere is disturbed with small-scale structures distributed over a range of altitudes and irregularities at a wide range of scale sizes. Radiowaves, after propagating through the ionosphere, will experience multiple effects from the irregularities at different altitudes, resulting in both phase variations and SNR variations.

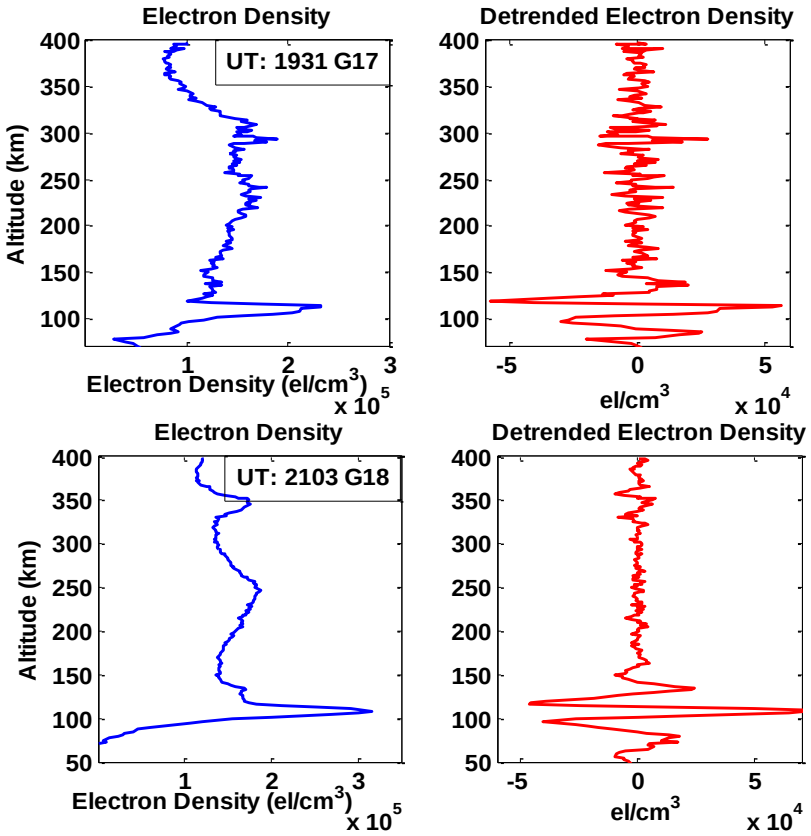

Figure 6.20 Electron density and detrended results for CHAMP RO events on October 29 2003

In Figure 6.20 there is a larger altitude range of E-region fluctuations than for the auroral electron density profiles shown previously. For altitudes above 150 km the fluctuations are observed to fill the whole F region with higher fluctuations than for normal profiles. Both the E- and F-regions generate more intense fluctuations than for moderately disturbed events. In this analysis of two RO events it is noted that scintillation models simulating SED effects must include electron density irregularities for all ionospheric altitudes such that signals experience the cumulative effect from all layers. In Figure 6.20 both of the density profiles have E-region enhancements; however, there are more fluctuations in the F region for the event at 1931 UT. Power spectral density analyses are shown in Figure 6.21. Both events show a peak at wavelengths in the range 10-20 km; this is also observed in the PSD of

auroral events for a wavelength of approximately 20 km. The power at the corresponding 10-20 km wavelength could arise from the significant electron density enhancement at 110 km. It is also noted that there are many spikes for 1931 UT event with wavelengths less than 10 km; this is the result of F region density fluctuations. Compared with the other events more power is observed in the small wavelength range - corresponding to the F region small-scale irregularities at 1931 UT.

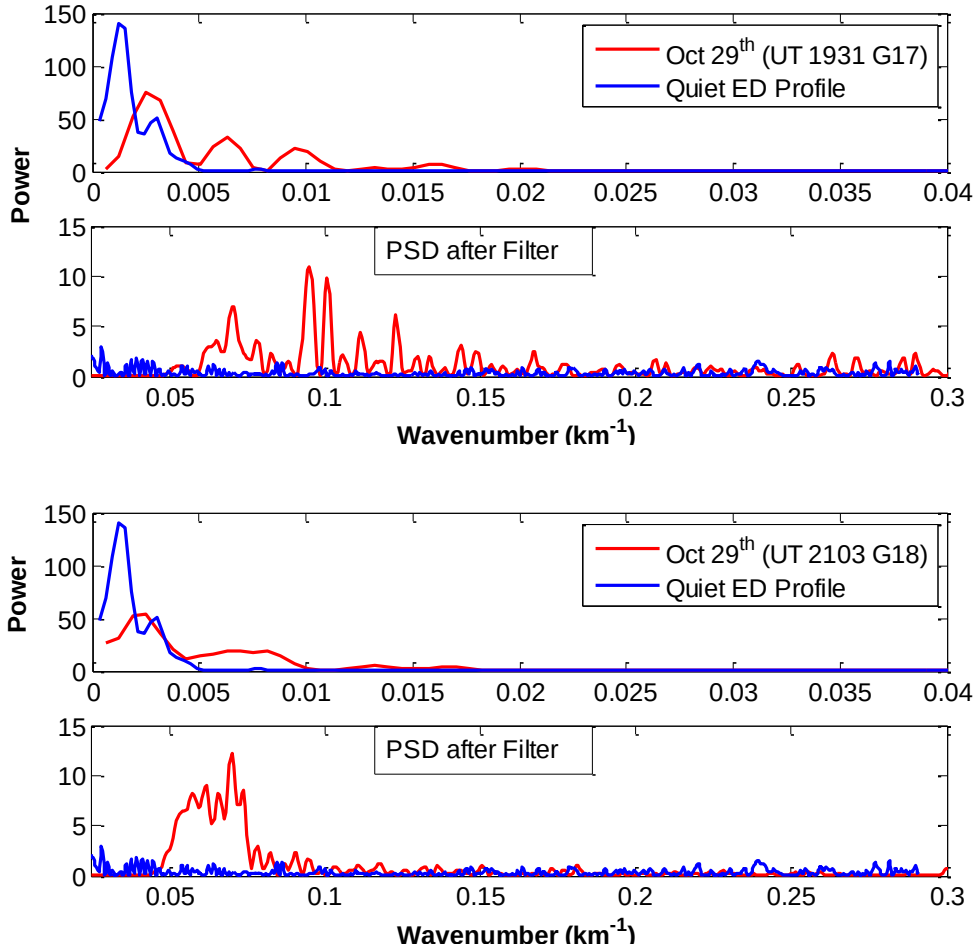

Figure 6.21 Power spectral analyses of electron density profiles for the two RO events on October 29 2003. The blue line is the quiet event in Figure 6.3 for comparison

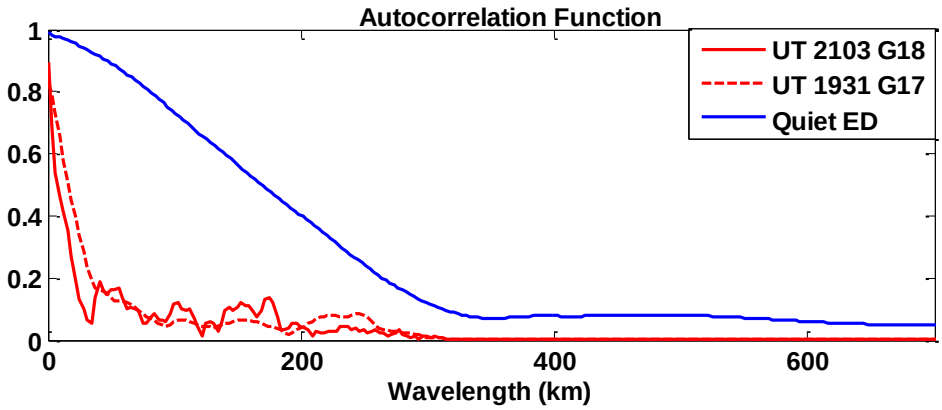

Figure 6.22 Autocorrelation function for electron density profiles on October 29 2003

The autocorrelation functions for electron density profiles are shown in Figure 6.22. The correlation index decreases more quickly with increasing wavelengths as compared with the former two selected cases. This is probably due to the existence of small fluctuations in the whole ionosphere which appear as noise in the electron density profile. Hence the correlation distance is small.

For Wavelet power spectrum analysis (Figure 6.23), compared with Figures 6.16 and 6.17, there is stronger power at altitudes above 200 km for structures with scale sizes from tens to hundreds of kilometers. There are also structures in the range 100-150 km at 110 km altitude corresponding to an E region enhancement in electron density. More ionospheric structures are defined in the F region; this shows that during the severe storm on October 29 2003 electron density irregularities with different scale sizes are distributed at all altitudes.

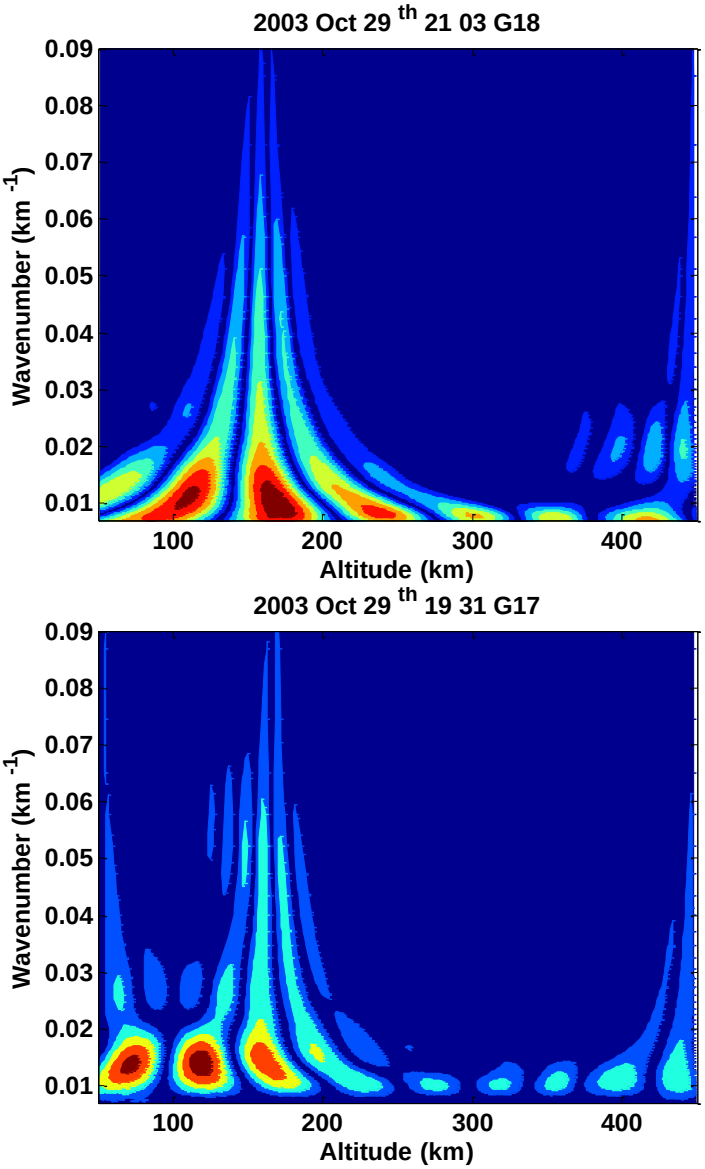

Figure 6.23 Wavelet power spectrum analysis for the electron density profiles during the severe storm on October 29 2003

6.3 SNR ANALYSIS

Figure 6.24 shows the SNR values for four RO events analyzed in previous sections (two auroral events (a and b) and two profiles from the October 29 2003 storm (c and d)).

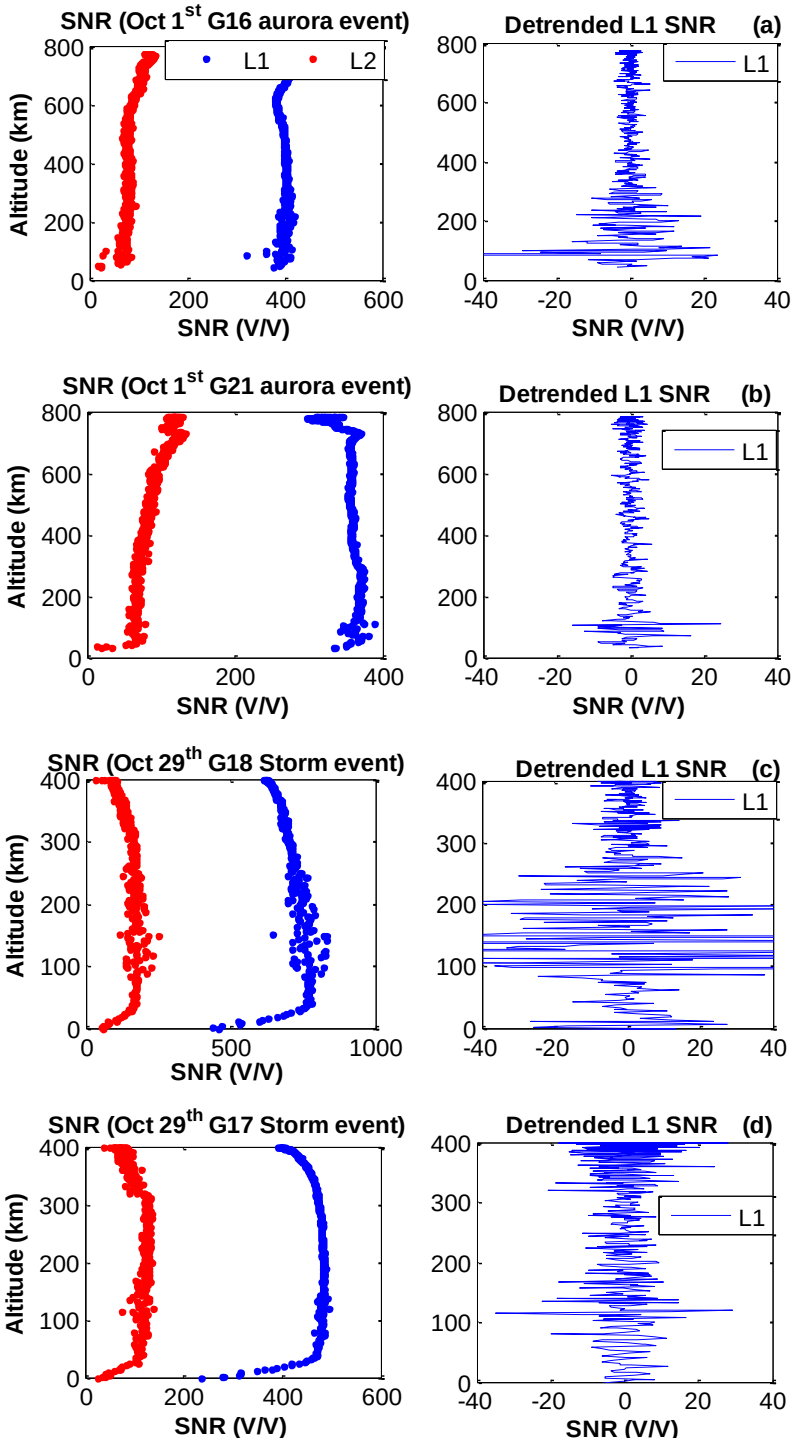

Figure 6.24 SNR and detrended L1 SNR (1 Hz sample rate) for the four events under different ionospherically disturbed conditions

The SNR fluctuations for GPS radio occultation are caused by layered structures in the ionosphere [*Wu et al.*, 2005]. To extract high frequency (small-scale) SNR perturbations the SNR data are detrended using a twenty point cubic polynomial approximation filter. Results are shown in the figures on the right. For the two auroral events the SNR fluctuates near 110 km. The G16 event also shows fluctuations extending to 200 km; such variations were not apparent in the electron density profiles. For the two SED RO events on October 29 2003 the SNR fluctuations are very large in both E and F regions. Radio occultation observations on October 29 2003 are derived under more intense ionospheric disturbances than for the other two cases. There are SNR fluctuations throughout all ionospheric altitudes for the 2003 storm events. SNR variations are introduced by ionospheric structures at a given altitude.

Analysis of the SNR variance is one way to demonstrate effects of ionospheric structures on satellite-based navigation system signals. Results show that AEI structures during ionospherically disturbed periods are disruptive for the LEO-GPS link. Under extreme storm scintillation conditions, fluctuations of satellite navigation signals are caused by cumulative effects of structures distributed throughout the entire ionosphere. SNR varies greatly in the disturbed E and F regions, and amplitude scintillation of GPS signals occurs at high latitudes.

6.4 TEC CALCULATED FROM RAW OBSERVATIONS

In the previous validation it has been noted that the Abel inversion to retrieve electron density profiles is inadequate due to the assumption of spherical symmetry during disturbed periods. The assumption is inadequate because of the existence of localized

irregularities and gradients. In this section the analyses are redone using TEC along the GPS-LEO line of sight for the same events considered previously. TEC is the total electron content measurement along the LEO-GPS line-of-sight. It is measured by using GPS L1 and L2 raw phase observations. TEC is mapped to the tangent point altitudes to create the profiles. TEC values from phase measurements are relative TEC. It is therefore assumed that the TEC series starts at a value of zero.

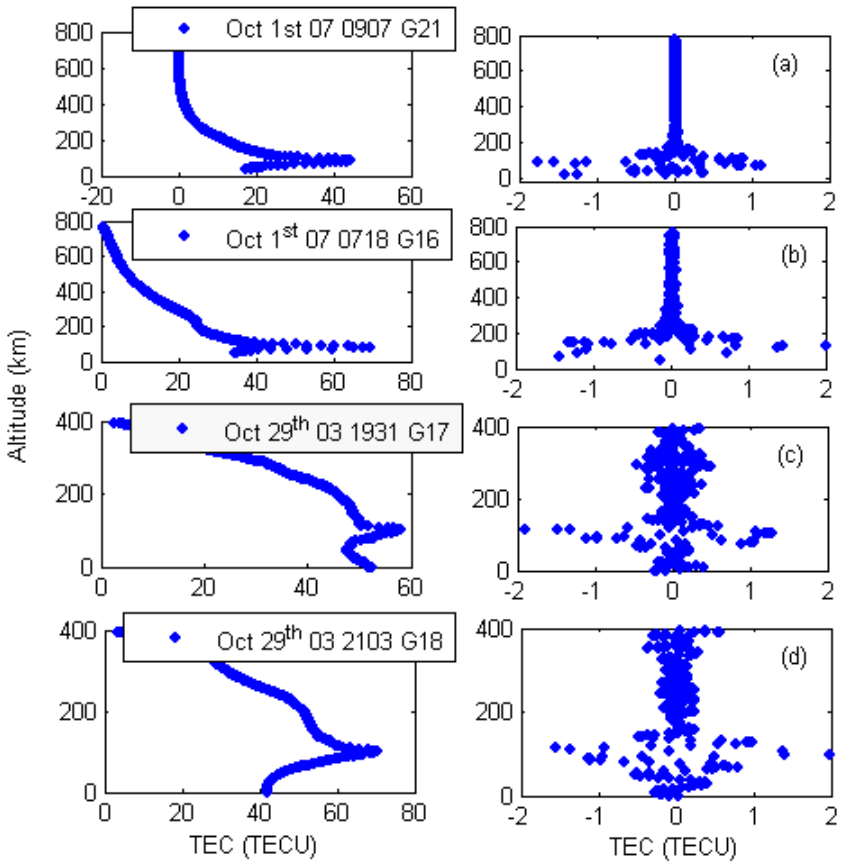

Figure 6.25 TEC profiles as a function of tangent points (left) and detrended results (right) for four events analyzed previously

TEC computed from raw observations shows the vertical distribution of electrons. Peaks are observed in Figure 6.25 at E-region altitudes for the two auroral events (a

and b). For the detrended TEC the vertical distribution of fluctuations shows almost the same characteristics as analyses of the electron density profiles. For the two events on October 29 2003 (c and d) the F-region fluctuations are larger than for the other two events; this is likely the cause of amplitude scintillation observed at ground GPS receivers. Wavelet analyses of the four TEC profiles are shown in Figure 6.26. The top two events (a and b) on October 1 2007 are COSMIC RO events with tangent points in the auroral region. Power is distributed mainly in the altitude range 100-150 km. Events on October 29 (c and d) are CHAMP RO observations during the severe storm period. The power is distributed from the E region to above 200 km altitude; this shows features similar to those derived for wavelet analyses of the electron density profiles.

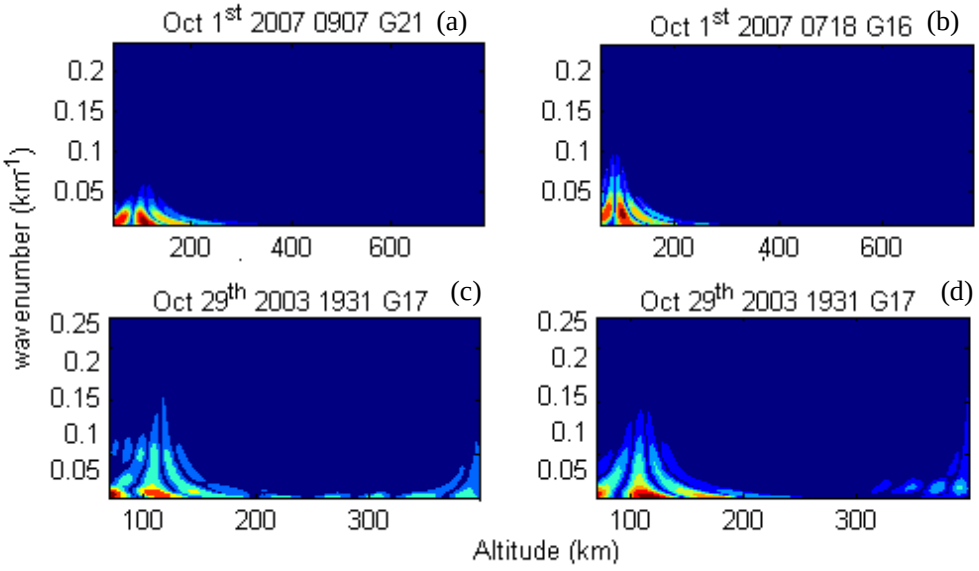

Figure 6.26 Wavelet power spectrum analysis for TEC profiles

This chapter applies PSD analysis to analyze radio occultation measurements under disturbed ionospheric conditions. Information is obtained about the ionosphere

vertical structures' scale size, spatial distribution and intensity. The AEI electron density profiles show fluctuations around 110 km and SED events show the fluctuation for the whole altitude range (E plus F regions). The observed results are generally in accordance with known physical processing controlling the high latitude plasma. The analyses not only provide information about ionosphere irregularity distribution at high latitude but also demonstrates the potential of RO for ionosphere monitoring of disturbed conditions.

CHAPTER 7

MAPPING OF HIGH-LATITUDE IONOSPHERIC IRREGULARITIES USING COSMIC OBSERVATIONS

7.1 OBSERVATION AVAILIBILITY

The goal of COSMIC is to provide approximately continuous 24 hours of local time coverage globally [*Lei et al.*, 2007]. However it is still not be achieved as described in Section 4.2. Figure 7.1 is an example of the distribution of tangent points for RO observations from five COSMIC LEO FORMOSAT-3 satellites over a two-hour interval. The local time sector is 0000 to 0200. The geometry of COSMIC satellites causes most of the RO events to occur in the western hemisphere (for the selected two-hour local time period on September 2 2007). For studies in this thesis only days with enough RO events in the high-latitude western hemisphere during local night time (Canadian region) are chosen to create ionosphere maps.

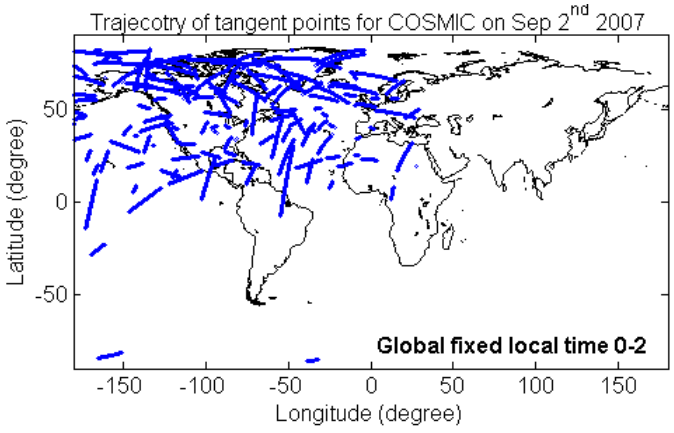

Figure 7.1 Distribution of tangent points for COSMIC RO with observations in local time sector 0000 to 0200 September 2 2007

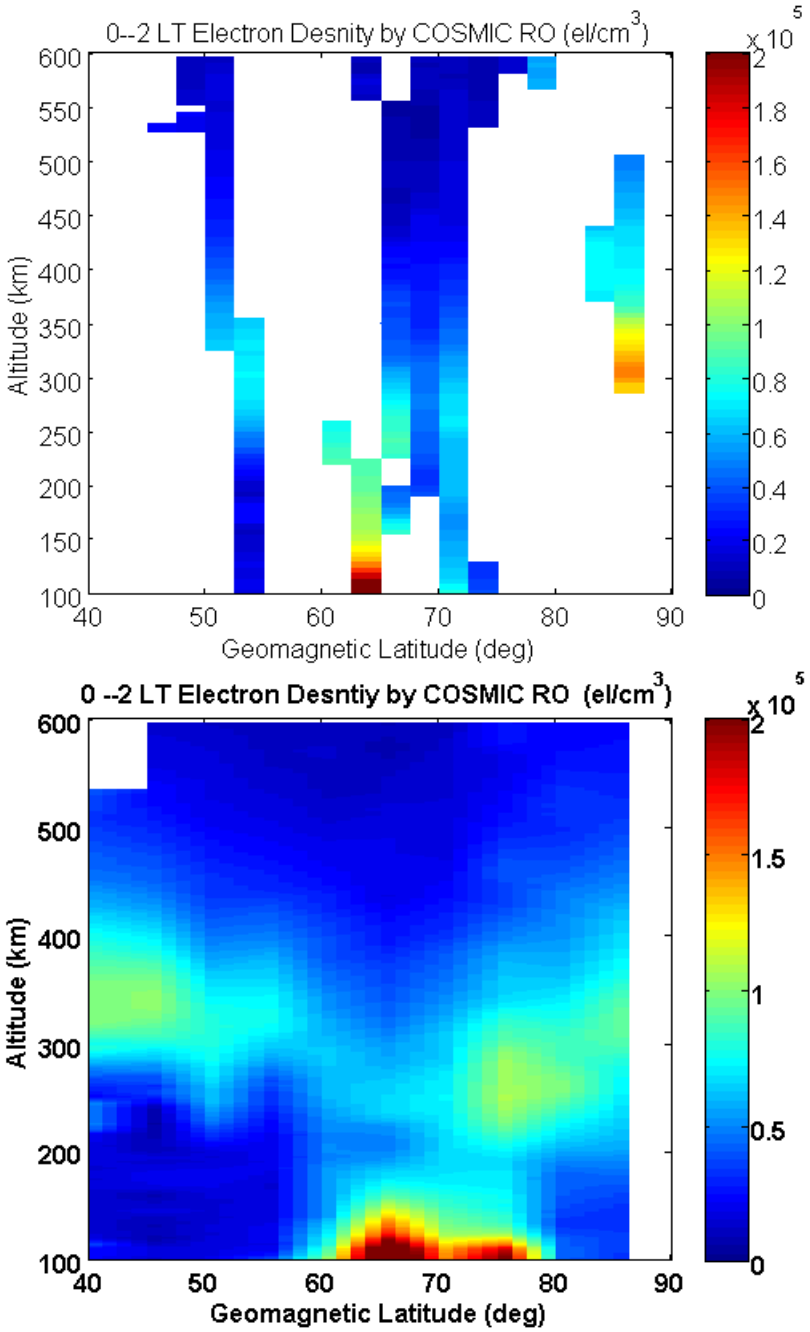

Figure 7.2 Averaged electron density map with observations from different longitude sectors (150˚ W - 160˚ W) (top) and (60˚ W - 160˚ W) (bottom), September 2 2007

Figure 7.2 is another example showing the observation availability for the selected time period from Figure 7.1. Figure 7.2 shows electron density observations from

COSMIC RO mapped to geomagnetic latitude and altitude. The top plot only uses observations averaged over 10 degrees of longitude while the bottom plot includes observations in the extended sector of the western hemisphere from 60 deg to 160 deg. RO events at different longitudes are mapped into the same latitude and altitude grid. The map is therefore an average latitude and altitude distribution of electron density in a given longitude sector for the high-latitude western hemisphere. Bins with no values available are shown as white pixels. It is noted that ionospheric activity levels were high on September 2 2007; the geomagnetic K index (Alaska) was greater than 5 for the period studied [*NOAA*, 2009].

It is noted that RO observations are undersampled in the Alaska longitude sector due to the geometry of COSMIC satellites. In order to create full maps observations are chosen from a wider longitude sector (60 deg W to 160 deg W) with ionospheric activity levels inferred from magnetometer observations in GIMA, CARISMA, and GSC networks. Magnetic time series from Alaska (GIMA) and the other two networks show significant magnetic field fluctuations in the local time range 0000 to 0400 LT on this day [*GIMA*, 2009; *GSC*, 2009; *CARISMA*, 2009]. An electron density enhancement in the geomagnetic latitude range 60-80 deg N is observed near 110 km altitude in Figure 7.2 for the two-hour local time sector.

A similar map is generated in Figure 7.3 with observations from December 8 2007 which is a magnetically quiet day for comparison purposes. The planetary Kp index was zero for the entire quiet day [*NOAA*, 2009]. In contrast to the bottom plot of Figure 7.2, no large E-region electron density enhancement exists. Typical F-region electron density peaks are observed. In the previous example (Figure 7.2) E-region electron density enhancements observed from COSMIC RO observations are consistent with patterns of energetic electron precipitation expected for auroral

substorm phenomena.

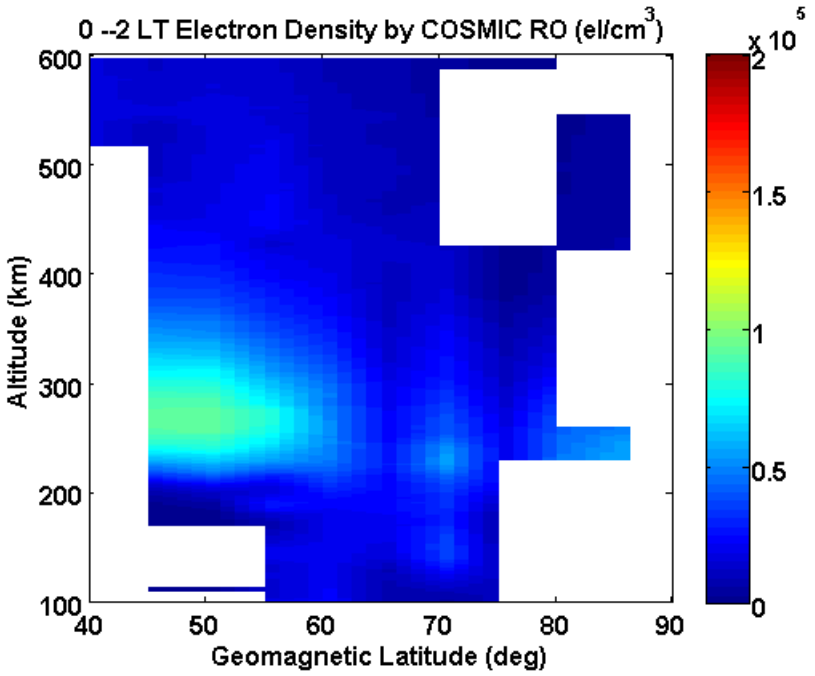

Figure 7.3 Averaged electron density map from COSMIC RO observations in the longitude sector (60° W to 160° W), December 8 2007

Note that the electron density plots are created by averaging observations from different longitude sectors because the insufficient observations of COSMIC; future expanded radio occultation missions are expected to achieve instantaneous global coverage with full local time sector coverage and resolution high enough to monitor ionospheric disturbed conditions continuously.

7.2 ANALYSES OF DISTURBED IONOSPHERE

7.2.1 ANALYSIS OF AURORAL EVENTS

Four successive ionospherically active nights were observed December 4 to 7 2008. In Figure 7.4 magnetometer observations between 1000 and 1200 UT in Alaska show decreases in the H (north-south) magnetic component consistent with the presence of an enhanced westward electrojet - and auroral substorm events. Based on GIMA observations in Figure 7.4 it can be determined that the ionosphere is disturbed 1000-1200 UT; this corresponds to 0000-0200 LT in Alaska.

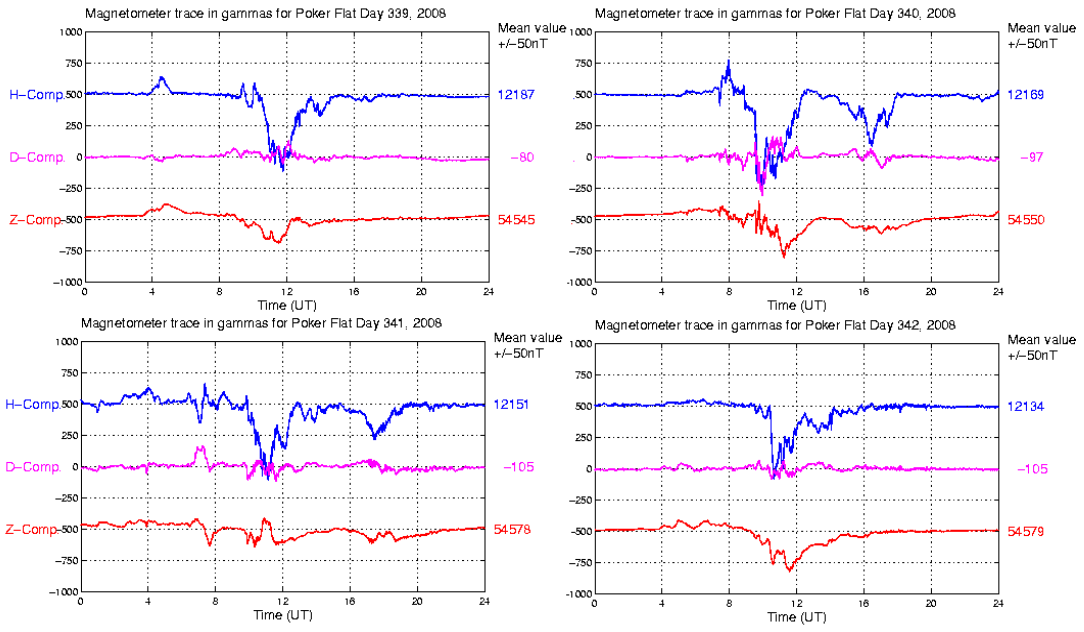

Figure 7.4 Geomagnetic field measured at Poker Flat December 4 to 7 2008, [*GIMA*, 2009]

COSMIC measurements are selected for this four-day period. Figure 7.5 is derived from such observations for the period 0400 to 2000 UT for the four days. COSMIC electron density observations within the same longitude and same latitude sector are compiled and averaged in a grid. The electron density observations are selected in the altitude range 100 km to 120 km corresponding to the altitude of AEI.

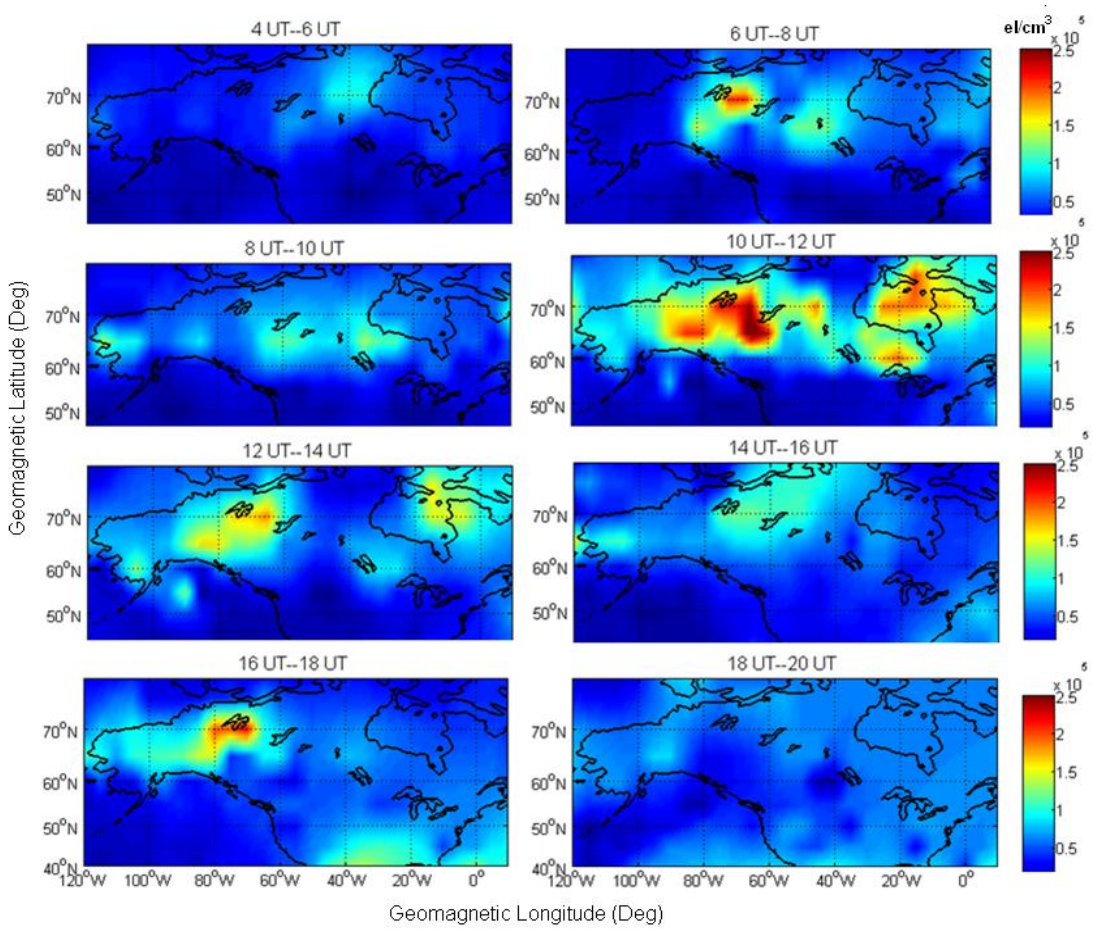

Figure 7.5 COSMIC electron density observations for altitude range 100-120 km generated from COSMIC measurements every two-hour time sector from 0400 to 2000 UT, as averaged over four days (December 4 2008 to December 7 2008) in geomagnetic coordinates

In Figure 7.4 magnetometer observations indicate that 1000 to 1200 UT is the most disturbed period for each of the four days. Accordingly in Figure 7.5 the E-region

electron density is enhanced at 60° W and 90° W geomagnetic longitude, which illustrates significant electron precipitation in the ionospheric E region near Alaska. Except the major decrease period of H component of magnetic field in Figure 7.4 two additional periods of geomagnetic fluctuations (0600-0800 UT and 1600-1800 UT) are also observed on December 5 and 6. Correspondingly the electron density is enhanced near Alaska (90° W) in Figure 7.5 for these two periods. The correlation between geomagnetic variations and electron density enhancement reflects the nature of the physical processes. The auroral electrojet current grows (causing a negative magnetic field perturbation) during the precipitation of energetic electrons into the E-region along magnetically field-aligned currents (refer to Section 3.2.2.1).

7.2.2.1 CO-LOCATED ELECTRON DENSITY PROFILES

Electron density profiles are compared for different levels of ionospheric activity. Figure 7.6 shows profiles for December 3 and 4, and December 7 and 8 2008. Note that December 7 and December 4 are ionospherically disturbed days and December 3 and 8 are quiet days. The GPS satellite orbital period is approximately 12 hours; the COSMIC LEO satellite orbital period is approximately 100 min. A RO event can happen at almost the same location but 20-30 min earlier for a given COSMIC LEO-GPS pair on successive days. Co-located electron density profiles are derived from such observations to determine the ionospheric variations introduced by substorm effects.

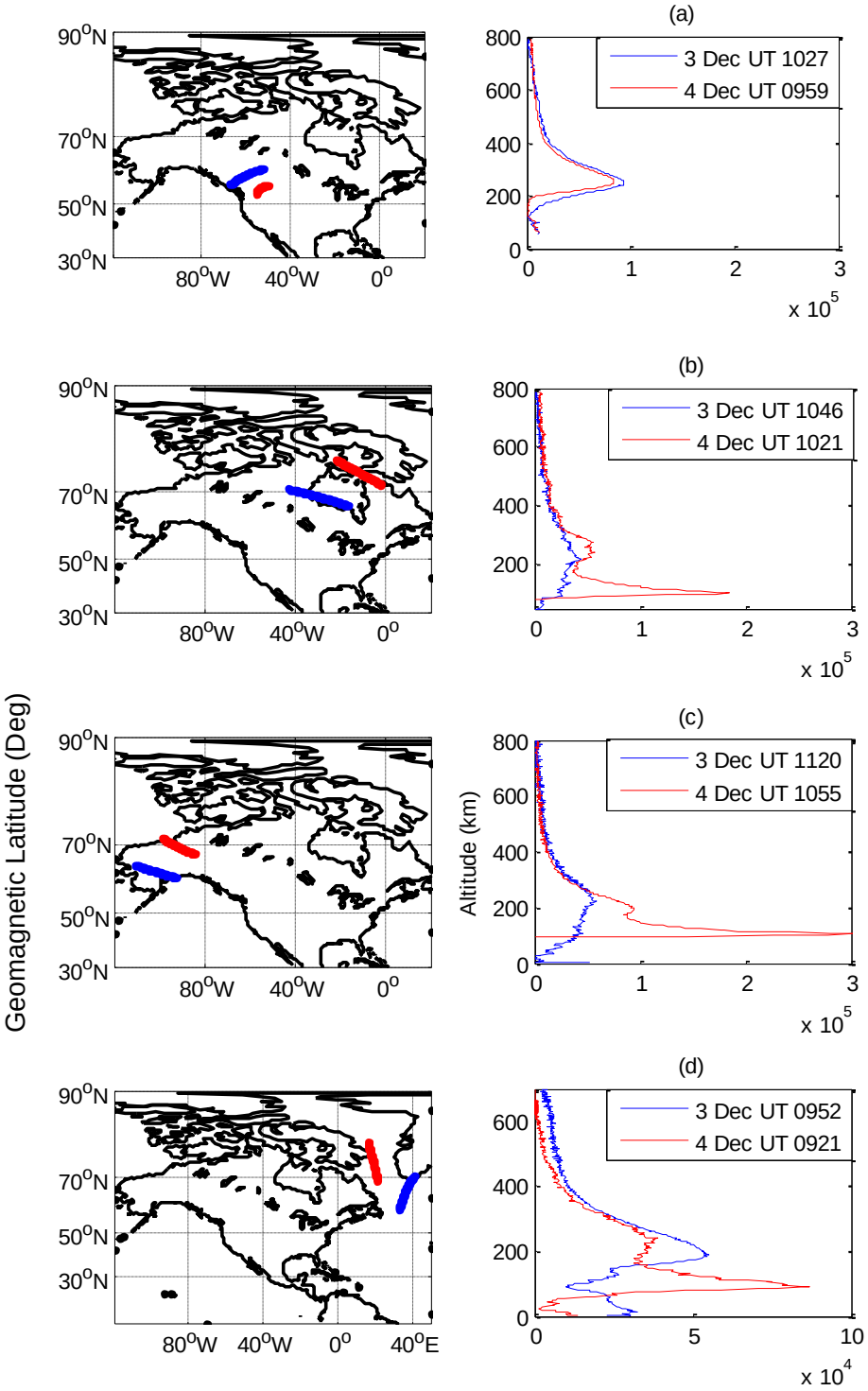
(a)
(b)
(c)
(d)
3 Dec UT 1027
4 Dec UT 0959
3 Dec UT 1046
4 Dec UT 1021
3 Dec UT 1120
4 Dec UT 1055
3 Dec UT 0952
4 Dec UT 0921
Geomagnetic Latitude (Deg)
Altitude (km)
90°N
70°N
50°N
30°N
80°W
40°W
0°
40°E
x 10^5
x 10^4

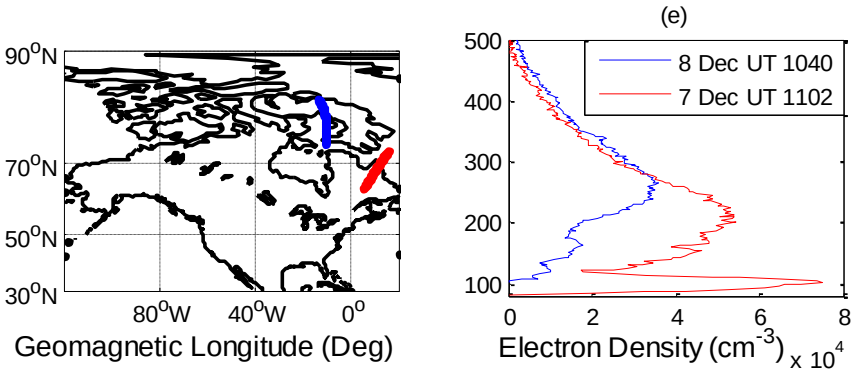

Figure 7.6 Five co-located pairs of COSMIC electron density observations (right) during ionospherically disturbed days (red line for December 4 and 7) and quiet days (blue line for December 3 and 8). Trajectories of RO tangent points are shown in maps (left) (blue dots correspond to the blue profiles on the right and red dots correspond to the red profiles on the right)

Figure 7.6 shows comparisons of five pairs of co-located COSMIC RO events for quiet versus disturbed periods with one day difference. Events in plot (a) occur at latitudes less than 60° geomagnetic, which is likely equatorward of the auroral oval. The two plots in figure (a) match quite well, with an F-region electron density peak typical of average ionospheric conditions; it can be inferred that ionospheric storm conditions are minimal in this latitude sector for the dates considered. Other plots ((b) to (e)) occur at relatively higher geomagnetic latitudes. The disturbed electron density profiles show obvious E region enhancements compared with co-located quiet density profiles. Plots (b), (c) and (e) also show local electron density peaks in the F region (200-300 km) compared with quiet day profiles.

From these observations, the AEI enhancement is determined to occur within 10-20 km of 110 km altitude with a magnitude up to 10^5el/cm^3. The maximum F region enhancement at altitudes 150-300 km is 5×10^4 el/ cm^3. There are no major differences

for the disturbed versus quiet profiles at altitudes higher than 300 km. From this example (Figure 7.6) electron density variations introduced by ionospheric storm effects can be summarized as 1) significant AEI near 110 km altitude with 10-20 km vertical scale, and 2) relative enhancement at F region at altitudes 150-300 km.

7.2.2.2 DENSITY MAPS FOR DIFFERENT ALTITUDES

Magnetometer observations between 1000 and 1200 UT in Alaska show decreases in the H component in Figure 7.4. Disturbed ionosphere periods are also selected using other high latitude magnetometer stations. Based on magnetometer observations of the entire Canadian region, corresponding COSMIC RO measurements have been selected during the period 4-7 December 2008. Spatial distribution and periods of disturbances are identified using GIMA, CARISMA and GSC data. Figure 7.7 is derived from the selected electron density observations at altitudes 100-120 km (top) and other altitude ranges for night time sectors of the four days. Four days of observations are included because there are not enough COSMIC RO measurements for a single day to create a full electron density map. A plot is compiled from all electron density measurements during disturbed periods for the given interval of local time. COSMIC electron density observations within the same geomagnetic latitude and local time sector bins are averaged to derive the grid of values in Figure 7.7.

The top plot is electron density observations selected for altitudes 100-120 km (corresponding to the altitude of AEI). In that plot all density enhancements generally occur above geomagnetic latitude 60 deg N; this is near the equatorward boundary of the auroral oval. Localized electron density enhancements are from 2-3 $\times 10^5$ el/cm^3.

(a)

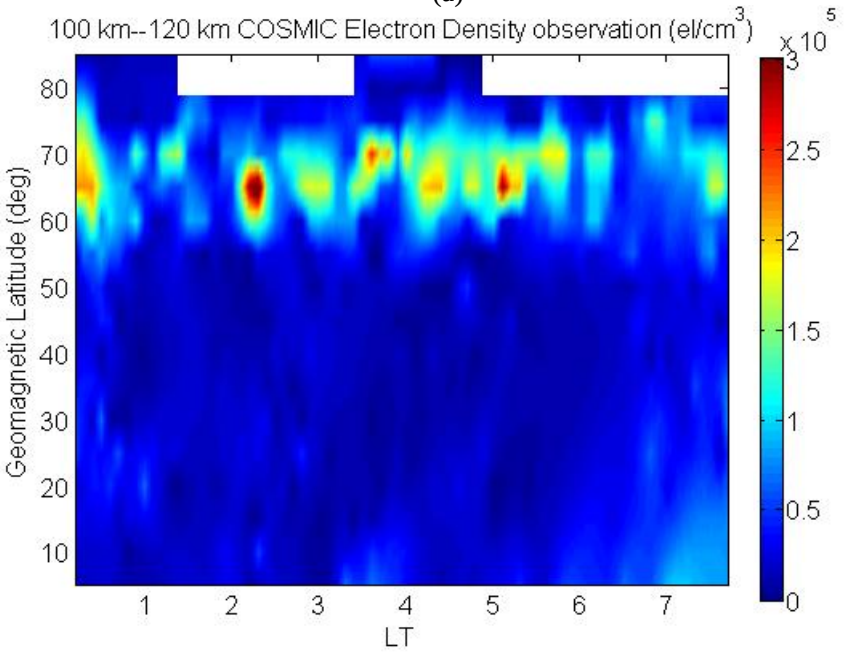
100 km--120 km COSMIC Electron Density observation (el/cm3)
x 10^5
Geomagnetic Latitude (deg)
LT

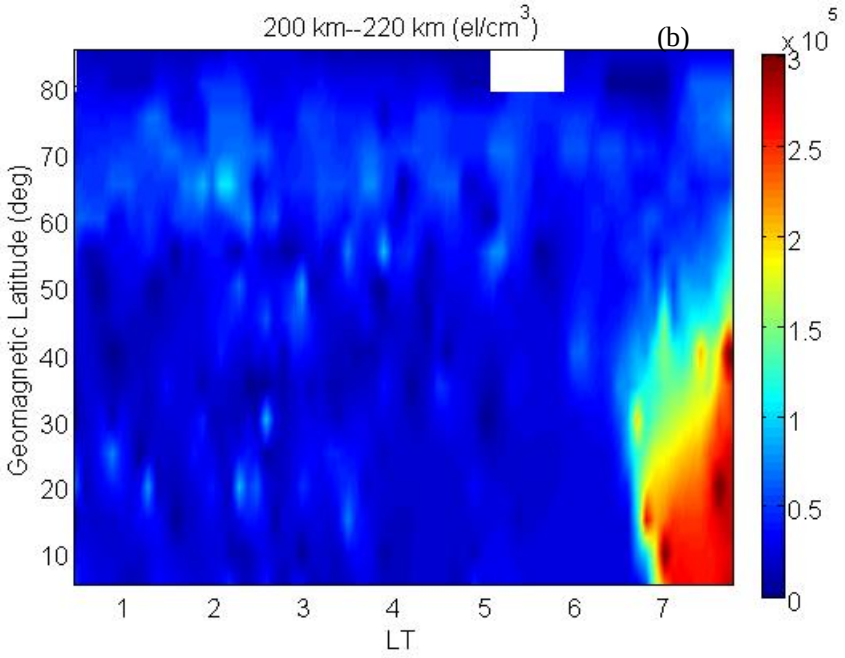
200 km--220 km (el/cm3)
(b)
x 10^5
Geomagnetic Latitude (deg)
LT

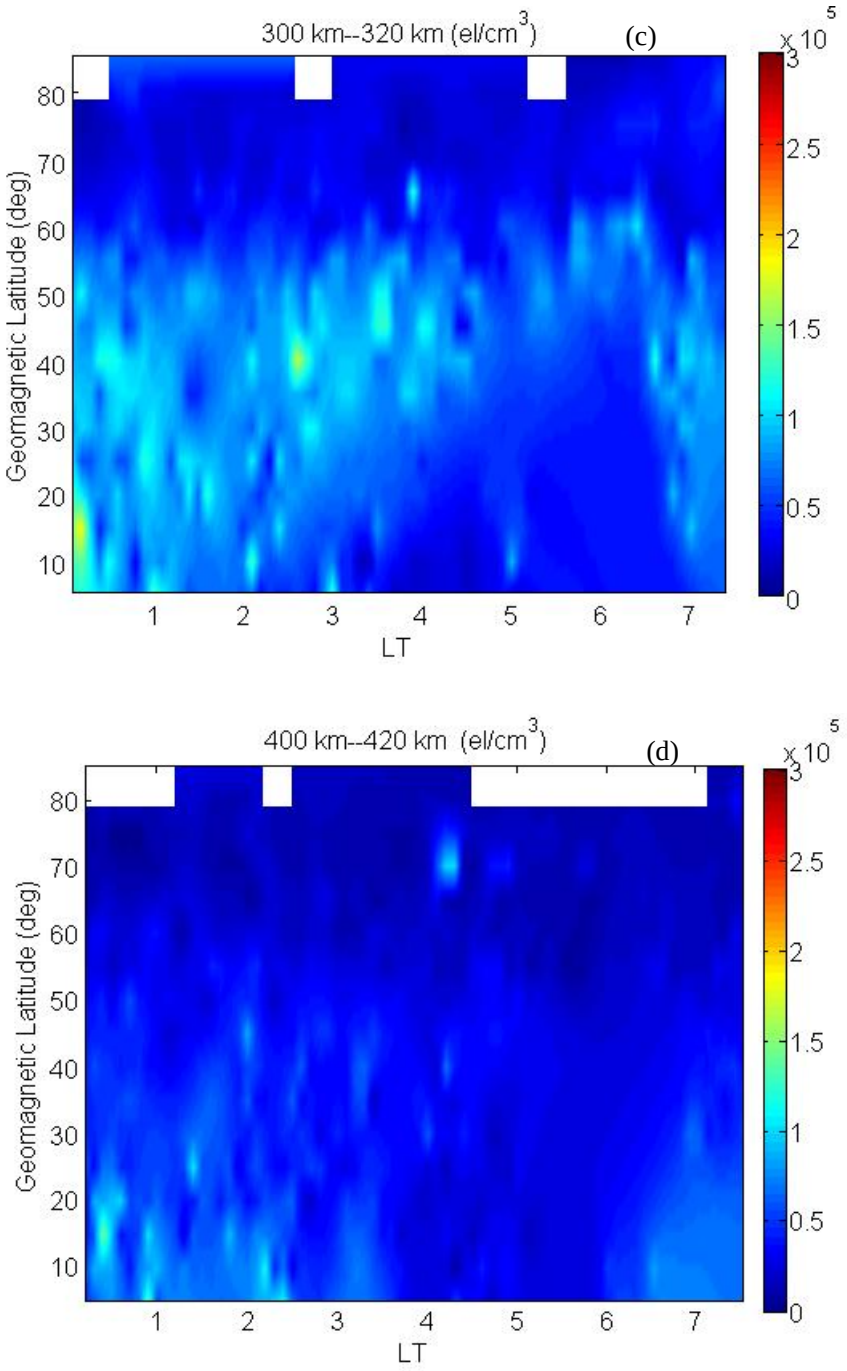

Figure 7.7 COSMIC electron density observations for altitude ranges (top to bottom) (a) 100-120 km, (b) 200-220 km, (c) 300-320 km, and (d) 400-420 km, generated from COSMIC measurements 0000-0800 LT for four days (4-7 December 2008)

For the plot of electron density at 200 km altitude F-region enhancements occur at 0700 LT which is before sunrise at the terminator location. The ionization starts at lower latitudes around 0600 to 0700 local time as the sun rises. The enhancement of density is from the beginning of ionization of a new day. For 300 km and 400 km altitudes the density maps do not show obvious enhancement at auroral latitudes. It is also observed that there is enhancement of electron density at mid-latitudes for F-region altitudes of 300 km after midnight. With observations of electron density in the altitude range 100-120 km the significant density enhancement is captured. The correlation between magnetometer observations and spatial distribution of electron density enhancement is consistent with the expected occurrence of AEI during geomagnetic disturbances and associated auroral substorms. RO events from COSMIC are able to capture the AEI feature from vertical electron density profiles directly. The density at E region associated with AEI is comparable to the density of F region during daytime, which is formed by the electron precipitation from the field-aligned current.

A further comparison is made by plotting electron density maps compiled from COSMIC measurements for quiet periods. Four quiet days from November 30 to December 3 with geomagnetic K index being 1 or 0 for high latitude region are identified. Observations of COSMIC RO for altitudes 100-120 km show no significant electron density enhancement at auroral oval latitudes in Figure 7.8. The F-region density enhancement near sunrise can still be observed for altitudes of 200-220 km. And the mid-latitude enhancement can be observed for 300 km altitude. The major difference between disturbed density maps (Figure 7.7) and quiet maps (Figure 7.8) for different altitude ranges is the high latitude density enhancement at 100 km for geomagnetically disturbed local nighttime - as associated with the auroral activity.

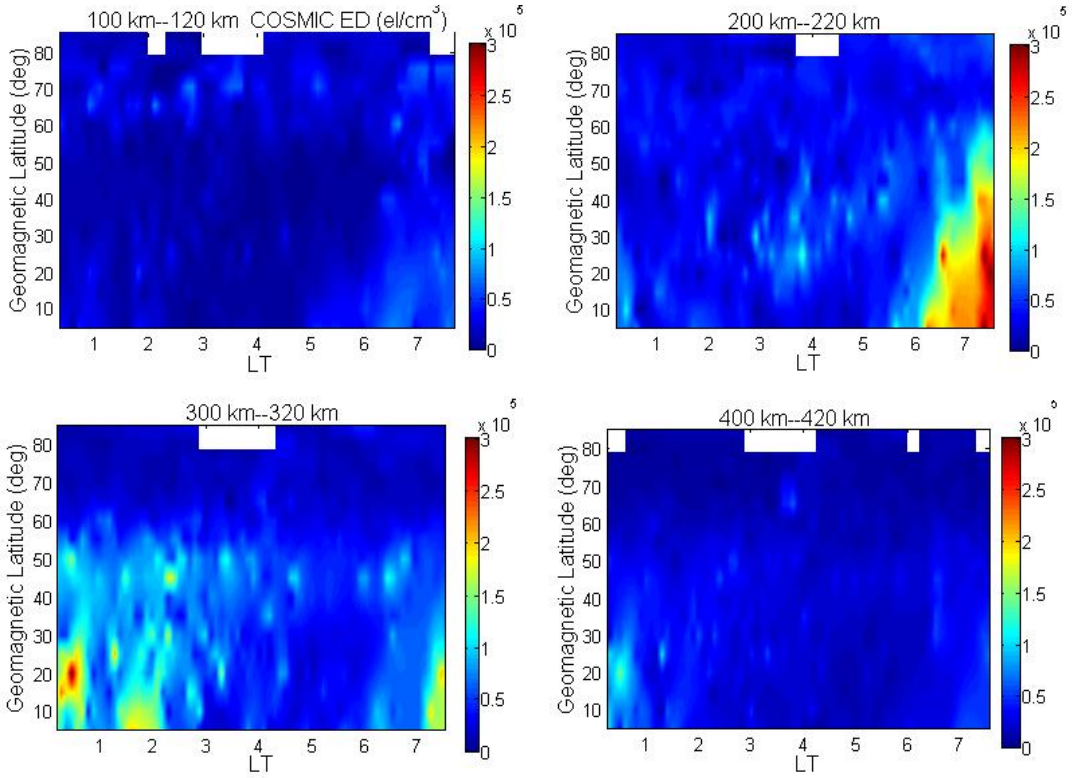

Figure 7.8 COSMIC RO electron density observations for altitude ranges 100-120 km, 200-220 km, 300-320 km, and 400-420 km, as generated from COSMIC measurements 0000-0800 LT for four days (November 30 to December 3 2008)

In order to show the electron enhancement of AEI feature more clearly, electron density differences are calculated for different altitude ranges between quiet observations in Figure 7.8 and disturbed observations in Figure 7.7. Figure 7.9 is generated by using electron density measurements obtained from the four disturbed days of Figure 7.7 subtracting density values in the grid with the same local time and geomagnetic latitude of the quiet days of Figure 7.8. The largest differences are observed in the top plot (100-120 km altitude) for the nighttime hemisphere; E-region electron precipitation enhancement above 60° N can reach 3×10^5 el/cm^3. For electron density differences at 200 km, 300 km and 400 km altitude the values are not that regular and found mainly for mid- and low-latitude regions. The ionosphere is also

active for mid- and low-latitude regions after local midnight and at sunrise due to other ionospheric phenomena. However the results in Figure 7.9 show that for different high-latitude altitude ranges the major difference is the enhancement around 100 km altitude associated with electron precipitation during auroral storm periods.

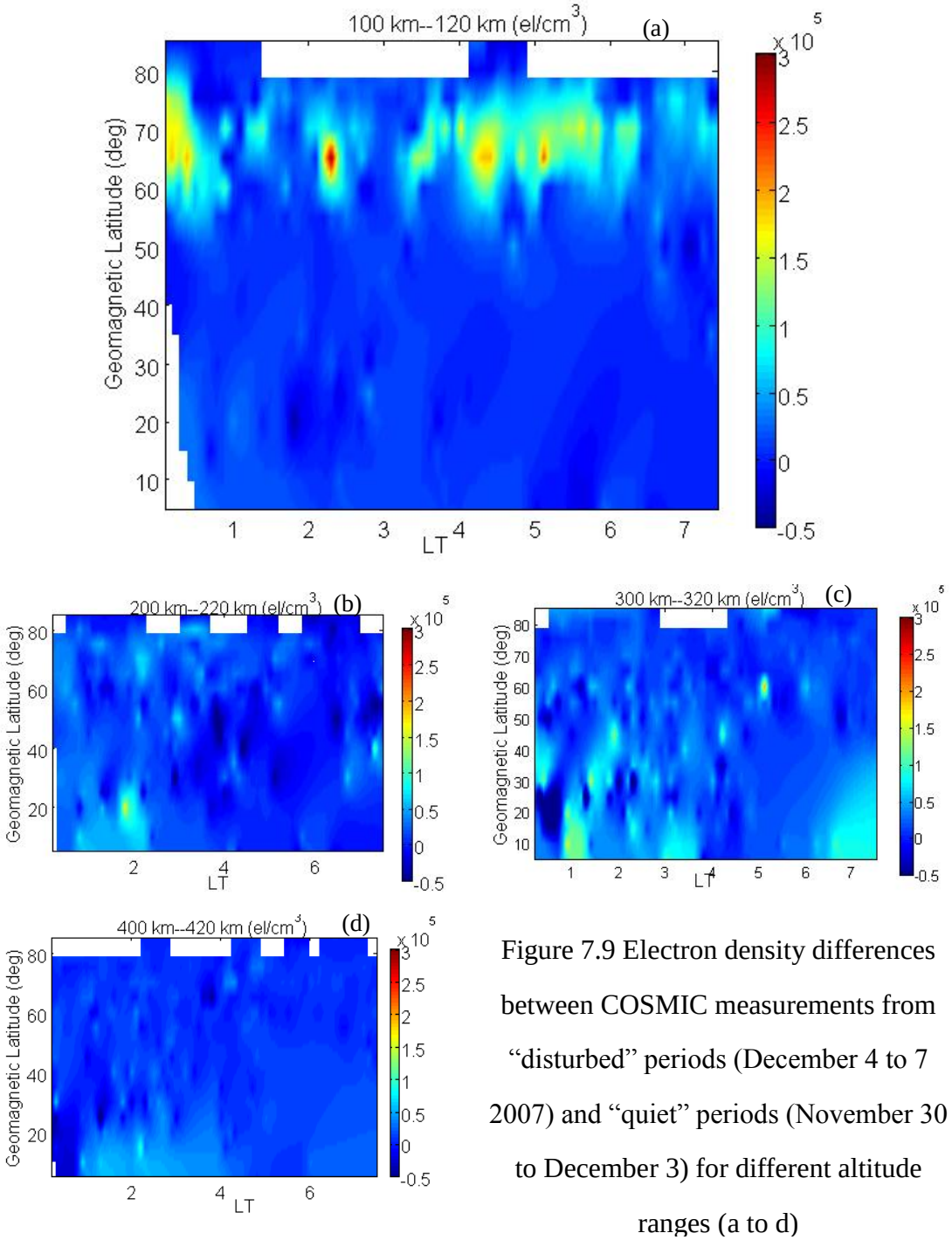

Figure 7.9 Electron density differences between COSMIC measurements from "disturbed" periods (December 4 to 7 2007) and "quiet" periods (November 30 to December 3) for different altitude ranges (a to d)

7.3 TEC MAPS

Figure 7.10 shows TEC estimates for the E and E-plus-F regions, as derived by integrating COSMIC electron density with respect to altitude for observations from the four ionospherically disturbed nights presented in previous sections. The top plot shows total electron content integrated for the E-region altitude range 90-120 km (corresponding to the AEI altitude). Good correlation can be found between TEC enhancements and electron density enhancement 100-120 km altitude in Figure 7.7.

For the E region, enhanced TEC occurs in the geomagnetic latitude range 60-70 deg N during local nighttime, which is mainly due to electron precipitation during storm periods. The plot indicates that AEI can introduce TEC enhancements around 1 TECU for the layer 90-120 km altitude; corresponding to 16 cm range delay for GPS L1 signals. Moreover the electron enhancement is not distributed symmetrically. AEI is characterized by localized irregularity structures with large horizontal and vertical gradients. AEI with horizontal scale sizes of dozens or hundreds of kilometers will cause phase scintillation at high latitudes during auroral nighttime.

The bottom plot in Figure 7.10 shows TEC derived from integrated COSMIC electron density profiles 90-600 km altitude from 0000 to 0800 LT. The obvious enhanced TEC around 0600 and 0700 LT below 60 °N is due to solar radiation (and ionization) near the terminator. The enhanced TEC can also be observed at high latitudes above 60 deg N for 0100 to 0700 LT. The high-latitude enhanced TEC 90-600 km altitude comes from the E-region electron precipitation (AEI - first plot in Figure 7.7) and also F-region enhancement at 200 km altitude (second plot in Figure 7.7).

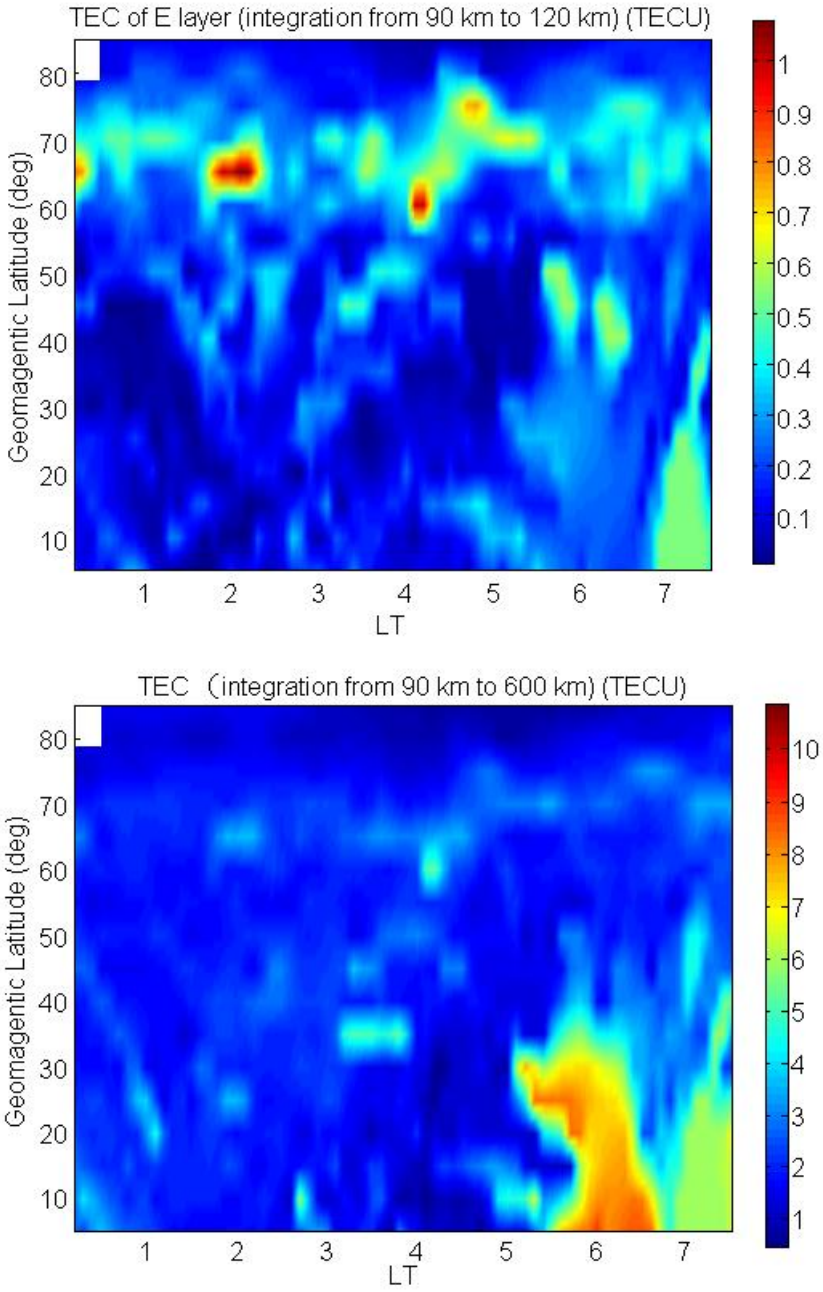

Figure 7.10 TEC integrated from COSMIC electron density observations (December 4-7 from 0000 to 0800 local night time) for E layer 90-120 km altitude (top) and E and F layer combined 90-600 km altitude (bottom)

Differences between TEC measurements for quiet versus disturbed periods are shown in Figure 7.11. TEC differences are calculated by subtracting quiet TEC values from disturbed values for a given geomagnetic latitude and local time. Results are computed for the E region 90-120 km altitude and E-plus-F region 90-600 km altitude; only geomagnetic latitudes above 55 deg N are shown.

Figure 7.11 shows that E-region enhancement (due to AEI) during disturbed periods is the main contributor to TEC measurement perturbations from the quiet ionosphere values. The TEC enhancement associated with auroral periods is approximately 1 TECU from E region. And the density enhancement of AEI can extend to a wider altitude range; the full TEC enhancement for altitudes 90-600 km can reach values of 1-3 TECU at the same location. For GPS applications the delay caused by structures of AEI are from 0.15 meters to 0.45 meters for L1 frequency in addition to the normal ionospheric range delay for enhancement from both the E and F region. From the density observation comparison in Figure 7.6 there are still enhancements at 200 km altitude at auroral latitudes that introduce TEC enhancement coming from F region altitude.

Hunsucker et al. [1995] conclude that the occurrence of specific TEC signatures due to large- and medium-scale E region structures can be utilized as the predictor/monitor of AEI within the auroral oval. In Figure 7.6 comparisons disturbed versus quiet conditions were conducted for single cases. The AEI enhancement can reach to higher than 200 km altitude (plots b, c, e) for auroral density profiles. From the analyses presented here TEC is expected to increase by 1-3 TECU for disturbed versus quiet conditions. It can also be concluded that the AEI feature can have 1 TECU enhancement around 110 km altitude.

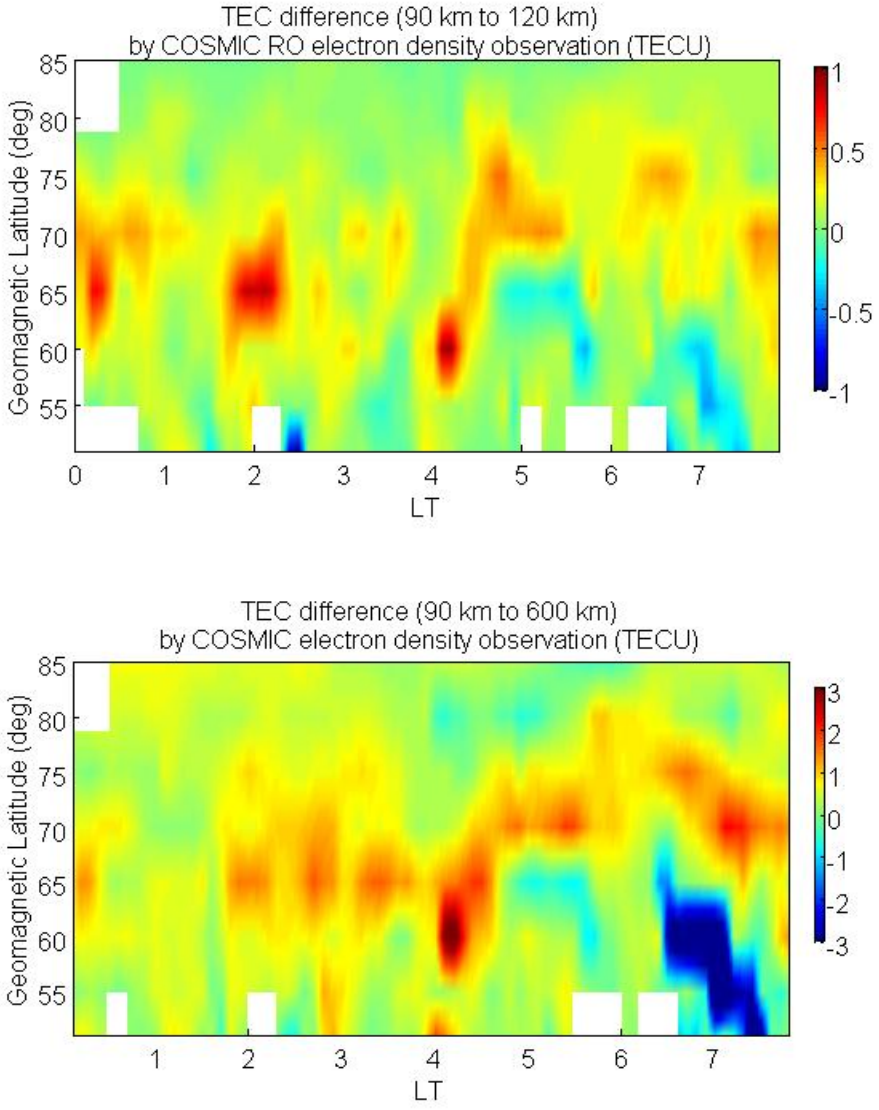

Figure 7.11 TEC differences between COSMIC measurements from “disturbed” periods (December 4-7 2008) and “quiet” periods (November 30 to December 3 2008) for different altitude ranges (90-120 km top plot, 90-600 km bottom plot) from 0000 to 0800 local time

Hunsucker et al. [1995] and *Coker et al.* [1995] determined that the AEI structures are associated with 1 to 2 TECU change in TEC; this result was derived by applying a filter to ground-GPS line-of-sight TEC observations. Such results are similar to the results obtained in a different manner here by exploiting COSMIC RO capabilities.

COSMIC observations are used to estimate electron density profiles and identify TEC perturbations in different altitude ranges. Analyses reveal dominant features of ionospheric activity introduced in specific altitude ranges. Moreover it is observed from COSMIC observations that the ionospheric structures are more extensive, and distributed over a wide range of altitudes, than represented by a simple model of ionospheric irregularities with assumption of one single phase screen. During auroral substorms multiple phase screen modeling is necessary for realistic ionosphere simulations in support of scintillation studies.

While the dataset used here is from solar minimum periods it is expected that the TEC or electron density change could be more significant for storm events during solar maximum periods (e.g. the severe storm in October 2003). GPS satellite signals may experience degraded performance from ionospheric irregularities in local regions with TEC enhancements introduced by auroral substorm effects. The additional range error caused by the AEI structures can be associated with large horizontal TEC gradients which also degrade the accuracy of safety-critical navigation systems such as the Wide Area Augmentation System (WAAS).

7.4 MAPPING E AND F REGION FLUCTUATIONS

In Chapter 6 the "Lombscargle" method was applied to calculate power spectral densities for COSMIC RO case studies. PSD analysis can provide information about ionospheric structures for different scale sizes. It was noted that peaks at small wavelengths (20 km) are typical for AEI electron density profiles. To better establish the occurrence and distribution of AEI at high latitudes, maps of intensity from power spectral analysis are shown for densities at smaller wavelengths.

Figure 7.12 shows PSD comparisons for a "quiet" RO electron density profile and a "disturbed" electron density profile. One region is selected for analysis: wavelengths of 10-50 km; this reflects medium scale size structures. This range includes wavelengths dominant in previous analysis of AEI profiles (e.g. Figure 6.14); the goal of this analysis is to capture the distribution of such smaller electron density structures. The average spectral density value is computed and normalized to determine geographic distribution using the COSMIC electron density observations from ionospheric disturbed periods.

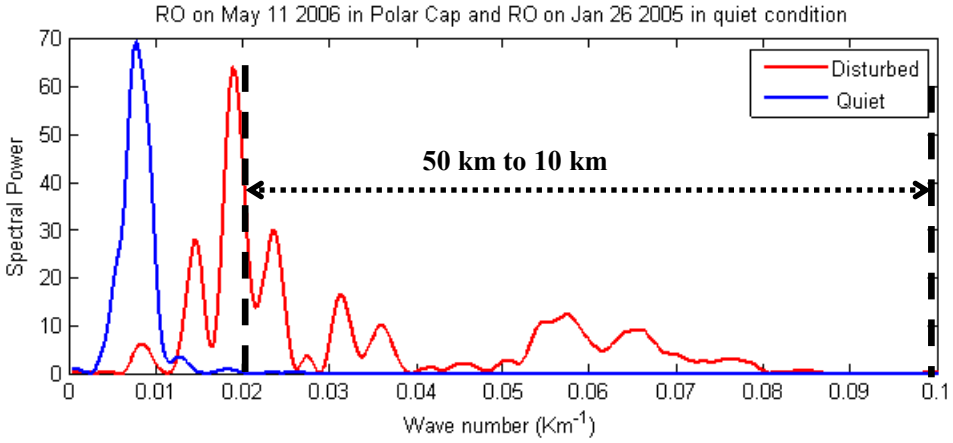

Figure 7.12 Spectral power of electron density profiles for selected occultation events

Power spectral densities for electron density values in Figure 7.7 for the limited wavelength range 10-50 km are shown in Figure 7.13. The results are normalized with the maximum power set with value of 100.

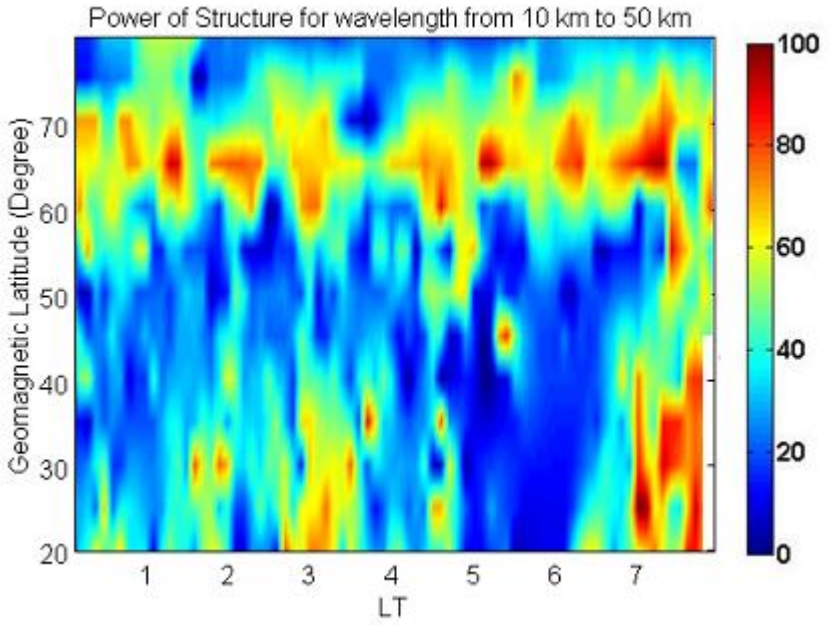

Figure 7.13 PSD map for structures with scale sizes in the range 10-50 km for electron density profiles derived from COSMIC measurements for ionospherically active periods (December 4-7, time period 0100 to 0700 LT)

Larger values in Figure 7.13 demonstrate good correlation with the larger electron density enhancements at altitudes 100-120 km in Figure 7.7 (first plot). Prominent structures with scale size 10-50 km are observed within the auroral boundaries defined in Figure 7.7. This implies that the occurrence of medium-scale structures corresponds to the presence of nightside AEI. It is noted that there are also regions of high spectral density at latitudes below the auroral oval boundary. However the dominant distribution of medium-scale structures at auroral latitudes (and

corresponding to AEI) is evident. In addition to single PSD case studies in previous sections, Figures 7.7 and 7.13 also show the direct correlation between E-region density enhancements for disturbed auroral nighttime periods and PSD for structures

CHAPTER 8

CONCLUSIONS AND RECOMMENDATIONS

8.1 CONCLUSIONS

GPS radio occultation measurements onboard LEO satellites demonstrate potential as a powerful tool for studying three-dimensional electron density in the high latitude ionosphere. A drawback is that there are insufficient COSMIC RO events available per day to achieve continuous global coverage. However, improved coverage can be expected for COSMICII with an additional 12 satellites. Better spatial coverage can be maintained for ionospheric tomography.

In Chapter 5 the validation of COSMIC electron density profiles during disturbed periods is conducted and it is demonstrated that sufficient accuracy and resolution of COSMIC electron density measurements can be achieved to capture and identify small-scale ionospheric structures associated with scintillation. This work was summarized in a poster presented at the COSMIC workshop (student poster competition) in Boulder, USA, November 2009 [*Feng and Skone*, 2009].

Further analysis includes selection of a number of radio occultation events as representative of disturbed auroral ionospheric conditions. Fluctuations in electron density were observed near 110 km altitude during periods in which ground scintillation was detected by CANGIM GPS receivers. For SED events the ionospheric irregularities can extend into the F region over a wide range of altitudes.

Scale sizes of 10-20 km were observed for structures associated with AEI. For analyses of electron density profiles during auroral events two conference papers have been published [*Skone et al.*, 2008; *Skone et al.*, 2009].

Another important analysis conducted here is the derivation of electron density and TEC maps for E-region disturbances with high resolution. Such maps showed the spatial distribution of irregularities leading to scintillation effects; these products could be made available to the GPS user community in an ionosphere warning system. The auroral oval boundaries are readily apparent in these maps - essentially providing a near real-time capability to track the evolution of auroral substorms. This work was summarized in a presentation at the AMS conference held in Atlanta, USA, January 2010 [*Feng and Skone*, 2010]

A significant contribution of this work is identifying E-region electron density enhancement signatures during auroral scintillation periods. From COSMIC observations the presence of precipitating energetic electrons during auroral substorms is identified at E-region altitudes; scintillations develop in such regions of AEI processes. Results demonstrate that, for high latitude scintillation simulations (for GNSS applications), a simple phase screen model assuming concentration of electrons in a single thin layer is not realistic. A more complex multiple phase screen physics-based model is required for realistic studies and simulations of high latitude scintillation.

8.2 RECOMMENDATIONS

Radio occultation studies for the six-satellite COSMIC mission have provided new capabilities to observe ionospheric structures. In this thesis analyses were conducted for case studies of electron density profiles as well as ionosphere mapping on a global scale. There are several recommendations for future research.

1. Validations of radio occultation electron density profiles with more truth observations need to be conducted. Horizontal information about density distributions is required to make the Abel inversion more accurate. Verification of COSMIC electron density profiles especially for measurements of RO occurring at high latitudes during ionospherically disturbed periods (confirmed with magnetometer observations or ground scintillation measurements) should be conducted.

2. The RO electron density observations, or integrated TEC values, can also be used to study the middle and low latitude ionospheric irregularities (e.g. spread-F phenomenon, sporadic-E [*Wu*, 2006] and the effect of thermosphere wind shear). PSD analysis can be used to determine presence of irregularity structures with different scale sizes. Besides the raw observations from the LEO GPS receiver, L1 signal SNR can be used to detect the existence of ionosphere irregularities.

3. With datasets from different RO missions and the upcoming solar maximum period, long term observations can be used to study the annual and seasonal ionospheric behavior.

4. RO measurements are able to provide information for ionosphere modeling or scintillation modeling. The question of how to combine RO density profiles with

other observations (such as TEC measurements from ground-based GNSS receivers) for data assimilation purposes, and how to simulate the electron density above LEO altitudes, needs more consideration.

5. After COSMICII is deployed combinations of GPS, GLONASS, and other navigation systems will be available. A continuous global coverage is expected for better spatial resolution allowing ionospheric tomography. The detailed temporal characteristics of ionospheric irregularities during storm periods can be derived. GNSS RO are expected to provide capabilities for monitoring the ionosphere on a large scale continuously to obtain the temporal and spatial correlation characteristics of irregularities during disturbed conditions. Similar analyses of this study could be implemented again with better ionospheric high latitude observation availability from new RO missions.

REFERENCES

Aarons, J. (1993). The longitudinal morphology of equatorial F-layer irregularities relevant to their occurrence. *Space Science Reviews, vol. 63, issue 3-4,* pp. 209-243.

Aarons, J. (1982). Global morphology of ionospheric scintillation. *Proceedings of the IEEE, vol. 70,* pp. 360-378.

AMISR (2009). http://madrigal.haystack.mit.edu/, accessed on Aug 18, 2009

Anthes, R.A., P.A. Bernhardt, Y. Chen, L. Cucurull, K.F. Dymond, D. Ector, S.B. Healy, S.P. Ho, D.C. Hunt, Y.H. Kuo, H. Liu, K. Manning, C. McCormick, T.K. Meehan, W.J. Randel, C. Rocken, W.S. Schreiner, S.V. Sokolovskiy, S. Syndergaard, D.C. Thompson, K.E. Trenberth, T.K. Wee, N.L. Yen and Z. Zeng (2008). The COSMIC / FORMOSAT-3 mission: Early results. *Bulletin of the American Meteorological Society, vol. 89 (3),* pp. 313-333.

Baron, M.J. (1974). Electron density within aurora and other aurora E-region characteristics. *Radio Science, vol. 9, no. 2,* pg. 341.

Basu, S., K.M. Groves, S. Basu and P.J. Sultan (2002). Specification and forecasting of scintillations in communication/navigation links: Current status and future plans. *Journal of Atmospheric and Solar-Terrestrial Physics, vol. 64,* pg. 1745.

Bates, H.F., A.E. Belon and R.D. Hunsucker (1973). Aurora and poleward edge of the main trough. *Journal of Geophysical Research, vol. 78, no. 4684.*

Beyerle, G., T. Schmidt, G. Michalak, S. Heise, J. Wickert, C. Reigber (2005). GPS radio occultation with GRACE: Atmospheric profiling utilizing the zero difference. *Geophysical Research Letters, vol. 32, issue 13.*

Bhattacharyya, A., K.C. Yeh and S.J. Franke (1992). Deducing turbulence parameters from transionospheric scintillation measurements. *Space Science Reviews, vol. 61, no. 3-4,* pp. 335-386.

Born, M. and E. Wolf (1999). Principles of optics: Electromagnetic theory of propagation, interference and diffraction of light (7^{th} edition). Cambridge University Press, New York, USA.

Brunner, F.K. and M. Gu (1991). An improved model for the dual frequency ionospheric correction of GPS observations. *Manuscripta geodaetica, vol. 16,* pp. 205-214.

CASISMA (2009). http://bluebird.phys.ualberta.ca/carisma/, accessed on Aug 24, 2009.

Chen, W.S., C.C. Lee, J.Y. Liu, F.D. Chu and B.W. Reinisch (2006). Digisonde spread F and GPS phase fluctuations in the equatorial ionosphere during solar maximum. *Journal of Geophysical Research, vol. 111,* pg. A12305.

Coker, C., R. Hunsucker and G. Lott (1995). Detection of auroral activity using GPS satellites. *Geophysical Research Letters*, vol. 22, pp. 3259-3263.

Conker, R.S., M.B. El-Arini, C.J. Hegarty and T. Hsiao (2003). Modeling the effects

of ionospheric scintillation on GPS satellite-based augmentation system availability. *Radio Science, vol. 38, no. 1.*

COSMIC (2009). http://cosmic-io.cosmic.ucar.edu, accessed on Jun 30, 2009.

CSSDP (2009). http://portal.cssdp.ca, accessed on Sep 23, 2009.

Davies, K. (1990). Ionospheric Radio *(IEE Electromagnetic Waves).* Peter Peregrinus Ltd, London, United Kingdom.

de La Beaujardiere, O. and the C/NOFS Science Definition Team (2004). A mission to forecast scintillations. *Journal of Atmospheric, Solar-Terrestrial and Planetary Physics, vol. 66, issue 17,* pp. 1573-1591.

Dixon, J. (1997). An overview of global mobile robot navigation: Global positioning. *Surprise 97, Mobile Robot Navigation, vol. 1,* May 20, 1997. (http://www.doc.ic.ac.uk/~nd/surprise_97/journal/vol1/jmd)

Dubey, S., R. Wahi. and A.K. Gwal (2006). Ionospheric effects on GPS positioning. *Advances in Space Research, vol. 38,* pp. 2478-2484.

Eshleman, V.R. (1973). The radio occultation method for the study of planetary atmospheres. *Planetary Space Science, vol. 21,* pp. 1521-1531.

Feldstein. Y.I. (1967). Dynamics of auroral belt and polar geomagnetic disturbances. *Planetary Space Science, vol. 15,* pp. 209-229.

Feng, M. and S. Skone (2010). High latitude ionospheric irregularity detection using COCMIC radio occultation observations. The 90th American Meteorological society annual meeting: Proceedings of the Seventh Symposium on Space Weather (Atlanta, GA), January 2010, in press.

Feng, M. and S. Skone (2009). Validation of high latitude electron density measurements from COSMIC radio occultation under disturbed ionospheric conditions. COSMIC workshop: student poster competition (NCAR, Boulder, USA) November 2009.

Fjeldbo, G. and V.R. Eshleman (1965). The bistatic radar-occultation method for the study of planetary atmospheres. *Journal of Geophysical Research, vol. 70,* pp. 3217-3225.

Fong, C.J., C.Y. Huang, V. Chu, N. Yen, Y.H. Kuo, Y.A. Liou and S. Chi (2008). Mission results from FORMOSAT-3 / COSMIC constellation system. *Journal of Space and Rockets, vol. 45, no. 6,* pp. 1293-1302.

Fremouw, E.J., J.A. Secan and J.M. Lansinger (1985). Spectral behavior of phase scintillation in the night auroral region. *Radio Science, vol. 20, no. 4,* pp. 923-933.

Fritz, K. and M. Gu (1991). An improved model for the dual frequency ionospheric correction of GPS observations. *Manuscripta Geodaetica, vol. 16,* pp. 205-214.

Garcia-Fernandez, M. (2004). Contribution to the 3D ionospheric sounding with GPS data. Ph.D thesis, Research group of Astronomy and Geomatics, Department of applied mathematics IV and Applied Physics, University Politecnica de Catalunya,

Spain.

Garcia-Fernandez, M., M. Hernandez-Pajares, M. Juan and J. Sanz (2003). Improvement of ionospheric electron density estimation with GPSMET occultations using Abel inversion and VTEC information. *Journal of Geophysical Research, vol. 108, no. A9,* pg. 1338.

GIMA (2009). http://magnet.gi.alaska.edu/, accessed on Aug. 20, 2009.

Giraud, A. and M. Petit (1978). Ionospheric Techniques and Phenomena. D. Reidel publishing company, Dordrecht, Holland.

Gorbunov, M.E. (1996). Three-dimensional satellite refractive tomography of the atmosphere: A numerical simulation. *Radio Science, vol. 31,* pp. 95-104.

GPS Compendium (2009). GPS-Essentials of Satellite Navigation. GPS-X-02007-D.

GSC (2009). http://geomag.nrcan.gc.ca/, accessed on Aug, 18, 2009.

Hajj, G.A., C.O. Ao, B.A. Iijima, D. Kuang, E.R. Kursinski, A.J. Mannucci, T.K. Meehan, L.J. Romans, M. de la Torre Juarez and T.P. Yunk (2004). CHAMP and SAC-C atmospheric results and intercomparisons. *Journal of Geophysical Research., vol. 109, No. D6.*

Hajj, G.A., E.R. Kursinski, L.J. Romans, W.I. Bertiger and S.S. Leroy (2002). A technical description of atmospheric sounding by GPS occultation. *Journal of Atmospheric and Solar-Terrestrial Physics, vol. 64,* pp. 451- 469.

Hajj, G.A., L. Lee, X. Pi, L. Romans, W. Schreiner, P. Straus and C. Wang (2000). COSMIC GPS ionospheric sensing and space weather. *Terrestrial Atmospheric and Oceanic Sciences, vol. 11, no. 1*, pp. 235-272.

Hajj, G.A., L.J. Romans (1998). Ionospheric electron density profiles obtained with the Global Positioning System: Results from GPS/MET experiment. *Radio Science, vol. 33*, pp. 175-190.

Hannah, B.M. (2001). Modeling and simulation of GPS multipath propagation. Ph. D thesis, Queensland University of Technology, Australia.

Hargreaves, J.K. (1992). The solar-terrestrial environment: An introduction to Geospace-the Science of the Terrestrial upper atmosphere, ionosphere and magnetosphere. Cambridge University Press, New York, USA.

Haystack (2009). http://www.haystack.mit.edu/, accessed on Aug 20, 2009.

Hegarty, C., M.B. El-Arini, T. Kim and S. Ericson (2001). Scintillation modeling for GPS/Wide Area Augmentation System receivers. *Radio Science, vol. 36, no. 5,* pp. 1221-1231.

Hinson, D.P., Joseph D. Twicken, E. Tuna Karayel (1998). Jupiter's ionosphere: New results from voyager 2 radio occultation measurements. *Journal of Geophysical Research, vol.* 103, *no.* A5, pp. 9505-9520.

Hocke, K., K. Igarashia, M. Nakamuraa, P. Wilkinsonb, A. Pavelyevd and J. Wickert

(2001). Global sounding of sporadic E layers by the GPS/MET radio occultation experiment. *Journal of Atmospheric and Solar-Terrestrial Physics, vol. 63, no. 18,* pp. 1973-1980.

Hocke, K., A. Pavelyev, O. Yakovlev, L. Barthes and N. Jakowski (1999). Radio occultation data analysis by radio holographic method. *Journal of Atmospheric and Solar-Terrestrial Physics, vol. 61, no. 15,* pp. 1169-1177.

Hunsucker, R.D and J.K. Hargreaves (2003). The high-latitude ionosphere and its effects on radio propagation. Cambridge University Press, New York, USA

Hunsucker, R. D., C. Coker, J.A. Cook and G. Lott (1995). An Investigation of the feasibility of utilizing GPS/TEC signatures for near-real time forecasting of auroral-E propagation at high-HF and low-VHF frequencies. *IEEE Transactions on Antennas and Propagation, vol. 43,* pp. 1313-1318.

Hunsucker, R.D. (1992). Mini-review: Auroral and polar-cap ionospheric effects on radio propagation. *IEEE Transactions on Antennas and Propagation, vol. 40, no. 7,* pg. 818.

IGSCB (2009). http://igscb.jpl.nasa.gov/components/prods.html, accessed on June 20, 2009.

ISDC (2009). http://isdc.gfz-potsdam.de/modules.php?name=product_type_overview, accessed on June 29, 2009.

ISR (2009). http://isr.sri.com/iono/amisr/, accessed on Aug. 20, 2009.

Jakowski, N., A. Wehrenpfennig, S. Heise, C. Reigber, H. Luhr, L. Grunwaldt and T. K. Meehan (2002). GPS radio occultation measurements of the ionosphere from CHAMP: Early results. *Geophysical Research Letters, vol. 29, no. 10,* pp. 95-1 to 95-4.

Kaplan, E. and C. Hegarty (2005). Understanding GPS: Principles and applications, second edition. Artech House, Boston, USA.

Kelley, M.C. (1989). The Earth's Ionosphere: Plasma Physics and Electrodynamics. Academic Press Inc, California, USA.

Knight, M.F. (2000). Ionospheric scintillation effects on Global Positioning System receivers. Ph.D thesis, Department of Electrical and Electronic Engineering, The University of Adelaide.

Kunitsyn, V. and E. Tereshchenko (2003). Ionospheric tomography, Springer, New York, USA.

Kunitsyn V.E.and E.E. Tereshchenko (1992). Determination of the turbulent spectrum in the ionosphere by a tomographic method. *Journal of Atmospheres and Solar-Terrestrial Physics, vol. 54, no. 10,* pp. 1275-1282.

Kuo, Y.H., T.K. Wee, S. Sokolovskiy, C. Rocken, W. Schreiner, and D. Hunt (2004). Inversion and error estimation of GPS radio occultation data. *Journal of the Meteorological Society of Japan, vol. 82, no. 1B,* pp. 507-531.

Kursinski, E.R., G.A. Hajj, J.T. Schofield, R.P. Linfield and K.R. Hardy (1997).

Observing earth's atmosphere with radio occultation measurements using the global positioning system. *Journal of Geophysical Research, vol. 102 (D19),* pp. 23,429-23,465.

Ledvina, B.M., P.M. Kintner and J.J. Makela (2004). Temporal properties of intense GPS L1 amplitude scintillations at midlatitudes. *Radio Science, vol. 39, RS1S18, doi:10.1029/2002RS002832.*

Lee, L.C., C. Rocken and E.R. Kursinski (Eds.) (2001). *Applications of Constellation Observing System for Meteorology, Ionosphere and Climate.* Springer-Verlag, New York.

Lei, J.H., S. Syndergaard, A.G. Burns, S.C. Solomon, W.B. Wang, Z. Zeng, R.G. Roble, Q. Wu, Y.H. Kuo, J.M. Holt, S.R. Zhang, D.L. Hysell, F.S. Rodrigues and C.H. Lin (2007). Comparison of COSMIC ionospheric measurements with ground-based observations and model predictions: Preliminary results. *Journal of Geophysical Research, vol. 112, pg. A07308.*

Leick, A. (1995). GPS Satellite Surveying. second edition, John Wiley & Sons, U.S.A.

Levy, M. (2000). *Parabolic equation methods for electromagnetic wave propagation.* Institute of Electrical Engineering, London.

Liou, Y.A., A.G. Paveleyev, S.F. Liu, A.A. Pavelyev, N. Yen, C.Y. Huang and C.J. Fong (2007). FORMOSAT-3 / COSMIC GPS radio occultation mission: Preliminary results. *IEEE, Transactions on Geoscience and Remote Sensing, vol. 45, no. 11,* pp.

3813-3826.

Lomb, N.R. (1976). Least-squares frequency analysis of unequally spaced data. *Astrophysics and Space Science, vol. 39,* pp. 447-462.

Lyou, J.G. (2000). The Solar Wind-Magnetosphere-Ionosphere system. *Science, vol. 288, no. 5473,* pp. 1987-1991.

Martin, E. and J. Aarons (1977). F-layer scintillation and the aurora. *Journal of Geophysical Research, vol. 82,* pg. 2717.

McDonald, K.D. (2002). The modernization of GPS: Plans, new capabilities and the future relationship to Galileo. *Journal of Global Positioning Systems, vol. 1, no. 1-17.*

Melbourne, W.G., E.S. Davis, C.B. Duncan, G.A. Hajj, K.R. Hardy, E.R. Kursinski, T.K. Meehan, L.E. Young and T.P. Yunck (1994). The application of spaceborne GPS to atmospheric limb sounding and global change monitoring. *JPL Publications, vol. 94-18,* pg. 147.

Mendes, V.B. (1999). Modelling the neutral-atmosphere propagation delay in radiometric space techniques. Ph.D dissertation, Department of Geodesy and Geomatics Engineering, Technical Report, No. 199, University of New Brunswick, Fredricton, New Brunswick, Canada.

Mitchell, C.N., L. Alfonsi, G. De Franceschi, M. Lester, V. Romano and A.W. Wernik (2005). GPS TEC and scintillation measurements from polar ionosphere during the October 2003 storm. *Geophysical Research Letters, vol. 32, issue 12.*

Parkinson, B. W. and J.J. Spilker Jr. (1996). Global Positioning System: Theory and Applications, American Institute of Aeronautics, Washington, DC.

Pavelyev. A.G., Y.A. Liou, J. Wickert, T. Schmidt, A.A. Pavelyev and S.F. Liu (2007). Effects of the ionosphere and solar activity on radio occultation signals: Application to CHAllenging Minisatellite Payload satellite observations. *Journal of Geophysical Research, vol. 112.*

Pavelyev, A.K., Igarashi, C. Reigber, K. Hocke, J. Wickert, G. Beyerle, S. Matyugov, A. Kucherjavenkov, D. Pavelyev and O. Yakovlev (2002). First application of radioholographic method to wave observations in the upper atmosphere. *Radio Science, vol. 37, no. 3,* pp. 15-1 to 15-11.

Press, W.H., S.A. Teukolsky, W.T. Vetterling and B.P. Flannery (1997). Numerical Recipes in C. Cambridge University Press, New York, USA.

Ratcliffe, J.A. (1964). An introduction to ionosphere and magnetosphere. Cambridge University Press, Cambridge, Great Britain.

Rodger, A.S. and A.C. Graham (1996). Diurnal and seasonal occurrence of polar patches. *Annales Geophysicales, vol.*14, pp. 533-537.

Schaer, S. (1999). Mapping and predicting the earth's ionosphere using the global positioning system. Ph.D dissertation, Astronomical Institude, University of Berne, Switzerland.

Schreiner, S.W., C. Rocken, S. Sokolovskiy, S. Syndergaard and D. Hunt (2007). Estimates of the precision of GPS radio occultations from the COSMIC / FORMOSAT-3 mission. *Geophysical Research Letters, vol. 34, issue 4.*

Schreiner, S.W., S. Sokolovskiy and C. Rocken (1999). Analysis and validation of GPS/MET radio occultation data in the ionosphere. *Radio Science, vol. 34, no. 4,* pp. 946-966.

Schunk, R.W. and A.F. Nagy (2000). Ionospheres: Physics, Plasma and Chemistry. Cambridge University Press, New York, USA.

Skone, S. (2007). ENGO 633 Lecture Notes. Department of Geomatics Engineering, University of Calgary.

Skone, S. (2006). TECMODEL Operating Manual version 1.0. Department of Geomatics Engineering, University of Calgary.

Skone, S. (1998). Wide are ionospheric grid modeling in the auroal region. Ph.D thesis, UCGE Report Number 20123, University of Calgary, Calgary, Alberta, Canada.

Skone, S., M. Feng and R. Tiwari and A. Coster (2009). Characterizing ionospheric irregularities for auroral scintillations. ION GNSS: Proceedings of the 22nd International Technical Meeting of the Satellite Division of the Institute of Navigation (Savannah, GA), September 2009, pp. 2551-2558.

Skone, S., M. Feng, F. Ghafoori and R. Tiwari (2008). Investigation of scintillation

characteristics for high latitude phenomena. ION GNSS: Proceedings of the 21st International Technical Meeting of the Satellite Division of the Institute of Navigation (Savannah, GA), September 2008, pp. 2425-2433.

Skone, S., G. Lachapelle, D. Yao, W. Yu and R. Watson (2005). Investigating the impact of ionospheric scintillation using a software receiver. ION GNSS: Proceedings of the 18th International Technical Meeting of the Satellite Division of the Institute of Navigation (Long Beach, CA), September 2005, pp. 1126-1137.

Skone, S., R. Yousuf and A. Coster (2004) Performance evaluation of the Wide Area Augmentation System for ionospheric storm. *Journal of Global Positioning Systems, vol.3, no. 1-2,* pp. 251-258.

Skone. S and M. de. Jong (2000). The Impact of geomagnetic substorms on GPS receiver performance. *Earth Planets and Space, vol. 52,* pp. 1067-1071.

Skone, S. and M.E. Cannon (1999). Ionospheric effects on differential GPS applications during auroral substorm activity. *ISPRS Journal of Photogrammetry & Remote Sensing, vol. 54,* pp. 279-288.

Sokolovskiy, S.V. (2000). Inversions of radio occultation amplitude data. *Radio Science, vol. 35, no. 1,* pp. 97-105.

Spilker Jr., J.J. (1996). Tropospheric effects on GPS, in Global Positioning System: Theory and Applications, Vol. 1, American Institute of Aeronautics and Astronautics, Washington, DC.

Steiner, A.K, G. Kirchengast and H.P. Ladreiter (1999). Inversion, error analysis and validation of GPS/MET data. *Annales Geophysicae, vol. 17, no. 1*, pp. 122-138.

Straus, P.R. (1999a). Ionospheric remote sensing using GPS. *AIAA Conference Proc*., (AIAA-99-0628), Reno, NV.

Straus, P.R., (1999b). Correcting GPS occultation measurements for ionospheric horizontal gradients. *Proceedings of the Ionospheric Effects Symposium*, Alexandria, VA.

Straus, P.R., P.C. Anderson and J.E. Danaher (2003). GPS occultation sensor observations of ionospheric scintillation. *Geophysical Research Letters, vol. 30, no.8.*

Syndergaard, S. (2006). http://cosmic-io.cosmic.ucar.edu, COSMIC S4 data

Syndergaard, S. (2002). A new algorithm for retrieving GPS radio occultation total electron content. *Journal of Geophysical Research, vol. 29, no. 16,* pp. 55-1 to 55-4.

Syndergarrd, S., E.R, Kursinski, B.M. Herman, E.M. Lane and D. E. Flittner (2004). A refractive index mapping operator for variational assimilation of occultation data. *Monthly Weather Review, vol. 133, issue 9.*

Trauth, M. H. (2007). Matlab®Recipes for Earth Sciences, Second Edition, Springer, New York, USA.

Tsybulya, K. and N. Jakowski (2005). Medium- and small-scale ionospheric irregularities detected by GPS radio occultation method. *Geophysical Research Letters, vol. 32, issue 9.*

UCLA (2009). http://dawn.ucla.edu/personnel/russell/papers/magsphere/, accessed on August 1, 2006.

Wickert, J., G. Beyerle, R. Konig, S. Heise, L. Grunwaldt, G. Michalak, Ch. Reigber and T. Schmidt (2005). GPS radio occultation with CHAMP and GRACE: A first look at new and promising satellite configuration for global atmospheric sounding. *Annales Geophysicae, vol. 23*, pp. 653-658.

Wickert, J., Schmidt, T., Beyerle, G., Konig, R. Reigber, C. and N. Jakowski (2004). The radio occultation experiment aboard CHAMP: Operational data processing and validation of atmospheric parameters. *Journal of the Meteorological Society Of Japan, vol. 82*, pp. 381-395.

Wickert, J., R. Galas, T. Schmidt, G. Beyerle, C. Reigber, C. Forste and M. Ramastschi (2003). Atmospheric sounding with CHAMP: GPS ground station data for occultation processing. *Physics and Chemistry of the Earth, vol. 29, issue 2-3,* pp. 267-275.

Wickert, J., C. Reigber, G. Beyerle, R. Konig, C. Marquardt, T. Schmidt, L. Grunwaldt, R. Galas, T.K. Meehan, W.G. Melbourne and K. Hocke (2001). Atmosphere sounding by GPS radio occultation: First results from CHAMP. *Geophysical Research Letters, vol. 28, no. 17,* pp.3263-3266.

William, S.S., S.V. Sokolovskiy, C. Rocken and D.C. Hunt (1999). Analysis and validation of GPS/MET radio occultation data in the ionosphere. *Radio Science, vol. 34*, pp. 946-966.

Wu, D.L. (2006). Small-scale fluctuations and scintillations in high-resolution GPS/CHAMP SNR and phase data. *Journal of Atmospheric and Solar-Terrestrial Physics, vol. 68*, pp. 999-1017.

Wu, D.L., C.O. Ao, G.A. Hajj, M.de. La Torre Juarez and A.J. Mannucci (2005). Sporadic E morphology from GPS-CHAMP radio occultation. *Journal of Geophysical Research, vol. 110, no. D2.*

Wu, D.L., C.O. Ao, G.A. Hajj, M.de. La Torre Juarez and A.J. Mannucci (2002). A study of sporadic E irregularities with SNR and phase measurements from GPS-LEO occultations. CEDAR Meeting, Longmont, USA.

Yakovlev, O.I (2002). Space Radio Science. London, U.K.: Taylor & Francis., New York, USA.

Yakovlev. O.I., S.S. Matyugov and I.A. Vikov (1995). Attenuation and scintillation of radio waves in the earth's atmosphere from radio occultation experiments on satellite-to-satellite links. *Radio Science, vol*. 30, pp. 591-602.

Yu, W. (2007). Selected GPS receiver enhancements for weak signal acquisition on tracking. Ms.c Thesis, Report No. 20249, Department of Geomatics Engineering, The University of Calgary.

Yu, W., G. Lachapelle and S. Skone (2006). PLL performance for signals in the presence of thermal noise, phase noise and ionospheric scintillation. ION GNSS: Proceedings of the 19 International Technical Meeting of the Satellite Division of the Institute of Navigation (Fort Worth, TX), September 2006, pp. 26-29.